The Dissertation Committee for Georgios Stratis
certifies that this is the approved version of the following dissertation:

Monitoring damage of self-assembled monolayers using metastable excited helium atoms

Committee:

Mark G. Raizen, Supervisor

Lauren Webb

Alex de Lozanne

Alex Demkov

Monitoring damage of self-assembled monolayers using metastable excited helium atoms

by

Georgios Stratis

DISSERTATION

Presented to the Faculty of the Graduate School of

The University of Texas at Austin

in Partial Fulfillment

of the Requirements

for the Degree of

DOCTOR OF PHILOSOPHY

THE UNIVERSITY OF TEXAS AT AUSTIN

May 2020

To my family.

Acknowledgments

In my journey to pursue a doctorate degree in physics there were many people who stood by me and helped me in one way or another to succeed in my endeavor. I will list as many people as I can and any omission should not be thought of as a slight, but rather as a sign of a tired mind who has been struggling for seven years. First and foremost I would like to thank my family and my friends I met here in Austin. For starters, I would like to wholeheartedly thank my family here in Austin: Sarah Serwe and Lola Strati-Serwe. They have both been critical for my success. Sarah your tireless and tenacious character act as inspiration for me. More often than not, you have taught me the value of good work. Lola you are an amazing hound dog that I love walking around the block. You have been my constant companion through all these years. Equally important are my family back in Cyprus: Kostas (father), Kalliopi (mother), Maria (sister), Dimos (brother, currently in the U.K.), Trifonas (bother), Afroditi (sister-in-law currently in the U.K.), Nikos (brother-in-law), and Alexandra (niece). My dad has been a huge inspiration for me since I was a kid. I would not have come to the US had it not been for my dad. My mum has been the voice of kindness in my life and taught me the value of selflessness. My siblings, sister-in-law, brother-in-law, and niece have all been by me from day one and I will never forget it. You have all stood by me when everything was collapsing and I am thankful! Besides my

family, my friends have played a crucial role. Abhranil (Neel) Das you have been an extraordinary individual to hang around with. You have inspired me to pursue my dreams and amazed me with all the crazy stuff you were doing. Stefan Eccles your calm voice stands for the voice of reason and compassion. No matter what happened in your life, I have never seen you upset or yelling and as an aside you are an excellent outdoorsman. Ben, Sarah, and Seth Stephens have always been there for us. Through playing board games or having a dinner, you were all pleasant to be around. I would like to thank Josiah Couch and Kim Carmona for their friendship. Josiah you are a great person to be around and full of honesty. Your enormous interest for languages is contagious. I would like to thank Dr. Gaurav Chaudhary for all the fruitful discussions we have had. Gaurav you have enlarged my understanding of physics and beyond. Special thanks go to Dr. Rustam Antia who even though he is not a physicist he occupies a special place in my heart. Rustam you have made me think a lot and have helped me learn many valuable lessons. The last friend I would like to thank is Dr. George Miloshevich the salsa dancer who has always provided me with all the necessary facts. George you are one in a million and you bring joy to my life.

Having thanked my family and friends I turn my attention to my academic family. First and foremost I would like to thank my advisor, professor Mark Raizen, who was gracious enough to accept me in his lab and mentored me for all these years. Mark is a constant source of ideas and I really envy his ability to come up with something new every month. I am also inspired by his

enthusiasm for delving into uncharted territories and trying to solve problems that are nominally outside his field. Of course nothing could have happened without the immense help we received from professor Lauren Webb from the chemistry department. Her welcoming attitude and willingness to collaborate with us was the catalyst needed for my experiment to succeed. For this I will be eternally grateful and nothing I can say or write can express my deep gratitude. Thank you Dr. Webb! Having spoken about professor Webb, I would like to thank Henry Pan who is a graduate student at the Webb lab. You have been extremely patient with me when you showed us how to grow self-assembled monolayers and use the FTIR machine. You definitely scared me a lot about the hydrogen cylinder exploding while annealing gold-coated silicon. I am also happy that I have worked with you Henry for you have always been a solid person for every experiment I suggested. Besides my collaborators, I could have never graduated had it not been for the other two committee members professor Alex Demkov and Alex de Lozanne who always smile each time they see me.

Having thanked my committee I would like to turn my attention to my colleagues and I will thank them in a chronological order. First, I would like to thank Dr. Rodrigo Castillo who instilled in me enthusiasm and excitement for experimental physics. You have given me a lot of tools and you showed me how to teach. I want to thank Dr. Jamie Gardner for the endless discussions regarding physics and not only. Jamie you have been and still are a bright spot in my life and I hope one day we end up writing that paper about wealth.

Furthermore, I would like to thank Dr. Erik Anciaux for his support and companionship. Erik you have been a huge influence on how I see things and the reason why I will go back to Cabo Bob's. Not enough can be said or written or thought about Dr. Igal Bucay. Igal you have been with me since day one (almost) and graduated a year before me. Igal you have been an amazing friend and thank you for that. Jordan Zesch has been the longest member on my team and has contributed the most. Jordan you have been a constant source of articles and heated discussions. Additionally, I would like to thank Dr. Kevin Melin for his constant support. There was never a day gone by that I would not ask Kevin for help and he was always glad to help me. Yi Xu has been incredible over the last few years. She has always welcomed me with a big smile to the lab and I am grateful for the discussions we had. I would like to thank Dr. Yu Lu for his amazing work ethic and smile. Anytime I will talk with Yu he would always made me laugh. Special thanks to Logan Hillberry who constantly heard my hypotheses. Logan you have always been the most interested person in physics I have ever met. It is important to thank the postdoctoral scientists in our lab. First of all, I would like to wholeheartedly thank Dr. Diney Ether. Diney you have been an amazing resource of physics knowledge as well as life advice. You have hugely influenced me and hopefully I will make a trip to Brazil to visit you. I would also like to thank our other postdoc Dr. Ahmed Helal. Good luck with all of your endeavors Ahmed. Among the Raizen lab people, Lukas Gradl had an impact on me. Lukas you were the first person to talk to me about free and

open source software. Since that day I have been trying to learn more about it. I would like to thank Dr. Scott Bustabad who has been a great addition to our lab. Scott you are a really thoughtful and caring person. You came the last year of my Ph.D., but you have made a huge impact.

Although I might have never explicitly showed it, I had always enjoyed the company of our fellow undergraduate lab colleagues. David Dunsky you are a good and intelligent person. I am confident in your ability to thrive. Will Yager was the first undergraduate student who explicitly worked under my project. You are the reason why I was inspired to learn more about electronics and attempted to learn functional programming. Zoe de Beurs was the last undergraduate who worked with me on my project. I would like to thank you Zoe for always trying your hardest to complete all the tasks I gave you, even those tasks that I had not thought through. Zoe you are an inspiring person with a lot of passion in you for change. Julia Orenstein and Gabriel Alvarez were both really enthused and had been hearing me complaining a lot. I am really happy to see you both doing well and pursuing your dreams. The undergraduates that have been with me this last year were Sebastian Miki-Silva and Nicholas Mendez. These two have been huge assets for the Raizen lab. Your patience and work ethic are both amazing. Besides that, you are both really genuine characters. Seba I hope you find the job or graduate school you are hoping for. Nico keep fighting and you will be rewarded.

I would like to thank from the depths of my heart our unbelievably skilled machine shop staff. These people are the unsung heroes of every ex-

perimental group at the UT physics department. They can turn almost every crazy design you might think of into reality. Most of the custom hardware I used in my experiment was built by them and they have been always pleasant to work with. More specifically, I would like to thank Allan Schroeder who was the machine shop supervisor up until last year and had always helped me re-design and adjust my drawings. Moreover, I would like to thank Jack Clifford for his kindness and willingness to teach me how to use the mill and the lathe in the student machine shop. Of course I would like to thank all of the machinists who have been part of this amazing journey. All of them are the heroes we all need! The workhorse of our experimental apparatus is a hemispherical electron analyzer that professor James Erksine had lent us for the entire duration of my Ph.D. and I am thankful for that.

On a different note, I would like to thank Texas State Employees Union (TSEU) for introducing me to the labor struggle. I joined the union at a time when I was lost and the union provided me a community of people that had the spark of justice in them. TSEU reminded me and taught me that a good scientist is one that is also a good, conscious, and active member of society. Keep the fight going on y'all!

Monitoring damage of self-assembled monolayers using metastable excited helium atoms

Georgios Stratis, Ph.D.
The University of Texas at Austin, 2020

Supervisor: Mark G. Raizen

Understanding the mechanisms behind material damage can enable us to prevent damage from happening in the first place, repair materials, and utilize damage for applications such as lithography. Atoms have been used in a multitude of experiments to probe and understand the fundamental laws of nature. In this dissertation we are presenting our results of using metastable excited helium atoms to characterize the damage caused by an electron beam on an organic self-assembled monolayer. We have also investigated the role the substrate plays in damage through X-ray photoelectron spectroscopy and metastable induced electron emission spectroscopy.

Table of Contents

List of Tables

List of Figures

Chapter 1

Introduction

1.1 Motivation

Damage is a ubiquitous phenomenon in every day life with examples ranging from sunburns due to ultraviolet radiation to breaking a wall with a sledge hammer. Despite the fact that these two examples seem far removed from each other, once we zoom in to the nanoscale we can see that in both cases damage is ultimately due to the breaking of molecular bonds. Even though this explanation seems enough to describe damage it does leave a series of questions unanswered such as the following: What are the dynamics of damage? What are the various mechanisms leading to a molecular bond breaking? Once a bond breaks, what happens to the newly freed molecules? Do they recombine? Do they combine with other molecules in the ambient environment? Ultimately, understanding how a material is damaged allows us to prevent damage in the first place, devise repairing mechanisms, and utilize damage for applications such as lithography.

1.2 Studying damage in organic materials

Understanding how organic materials get damaged has important ramifications in technology (e-beam lithography), medicine (cancer therapy and prevention), and beyond. Self-assembled monolayers of alkanethiolate molecules, discussed in chapter 4, provide a good platform to understand damage in organic materials. In previous studies, researchers used different techniques such as x-ray photoelectron spectroscopy (XPS) [1]–[4], Auger electron spectroscopy (AES) [5], secondary ion mass spectrometry (SIMS) [6] to study damage induced on self-assembled monolayers. Results from reference [1] are shown in fig. 1.1 where they used XPS to monitor electron-induced damage on a self-assembled monolayer. The main issue with the techniques used in previous studies, is the fact that the beams used to probe a material induce damage during the data acquisition. The goal of our project is to overcome this issue by probing materials with metastable excited helium atoms which induce significantly less damage.

1.3 Metastable Atom Electron Spectroscopy (MAES)

Metastable atom electron spectroscopy is a promising platform with the following advantages over techniques which use x-rays or electrons. First, metastable atoms induce very little damage due to their kinetic energy. They can cause damage due to their de-excitation process, but that amount of energy is relatively small ($<$20 eV). In comparison, most electron microscopes use beams with energies $\sim$5 keV, damaging the sample through electron cas-

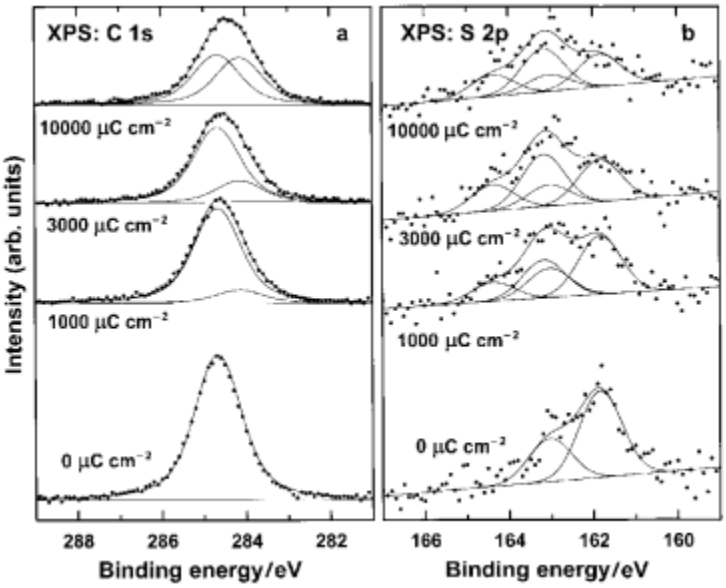

Figure 1.1: XPS spectra of C 1s (left) and S 2p (right) of a hexadecanethiolate monolayer on gold after different exposures to 50 eV electrons. As the electron dose increases the peaks get broader and shorter indicating that the monolayer has undergone a structural change. The figure was taken from reference [1].

cade events as well as heating. Second, metastable atoms are surface-sensitive probes. Metastable atoms interact with a surface through an electron exchange via tunneling. This tunneling event is followed by an electron emission. Collecting these emitted electrons allows us to extract information about the material. For this reason, metastable atoms are probing only the surface similar to scanning tunneling microscopes and can give us information only about the topmost layer of the material. Lastly, metastable atoms can probe any kind of material regardless of its conductivity as long as the internal energy of the metastable atom is high enough to overcome certain constraints such as the material's work function. This technique has been developed over

many decades and is referred to by various names such as metastable atom electron spectroscopy (MAES), metastable induced electron spectroscopy (MIES), metastable de-excitation spectroscopy (MDS), and various other acronyms [7]. For the purpose of this dissertation, we are using the term metastable atom electron spectroscopy (MAES) in an effort to indicate that this is a spectroscopy technique where the detected particles are electrons which are emitted due to metastable atom interaction with our sample. The technique as well as its main underlying mechanisms are described in chapter 3. The main challenge behind using MAES is the inability to obtain local information from a certain region of a material due to the inability to create a focused atomic beam with high brightness. Nevertheless, metastable atoms' ability to probe the surface of a sample without inducing significant damage proves extremely valuable.

1.4 Repairing and preventing damage

Modern microscopy techniques face the extreme difficulty of studying organic materials, such as DNA, without damaging them or significantly modifying them. In reference [8], it was proposed that an organic molecule would be placed on top of graphene in order to prevent the molecule from getting damage from a probing beam of electrons. The idea is that damage happens as a result of charge accumulation on the sample due to electron emission and exposure to the incoming electron beam. The charge accumulation causes Coulomb explosion; thus breaking the material's molecular bonds. If

one could stop charge accumulating by providing a reservoir of electrons, we should be able to prolong the life of our material or even prevent damage entirely. The substrate on which the sample is adsorbed can provide this reservoir of electrons. We not only need many free electrons available but also need those electrons to move as fast as possible in order to prevent a charge from building up. To that end conductors seem to be the natural candidates since high conductivity indicates high charge carrier density and high charge mobility. Another candidate is graphene, which outperforms conductors due to its much higher electron mobility. Having said that, conductors have a significantly higher charge carrier density than graphene and that could play a crucial role. In our experiments we studied how x-rays and electrons damage self-assembled monolayers on gold and graphene substrates to investigate how important the substrate was in preventing damage. In fig. 1.2 we show how the MAES spectrum of a 11-bromo-1-undecanethiol monolayer changes after a series of exposures to a 65 eV electron beam. The preliminary results of our experiments with an analysis contrasting the two substrates are presented in chapter 7. Further experiments are needed to refine our understanding of how the graphene substrate interacts with the adsorbed alkanethiolate molecules.

1.5 Overview of this dissertation

This dissertation presents most of the information necessary to understand the main ideas behind our project along with our experimental results and analysis. In chapter 2, we present some basic ideas and terminology from

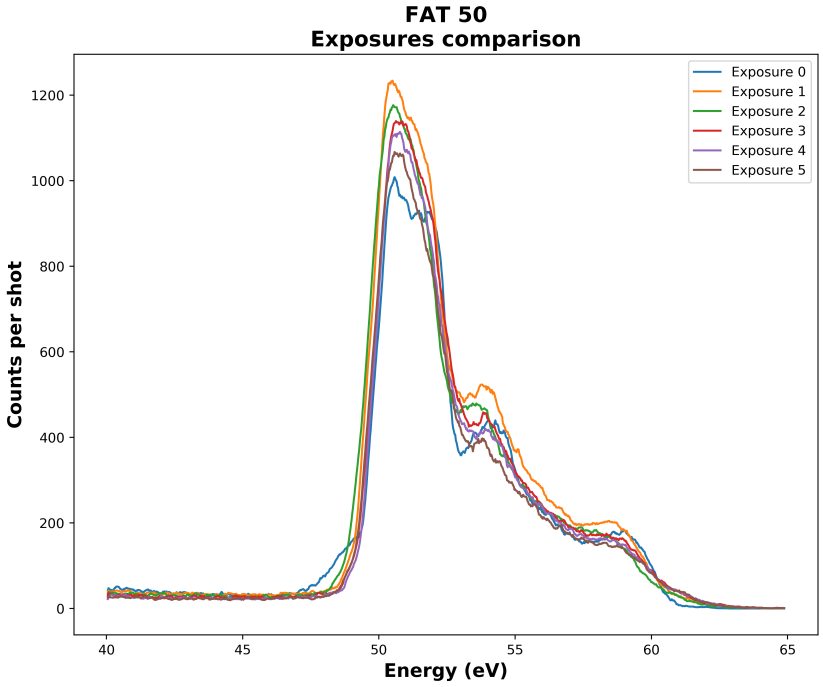

Figure 1.2: MAES spectrum of a 11-bromo-1-undecanethiol self-assembled monolayer on a graphene substrate after a series of exposures to an electron beam with energy 65 eV. In this experiment we used MAES to determine if the graphene substrate prevented the electron induced damage on the self-assembled monolayer and is discussed in more detail in section 7.4.

quantum mechanics that are deemed necessary to understand the theory and results of our experiment. The presentation does not constitute a complete description of the fundamental concepts of quantum mechanics since doing so will require an entire book. In chapter 3, we present the theory behind metastable atom electron spectroscopy as well as x-ray photoelectron spectroscopy, which were both used in our experiments. Our goal was to introduce

the reader to the main equations and mechanisms governing the two techniques in order to have a rudimentary understanding of how to interpret the results presented. In chapter 4, we briefly discuss the theoretical framework behind molecular bonds and provide an overview of self-assembled monolayers. The discussion provides an insight of what a molecular bond is in an attempt to understand the mechanisms behind bond-breaking. In chapter 5, we present concepts from electron and atom optics which were necessary for the development of our apparatus. In chapter 6, we present all the information behind our experimental apparatus and its operation, allowing future generations to replicate our experiments and results. In chapter 7, we present the results of our project, namely how MAES can be used to monitor damage on organic materials. We also present preliminary results from experiments where we monitored the damage induced on self-assembled monolayers adsorbed on graphene. Lastly, chapter 8 concludes this dissertation with suggestions for further improvements and indicate future directions for the entire project.

Chapter 2

Quantum mechanics fundamentals

The birth of quantum mechanics can be traced back in the early 1900's in the effort of Max Planck to explain the blackbody radiation [9]. That discovery allowed scientists to answer a lot of open questions and enabled technological advancements. In this chapter, certain concepts from quantum mechanics will be presented in order to provide the basic theoretical framework behind the project. First, we are going to present Schrödinger's equation and apply it on the case of the hydrogen atom. The main goal behind this exposure is to familiarize ourselves with one of the few exactly solvable problems in quantum mechanics and identify some of the consequences of quantum mechanics. Understanding the hydrogen atom might seem pedantic; however, the hydrogen wavefunctions constitute the starting point for many calculations whether that is calculating the energy levels of helium or understanding chemical bonds. Following the hydrogen atom discussion, we are going to explore the helium atom and its energy levels. Even though we can write down the exact equation describing the helium atom, we are unable to have an exact mathematical solution for its energy levels and its wavefunctions. Our next endeavor is to present the concepts of allowed and forbidden transitions, which are closely related to the lifetime of an energy level. Lastly, we are going to

briefly discuss how to apply quantum mechanics in real materials and present some important concepts that are fundamental to the field.

2.1 Schrödinger's equation

Schrödinger's equation has been the main tool used to formulate most of the quantum mechanics framework and has provided solutions to many phenomena that classical mechanics could not properly explain. Schrödinger's equation is a first order differential equation that resembles the heat equation; although, unlike the heat equation, it explicitly incorporates imaginary numbers in its formulation. Schrödinger's equation is most frequently expressed in an operator form, as can be seen in eq. (2.1). The *Hamiltonian* operator $\hat{H}$ encapsulates all the interactions and effects of the system of interest and $\Psi(\boldsymbol{r}, t)$ is the notorious wavefunction describing the state of the system. Giving an intuitive interpretation to the wavefunction is not a trivial manner and despite quantum mechanics being at least 120 years old there is still a vibrant discussion about the nature of the wavefunction. For more details about the interpretation of the wavefunction the reader is encouraged to visit references [9], [10].

$$i\hbar\frac{\partial\Psi(\boldsymbol{r}, t)}{\partial t} = \hat{H}\Psi(\boldsymbol{r}, t) \tag{2.1}$$

Operators are extremely useful mathematical constructs allowing us to modify the problem from a differential equation into a linear algebra problem making certain calculations easier. An operator is usually signified by an uppercase letter with a hat. For example, the x, y, and z coordinates translate to the $\hat{X}$,

$\hat{Y}$, and $\hat{Z}$ operators respectively. Depending on the mathematical space used to setup the problem, an operator takes different forms. The most common spaces used are the position (x, y, z) and momentum (p_x, p_y, p_z) spaces. In most cases, we choose to work in position space and the operators obey the relations presented in eq. (2.2) where the momentum operator turns into the gradient operator and the coordinate operators $(\hat{X}, \hat{Y}, \hat{Z})$ turn into a multiplication with the respective coordinate.

$$\begin{aligned} \hat{P} &\to -i\hbar\boldsymbol{\nabla} \\ \hat{X} &\to x \\ \hat{Y} &\to y \\ \hat{Z} &\to z \end{aligned} \tag{2.2}$$

One can immediately notice the partial time derivative explicitly present in eq. (2.1). Seeing this time derivative one might ponder the following: for a given Hamiltonian $\hat{H}$ could we find a wavefunction Ψ that retains some of its fundamental characteristics over time? Our first instinct might be to choose a wavefunction that is constant over time. Delving a little deeper into this question we realize that a time independent wavefunction will only work if its equal with zero which means nothing is happening and that is boring. However this is not the end of the thought experiment. Instead of a constant wavefunction, we could have a wavefunction such that its time derivative gives us the wavefunction back times a constant as demonstrated in eq. (2.3).

$$\begin{aligned} i\hbar\frac{\partial\Psi_n(\boldsymbol{r},t)}{\partial t} &= \hat{H}\Psi_n(\boldsymbol{r},t) \\ E_n\Psi_n(\boldsymbol{r},t) &= \hat{H}\Psi_n(\boldsymbol{r},t) \end{aligned} \tag{2.3}$$

Such a wavefunction Ψ_n, is called a *stationary state* of the specific Hamiltonian characterizing our system and is associated with a constant E_n, which we will later identify as the state's energy, that is part of the Hamiltonian's *spectrum* [11]. Stationary states are an extremely important concept in quantum mechanics that often goes overlooked and not given much attention. They are the backbone of the entire framework since in most cases our entire effort goes into calculating and measuring the energies associated with these states. Until this point the discussion was kept at a relatively abstract level. We are going to demonstrate the utility of eqs. (2.1) and (2.3) in a real scenario: the hydrogen atom.

2.2 The hydrogen atom

Quantum mechanics gained immense popularity once it was able to provide a robust prediction of the hydrogen spectrum. The key element behind this success was the ability to transform familiar concepts from classical mechanics, i.e kinetic energy and central potential, into an operator form in Schrödinger's differential equation. The hydrogen atom is a simple system that involves two moving parts, a proton and an electron, that attract each other due to the Coulomb electrostatic interaction. The system can is described in the quantum mechanics formalism using eq. (2.4):

$$E_n\Psi_n(\boldsymbol{r_p},\boldsymbol{r_e}) = \frac{\hat{P_p}^2}{2m_p}\Psi_n(\boldsymbol{r_p},\boldsymbol{r_e}) + \frac{\hat{P_e}^2}{2m_e}\Psi_n(\boldsymbol{r_p},\boldsymbol{r_e}) - \frac{e^2}{4\pi\epsilon_0|\boldsymbol{r_p}-\boldsymbol{r_e}|}\Psi_n(\boldsymbol{r_p},\boldsymbol{r_e}) \tag{2.4}$$

where E_n is the energy level corresponding to the stationary state $\Psi_n(\boldsymbol{r_p}, \boldsymbol{r_e})$ $\frac{\hat{P_p}^2}{2m_p}$ is the proton's kinetic energy, $\frac{\hat{P_e}^2}{2m_e}$ is the electron's kinetic energy, m_p is the mass of the proton, m_e is the mass of the electron, and $-\frac{e^2}{4\pi\epsilon_0|\boldsymbol{r_p}-\boldsymbol{r_e}|}$ represents the electrostatic attraction between the electron and the proton. It is important to note that the wavefunction encapsulates information for both the electron and the proton. For the sake of simplicity we are going to assume that only the electron is moving and the proton is frozen in place. Thus the equation describing the hydrogen atom becomes eq. (2.5) where we used eq. (2.2) to substitute for the operator forms in position space.

$$E_n\psi(\boldsymbol{r}) = -\frac{\hbar^2}{2m_e}\nabla^2\psi_n(\boldsymbol{r}) - \frac{e^2}{4\pi\epsilon_0 r}\psi_n(\boldsymbol{r}) \tag{2.5}$$

One can drop the assumption we have just made and solve the problem including the motion of the proton which is presented in references [9], [11]. Back to our task, in order to solve eq. (2.5) it is best to use spherical coordinates due to the spherical symmetry of our problem. Using the tools developed by valiant mathematicians, the functions that satisfy eq. (2.5) are presented in eq. (2.6) and the convention followed is the one presented in reference [12]. The details of how to solve the hydrogen atom's differential equation are outlined in references [9], [11].

$$\begin{aligned}
\psi_{nlm}(r,\theta,\phi) &= \sqrt{\left(\frac{2}{na_0}\right)^3 \frac{(n-l-1)!}{2n(n+l)!}} e^{-\frac{\rho}{2}} \rho^l L_{n-l-1}^{2l+1}(\rho) Y_l^m(\theta,\phi), \\
\rho &= \frac{2r}{a_0}, \\
a_0 &= \frac{4\pi\epsilon_0\hbar^2}{m_e e^2},
\end{aligned} \tag{2.6}$$

where $L_{n-l-1}^{2l+1}(\rho)$ is the generalized Laguerre polynomial of degree $n-l-1$ and $Y_l^m(\theta,\phi)$ is a spherical harmonic of degree l and order m. The norm of the hydrogen wavefunctions squared for the cases of $n = 1,2,3$ and $l = 0,1,2$ is shown in fig. 2.1. The indices n, l, m are not mere mathematical structures, but

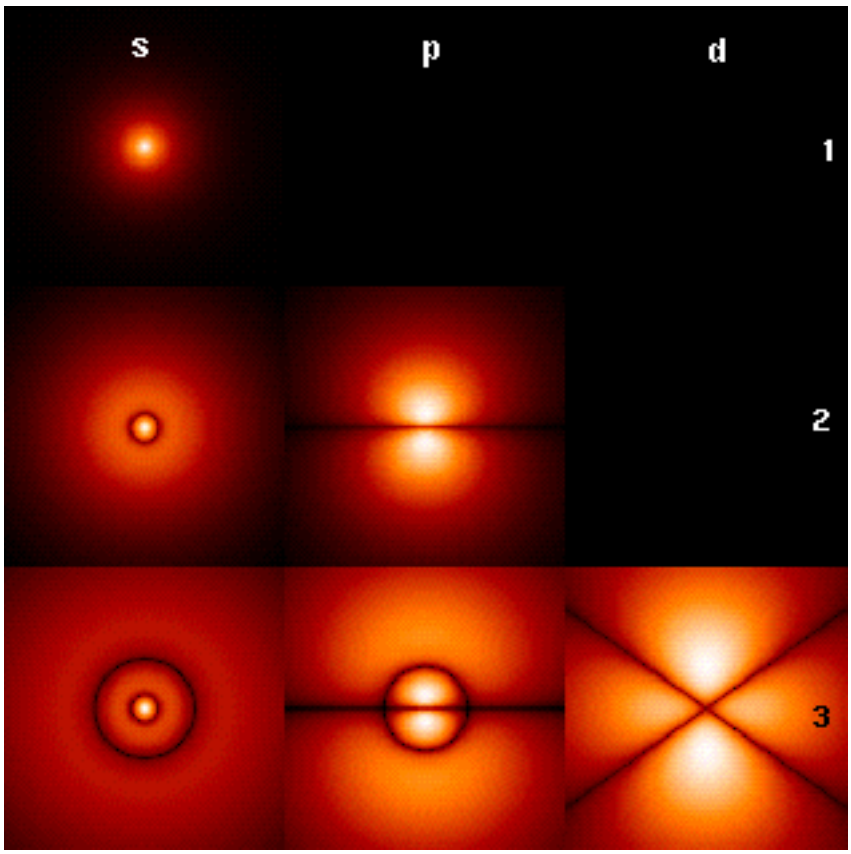

Figure 2.1: The norm of the hydrogen wavefunctions squared for $n = 1,2,3$ and $l = 0,1,2$ projected on the xz-plane. The image was borrowed from reference [12].

have certain physical features attributed to them based on the role they play in the solution of the problem. The index n is called the *principal quantum*

number and gives us a notion of how big an atom is since it only appears in the radial part of the solution. The index l is associated with the *orbital angular momentum* of the electron and m is the *magnetic* quantum number. Both l and m are present in the spherical harmonic part of the solution that deals with the azimuthal and longitudinal angles ϕ and θ respectively. Since these two indices partake in the angular portion of the solution it is natural to associate them with the angular momentum. Having said that, we should bear in mind that l participates in the radial part of the wavefunction as well. The indices n, l, m are referred to as *quantum numbers*. The quantum numbers we have just presented are restricted to take integer values and obey the rules outlined in eqs. (2.7) to (2.9). Lastly, the orbital quantum number l, due to historical reasons predating quantum mechanics, takes letter values instead of numbers. The nomenclature is presented in table 2.1.

$$n \in \mathbb{N} \tag{2.7}$$

$$l = 0, 1, 2, \ldots, n-1 \tag{2.8}$$

$$m = -l, -(l-1), -(l-2), \ldots, l-2, l-1, l \tag{2.9}$$

For a given hydrogen wavefunction ψ_{nlm} the corresponding energy is given by eq. (2.10) and the numerical values for a subset of the energy levels are presented in table 2.2.

$$\begin{aligned} E_n &= -\frac{e^4 m_e}{32\pi^2 \epsilon_0^2 \hbar^2 n^2} \\ E_n &\approx -\frac{13.6}{n^2}\ eV \end{aligned} \tag{2.10}$$

As we can see, the energy levels can be indexed by the principal quantum

Numerical value	**Letter value**
0	s
1	p
2	d
3	f
4...	g and then follows alphabetical order except the letter j and those already used

Table 2.1: Orbital angular momentum nomenclature providing a correspondence between numerical and letter values.

n	**Energy (eV)**
1	00.0000
2	10.1988
3	12.0875
4	12.7485
Ionization	13.5984

Table 2.2: Hydrogen energy levels retrieved from the NIST Atomic Spectra Database [13]. The energy levels are referenced with respect to the ground state in contrast with eq. (2.10) in which the energy levels are referenced with respect to the ionization energy that lies at the start of the energy continuum.

number n which is always an integer, meaning that the energy levels are discrete and infinitely many. In eq. (2.10) the energy levels are referenced from the continuum which is the point at which the electron is liberated from the hydrogen atom and can travel freely on its own. Surprisingly, or not, the energy levels do not depend on l and m, but depend solely on n. That means we can have wavefunctions with different quantum numbers l or m but the same n corresponding to the same energy level. This situation where we have more

than one wavefunction with the same energy level is called *degeneracy* and the energy level is referred to as being *degenerate*.

2.2.1 Lessons from the hydrogen atom

For starters, we actually used Schrödinger's equation and found exact solution to a real problem, namely the hydrogen problem. The solution allows us to determine the energy values associated with the hydrogen atom, which can be verified experimentally, and its wavefunctions. We also learned that the energy levels are discrete and only depend on the principal quantum number n. That also has the consequence that wavefunctions with different l or m that share the same n, correspond to the same energy level, leading to degenerate energy levels. More importantly, the hydrogen atom laid the groundwork for concepts coming up later in the chapter where the hydrogen wavefunctions are going to re-appear as the starting point for understanding the structure of other atoms and energy bands in solids. Lastly, using Schrödinger's equation to understand the hydrogen atom did leave behind some unanswered questions. The equation neither addresses relativity nor spin angular momentum which is our next topic.

2.3 Spin angular momentum and Pauli's exclusion principle

Having seen that a hydrogen wavefunction ψ_{nlm} is uniquely determined by its quantum numbers n, l, m, one might wonder if there are more quantum

numbers that for some reason did not make an appearance but nonetheless are essential for uniquely determining the wavefunction. Such quantum numbers are the spin angular momentum s and the spin projection m_s. In most textbooks and in our every day parlance, we physicists often referred to both quantum numbers s and m_s as the *spin*. These quantum numbers do not appear in the non-relativistic Schödinger equation. Any operators L and L_z, where L_z is the projection of L along the z-axis, that obey eqs. (2.11) and (2.12) allow for l and m to take integer and half-integer values [9], [11].

$$\hat{L}^2 \left|\psi_{nlm}\right\rangle = \hbar^2 l(l+1) \left|\psi_{nlm}\right\rangle , \tag{2.11}$$

$$\hat{L}_z \left|\psi_{nlm}\right\rangle = \hbar m \left|\psi_{nlm}\right\rangle , \tag{2.12}$$

$$m = -l, -(l-1), \ldots, (l-1), l \tag{2.13}$$

The spin is precisely an operator that obeys eqs. (2.11) and (2.12) and can take half integer values as in the case of an electron which has $s = \frac{1}{2}$. Having an angular momentum that takes half-integer values startles people, but even worse there is no familiar concept from our day to day life that behaves the same way as the electron spin. Moreover, the spin has serious ramifications dividing particles in two distinct categories: the *bosons* which have integer valued spin, and the *fermions* which have half-integer valued spin. This separation is important due to the *Pauli exclusion principle* which states that *each fermion has its own unique wavefunction.* As a consequence, two fermions cannot share the same wavefunction! On the other hand, Pauli's exclusion principle does not say anything about bosons. That means many bosons can

have exactly the same wavefunction! In our discussion, we are not going to trace the origins of spin but will take it as a given fact which is going to be incorporated in the wavefunction by hand. Since spin is yet another kind of angular momentum one might ask the following: how does it interact with the other angular momenta, and in general how do the different angular momenta combine with each other? To answer these questions, we are going to introduce the total angular momentum operator, customarily denoted by $\hat{J}$, which is exactly what you might think it is; the sum of all the different angular momenta in a system. J is an angular momentum operator and also obeys eqs. (2.11) and (2.12) as well as eqs. (2.14) and (2.15).

$$j = |l - s|, |l - s| + 1, \ldots, l + s - 1, l + s \tag{2.14}$$

$$m_j = -j, -(j - 1), \ldots, (j - 1), j \tag{2.15}$$

Having used quantum mechanics to study the hydrogen atom and introduced the concept of spin, we are going to use these tools to tackle the next element in the periodic table, the helium atom.

2.4 The helium atom

In this section we are going to discuss the helium spectrum because we are using an excited helium atomic beam in our experiment. Unfortunately, helium proves to be more challenging than one might expect and seems to have one too many electrons for us to handle. As can be seen in eq. (2.16), the Schrödinger equation for helium looks similar to that of hydrogen, where each

electron has its own kinetic term and experiences an electrostatic attraction due to the nucleus. The last term in the equation describes the electrostatic repulsion between the two electrons; thus coupling the two electrons together.

$$E_n\psi_n = -\frac{\hbar^2}{2m}\sum_{i=1}^{2}\nabla_i^2\psi_n - \sum_{i=1}^{2}\frac{2e^2}{4\pi\epsilon_0 \boldsymbol{r_i}}\psi_n + \frac{e^2}{4\pi\epsilon_0|\boldsymbol{r_1}-\boldsymbol{r_2}|}\psi_n \tag{2.16}$$

Unfortunately, besides the hydrogen atom, for all other atoms, including helium, Schrödinger's equation is solved numerically. There are different approaches of how to deal with a many-electron system. The reader is encouraged to delve into the details of different approximations outlined in references [11], [14], [15]. For our purposes, we are presenting a subset of the experimentally measured energy levels for helium which were retrieved from NIST's atomic spectra database [13] and are presented in table 2.3. In table 2.3, we notice

Electron configuration	**Term symbol**	**J**	**Energy (eV)**
$1s^2$	$^1S_0$	0	00.000000
$1s2s$	$^3S_0$	1	19.819615
$1s2s$	$^1S_0$	0	20.615775
$1s2p$	$^3P^o$	2	20.964087
$1s2p$	$^3P^o$	1	20.964097
$1s2p$	$^3P^o$	0	20.964219
$1s2p$	$^1P^o$	1	21.218023
$1s3s$	$^3S_1$	1	22.718467
$1s3s$	$^1S_0$	0	22.920317
Ionization $1s$	$2S_{\frac{1}{2}}$	—	24.587389

Table 2.3: Experimentally determined energy levels for the helium atom retrieved from the NIST Atomic Spectra Database [13]. The energy levels are referenced with respect to the helium ground state.

a series of significant differences with table 2.2 which lists the hydrogen lev-

els. First of all, the first column describes the electron configuration, i.e the wavefunctions that the helium electrons are occupying. These wavefunctions correspond to the wavefunctions of hydrogen as if each atomic electron was moving around the nucleus by itself. As an example let's take the electron configuration 1s3p which indicates that one of the electrons has a principal quantum number $n = 1$ and orbital angular momentum $l = 0$, while the other has a principal quantum number $n = 3$ and orbital angular momentum $l = 1$. Here we are using all the knowledge we gained from studying the hydrogen atom to describe other systems for which we cannot analytically find a solution. It is also important to point out that the spin quantum number plays a more significant role for the helium atom energy levels. We can see that the ground state has both electrons in the s state. But we have just talked in section 2.3 about Pauli's exclusion principle which bans two fermions sharing the same wavefunction. In this case the two electrons have the same quantum numbers apart from their spin projection m_s. One of them has $m_s = \frac{1}{2}$ which we refer to as spin up or $\uparrow$ and the other electron has $m_s = -\frac{1}{2}$ which we refer to as spin down or $\downarrow$. Things get more interesting for higher energy levels. In table 2.3 there are two different energy levels corresponding to the electron configuration 1s2s, but have a different term symbol and total angular momentum J. The *term symbol*, ${}^{2S+1}L_J$, is a way to attribute a total spin, orbital, and total angular momenta to a multi-electron atom. The $2S + 1$ indicates the spin multiplicity, L indicates the total orbital angular momentum, and J indicates the total angular momentum we get when we combine L and S as

described in eqs. (2.14) and (2.15). For example, the state $^3S_1$ at $\sim$19.8 eV has spin $S = 1$, $L = 0$, and $J = |L + S| = |L - S| = 1$. This leads to three available values $m_j = -1, 0, 1$ and the state is refer to as a *triplet* state. On the other hand, the state $^1S_0$ at $\sim$20.6 eV has spin $S = 0$, $L = 0$, and $J = |L + S| = |L - S| = 0$. For this state there is only one available $m_j = 0$ value and the state is refer to as a *singlet* state. In our experiments, both the singlet and the triplet states of helium are present, but the triplet is assumed to be more prevalent. The term symbol is a useful concept for atoms where the spin-orbit coupling is a small perturbation to the energy levels of the atom [14]. This assumption breaks down as we get to heavier elements which have a lot of electrons. The term symbol provides the framework to understand how most atoms transition between energy levels.

2.5 Atomic transitions

In the above discussion we recognized the fact that there are different stationary states which correspond to specific energy levels. Nothing in our analysis indicates how we can transition from one state to other or why should we ever expect a system to spontaneously transition from one energy level to another. Nonetheless, in real life, we do experience the phenomenon of *spontaneous emission* which is precisely the transition from one energy level to another with a photon emission happening simultaneously as depicted in fig. 2.2. The emitted photon has energy that corresponds to the energy difference between the two participating energy levels. Over time the atom ends up

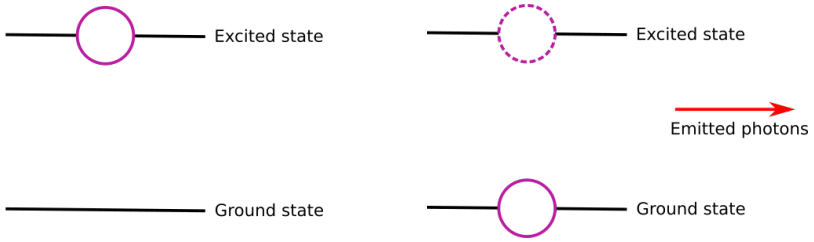

(a) The atom occupies an energy level located above another.

(b) The atom transitions to the lower energy level and a photon is emitted.

Figure 2.2: Spontaneous emission process.

in its lowest energy level, its *ground state*, even if that takes a long amount of time. Naturally, people wonder: what causes spontaneous emission, how can we hop from one state to another, and are all energy transitions accessible? Einstein provided a phenomenological explanation in which he described three different processes that could take place: *absorption*, *spontaneous emission*, and *stimulated emission*. Absorption is shown in fig. 2.3 and an atom initially in a low energy level absorbs a photon and transitions to a higher energy level. Similarly to spontaneous emission, the photon has to have energy equal to the energy difference between the two levels. Stimulated emission can be thought

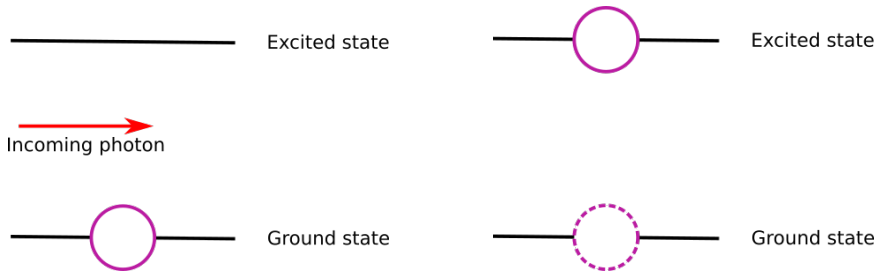

(a) The atom occupies a lower energy level and a photon is present.

(b) The atom absorbs the photon and transitions to the higher level.

Figure 2.3: Absorption of a photon by an atom.

of as a hybrid of the two aforementioned processes and is shown in fig. 2.4. In this scenario, a photon causes an atom to de-excite from a high to a low energy level emitting a second photon. The end result is the atom occupying the lower energy level and we have two photons with the same energy. With

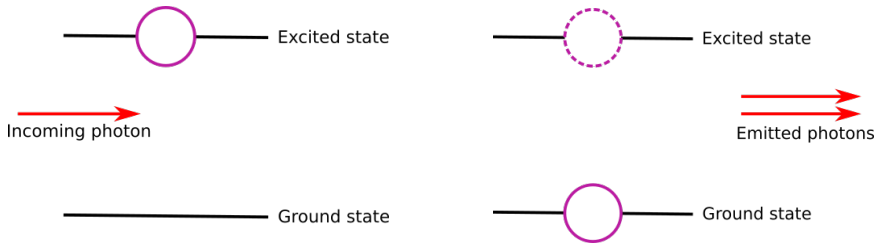

(a) The atom is in the excited energy level and a photon is present.

(b) The atom is in the ground state and two photons are present.

Figure 2.4: Stimulated emission process.

the development of quantum electrodynamics (QED) physicists were able to create a more robust theoretical framework in which these three processes arise organically. Roughly speaking, what causes the atom to spontaneously emit light and transition from a high energy level to a lower, are the fluctuations in the electromagnetic field of the vacuum. These fluctuations are a perturbation in the system's Hamiltonian causing the energy levels not to correspond to stationary states. For the full explanation and exposition to the mathematical details, the reader is encouraged to consult reference [16]. Even though we do have an explanation behind spontaneous emission, from early experimental measurements it became clear that only a subset of energy transitions were dominant and some were seemingly absent. As we always do in quantum mechanics, scientists revisited their knowledge from the pre-quantum era and

reformulated it in the quantum mechanics formalism. More specifically, scientists knew how radiation arises from an accelerating charged particle and tried to relate it to the motion of atomic electrons [9]. In the end, it was shown that not every energy transition can happen with equal probability. Ultimately the participating energy levels had to respect the symmetries present in the initial and final states. The most prevalent transitions, which are commonly referred to as *allowed transitions*, are those that obey the *electric dipole* transitions with lifetimes in the nanosecond to microsecond range. Higher order electric and magnetic multipole transitions do take place with lifetimes that span an enormous range of timescales. For this reason they are often referred to as being *forbidden transitions*, even though they do take place; albeit slowly. For more information, reference [17] provides a thorough analysis on energy transitions in atoms. Each transition category, whether it is an electric dipole transition or a magnetic octupole, obeys certain rules which mainly ensure that certain quantities are conserved. For the electric dipole the rules are $\Delta J = 0, \pm 1$, with the exception of $J = 0 \nleftrightarrow 0$, $\Delta M_J = 0, \pm 1$, and $\pi_f = -\pi_i$ where π is the level's parity [11]. An energy level's lifetime is defined as the amount of time that an atom will have a probability of e^{-1} to remain in the higher energy level. This quantity is intimately related through Heisenberg's uncertainty principle with the linewidth of the energy level. For this reason, even though *forbidden transitions* have longer lifetimes than *allowed transitions*, the former have much narrower linewidth making them ideal for certain applications. In some situations, atoms end up in an excited state and remain

there for a significant amount of time which is normally significantly longer than the duration of our experiment. These energy levels are called *metastable states* and their definition is not the most rigorous, but highly depends on the experimental situation. In our experiment we are using the an extremely long-lived metastable state, the helium triplet state $^3S_1$ with lifetime $\sim$7850 s [18], giving us ample time to do our experiment which last a couple of milliseconds.

2.5.1 Optical pumping

In section 2.5 we have seen how an atom can decay from a high to a low energy level by photon emission and the reverse process of absorption where a photon excites an atom from a low to a high energy level. The transition rules that dictate photon emission apply equally well to the reverse process, photon absorption. These processes are extremely important when one wants to create a beam of atoms occupying a certain energy level or a certain quantum number which in most cases is the magnetic quantum number m. The process of using light to force atoms in a certain state is called *optical pumping*. More specifically, optical pumping allows us to put atoms in a state with a non-zero magnetic quantum number m; thus the atoms have a nonzero magnetic moment. Using appropriate inhomogeneous magnetic fields, as it was the case in the Stern-Gerlach experiment, the trajectories of the atoms can be manipulated and more specifically the atomic beam can be focused as it is described in chapter 5. For more details regarding optical pumping the reader is encouraged to peruse references [19], [20].

2.6 Many-body systems: Molecules and solids

As it was mentioned in section 2.4, except from the atomic hydrogen, we cannot calculate the exact spectrum of any atom. If the situation looked bleak when we tried to deal with the helium, the situation becomes a pandemonium once we start trying to calculate the spectra of molecules, not to mention solids that consist of astronomically huge numbers ($> 10^{23}$) of electrons, protons, and neutrons. We can write down a Hamiltonian that exactly describes the interactions among all the participating particles, as well as their kinetic energies, but how do you solve such a massive system of equations? There must be another way around this issue and smarter ways for recasting our problem that are more conducive to numerical calculations and many of them are presented in reference [21].

2.6.1 Molecules

We start our discussion with the hydrogen molecule H_2 which, as its chemical formula indicates, consists of two hydrogen atoms. The Hamiltonian describing the hydrogen molecule system is given in eq. (2.17). The first two sums describe the usual kinetic energy terms for each component; thus we end up having four kinetic terms in total, two for the electrons and two for the protons. The other terms describe the Coulomb interaction among the

different particles.

$$\begin{aligned}\hat{H} = &- \frac{\hbar^2}{2m_e}\sum_{i=1}^{2}\nabla_{i,e}^2 - \frac{\hbar^2}{2m_p}\sum_{i=1}^{2}\nabla_{i,p}^2 \\ &- \sum_{i,j=1}^{2}\frac{e^2}{4\pi\epsilon_0|\boldsymbol{r_i^{(e)}} - \boldsymbol{r_j^{(p)}}|} \\ &+ \frac{e^2}{4\pi\epsilon_0|\boldsymbol{r_1^{(e)}} - \boldsymbol{r_2^{(e)}}|} + \frac{e^2}{4\pi\epsilon_0|\boldsymbol{r_1^{(p)}} - \boldsymbol{r_2^{(p)}}|}\end{aligned} \tag{2.17}$$

Solving the equation describing the hydrogen molecule is intimidating and we are not going to do it. Roughly speaking, one can start by first using the *Born-Oppenheimer* approximation which assumes that the motion of the nuclei can be treated separately from the motion of the electrons. The next step, uses combinations of the hydrogen wavefunctions that were presented in section 2.2 keeping in mind to respect Pauli's exclusion principle. The reader who does feel like spending an afternoon delving into the hairy details is strongly encouraged to consult references [22]–[24]. What we learn from the hydrogen molecule, which is confirmed experimentally, is that the hydrogen molecule has a discrete spectrum as it was the case with the hydrogen atom. Nevertheless, the molecular hydrogen spectrum is far more crowded with energy levels aggregating around certain locations. This is due to the fact that there are energy levels attributed to the rotational and vibrational states of the molecule. These energy levels are associated with the motion of the two nuclei with respect to each other and are significantly smaller than those associated with the electrostatic interaction among the electrons and the protons.

2.6.2 Solids

The dynamics of a hydrogen molecule, which has two electrons and two protons, are described in eq. (2.17) which has ten terms in total. In the general case where we have N interacting particles, the Schrödinger equation describing the system will have N kinetic terms (one for each particle) and $\binom{N}{2} = \frac{N(N-1)}{2}$ two-particle interaction terms; therefore the Schrödinger equation ends up having $\frac{N(N+1)}{2}$ terms. For a real macroscopic solid having $> 10^{23}$ particles, analytically solving the equation describing the system is impossible, and we have to approximate the system in various ways to make it computationally tractable. One of the simplest models is the *free-electron gas* model. The only particles present in our system are electrons which do not interact with each other [21]. In other words our system's Schrödinger's equation has only kinetic terms, one for each electron. The next step to solve the free-electron gas model is to use Pauli's exclusion principle, which forces every electron to have its own unique kinetic energy $E = \frac{\hbar^2 k^2}{2m_e}$; thus a given wave-vector $\boldsymbol{k} = (k_x, k_y, k_z)$ has at most two electrons ascribed to it, a spin up and a spin down electron. Each wave-vector $\boldsymbol{k}$ has to obey the boundary conditions of the system which are determined by the system's dimensions $L_x,\ L_y,\ L_z$ corresponding to the x, y, and z axis respectively. The boundary conditions force our wave-vector to take values $\boldsymbol{k} = (\frac{2\pi n_x}{L_x}, \frac{2\pi n_y}{L_y}, \frac{2\pi n_z}{L_z})$. Without any loss of generality and in order to simplify things we treat the system as a cube with dimensions $L_x = L_y = L_z = L$ turning the wave-vector components to $\boldsymbol{k} = \frac{2\pi}{L}(n_x, n_y, n_z)$. As a consequence, given N electrons, the ground state of

the system is nonzero since almost all of the electrons, apart from two, will have nonzero kinetic energy. In order to determine the ground state, we start attributing to each electron a wave-vector $\boldsymbol{k}$ and a spin starting from $\boldsymbol{k} = 0$ until we run out of electrons. The last occupied energy level is referred to as the *Fermi energy*, E_F, which is a fundamental concept not unique to the free-electron gas model that makes its appearance in other models. The Fermi energy is a quantity deeply embedded in condensed matter theory and crucial for our understanding of many-body systems! A quantity closely related with the Fermi energy is the *work function* which tells us the minimum amount of energy needed to liberate an electron from a solid. The work function can be thought of as the equivalent of the *ionization energy*, a quantity used for describing atoms and molecules, in solids.

In the free electron gas model, each energy level depends on the magnitude of the wave-vector; thus we can have multiple electrons corresponding to the same energy level as long as they have different spin or wave-vector. As it was discussed above, each wave-vector is uniquely defined by the discrete set of positive integers n_x, n_y, n_z. One might ask how many electrons can correspond to the same energy level? Due to the fact that in a real solid we have an extraordinary huge number of electrons, we move away from the discrete description of $\boldsymbol{k} = \frac{2\pi}{L}(n_x, n_y, n_z)$ and instead we adopt the continuous function $D(\boldsymbol{k})$ which we are going to refer to as the *density of states*. In k-space (wave-vector space), the density of states has the form presented in eq. (2.18).

$$D(\boldsymbol{k}) = 2\frac{V}{(2\pi)^3} \tag{2.18}$$

The two in front of the fraction on the right hand side is to account for the two spin directions and V is the volume of the system in the coordinate space. A hand-wavy explanation behind eq. (2.18) is the following. A unique state in k-space occupies a volume $\frac{2\pi}{L^3}$ since each point in k-space is $\frac{2\pi}{L}$ away from its nearest neighbors in all three directions. As the volume of the system, $V = L^3$, increases, the volume that a unique state occupies in k-space decreases by the same amount. As a result the discrete nature of the states can be approximated by the density of states $D(\boldsymbol{k})$ that gives us the number of particles $D(\boldsymbol{k})d^3k$ that occupy the k-space volume d^3k around the wave-vector $\boldsymbol{k}$. Fortunately, eq. (2.18) describing the density of states is a general expression which is not unique to the free-electron gas. Depending on the relation between energy and wave-vector $\boldsymbol{k}$, we can get the energy density of states form the density of states. Last remark, the *energy density of states* is an omnipresent concept in condensed matter physics that can be experimentally determined and can tell us a lot about a material's properties.

2.6.3 Other models for studying materials

We can clearly see that the free-electron gas cannot fully explain reality for the simple reasons that it excludes any interactions among the electrons and does not even mention the material's nuclei. As a result, different approaches have been developed trying to address this issue and the interested reader is once more encouraged to read reference [21] where many of those models are presented. A common feature across the different models is the departure away

from discrete energy levels, which was the situation with atoms and molecules, towards a discrete set of energy intervals. In essence, the only allowed energies that a system can adopt are only those that fall in the allowed energy intervals. Nevertheless, within an energy interval the system can take whatever energy value it wants. These energy intervals are called *energy bands* and all together as a collective are called *the band structure*. The energy bands are a direct consequence of *Bloch's theorem* which describes the motion of electrons in a periodic potential.

2.7 Conclusion

Reality is best described with quantum mechanics and most microscopic phenomena cannot be interpreted otherwise. This formalism was applied on the hydrogen atom, where we saw that the atom can take only certain energy values. Trying to solve the equation describing the helium atom ends up being impossible requiring us to employ numerical methods. This is not a unique situation to the helium, but actually is the case for all the remaining atoms. In real life atoms can transition from a high energy level to a lower by emitting a photon that corresponds to the energy difference between the two energy levels. Nevertheless, not every transition can happen with equal probability, with the energy transitions that obey the electric dipole rules being the most dominant. These transitions tend to have lifetimes somewhere in the nanoseconds to microseconds range. We can also have transitions that are extremely slow that for all intends and purposes can be treated as being

metastable. This is something that we take advantage of in our experiment where we use excited helium in $^3S_1$ state which has lifetime of $\sim$7850 s. In the same way atoms can go from a high to a low energy level by emitting a photon, the opposite process can also happen. Using light that corresponds to the energy difference between two energy levels we can place atoms into an excited state. Optical pumping, which is repeated photon absorption and emission by an atom, allow us to create a beam of atoms occupying a specific state. On a different note, quantum mechanics requires atoms and molecules of having their own unique, discrete energy spectrum. Nevertheless, the situation becomes more complicated for solids. Instead of having discrete energy levels, we have energy bands. Moreover, the last occupied energy is called the Fermi energy and the amount of energy it takes to remove an electron from the Fermi energy to the continuum is called the work function. Having seen the wealth of information that atoms, molecules, and solids have, how do we study their structure and access this information? One approach is outlined in the next chapter, where we present a technique that utilizes metastable neutral atoms to study materials.

Chapter 3

Electron emission spectroscopy techniques

In chapter 2 we developed the necessary framework for understanding the energy spectrum of atoms, molecules, and solids. We had also discussed the concepts of allowed and forbidden transitions as well as the process of optical pumping which allows us to use light to pump atoms into a certain energy level. Nevertheless, energy transitions can also happen through *nonradiative* processes, meaning an atom can get excited or de-excited without absorbing or emitting photons. This family of transitions is the underlying mechanism behind the metastable atom electron spectroscopy (MAES), the technique we are using for the majority of our experiments. In this technique, a metastable excited atom de-excites once it encounters a surface (or a gas atom) causing an electron emission that carries information about the density of energy states of the material. This information can be used to identify the elements present on a surface as well as some surface properties. Besides MAES, we also employed x-ray photoelectron spectroscopy (XPS), a technique that uses x-ray photons to excite core and valence electrons of a material allowing us to trace the elements present in the bulk and the surface of a sample.

3.1 Metastable atoms

We briefly discussed metastable excited atoms in section 2.5 where we alluded to the fact that metastable excited energy levels have long lifetimes, but we never concretely defined the boundaries. This was done on purpose because the defining timescale highly depends on the duration of the experiment we are trying to perform. Most atomic experiments take place on the order of a few milliseconds which means any excited state with a lifetime $>1\,\mathrm{s}$ qualifies as a metastable state. In our experiment, the timescale is determined by the time it takes for an excited atom to reach our sample which is $\sim 500\,\mu\mathrm{s}$ and we are using the helium triplet state $^3S_1$ with $\sim 7850\,\mathrm{s}$ lifetime [18], giving us plenty amount of time to perform our measurements.

3.1.1 Making metastable atoms

Metastable atoms can be created in various ways and some of them are listed in table 3.1. The various approaches are in discussed in detail in reference [25]. The first technique we are going to address is atom excitation via electron bombardment. In such an apparatus, an electron beam collides with the atoms of interest exciting a portion of the atoms. Electron bombardment allows us to excite select states by changing the energy of the electron beam. Unfortunately, it has a low efficiency due to the small cross-section in an atom-electron collision. The cross-section is so small that in order to excite atoms with a high efficiency our electron beam starts encountering space charge limitations [25]. The second technique, which is the one used in our

Technique	**Advantages**	**Disadvantages**
Electron bombardment	Tunability and relative ease of making the equipment	Low efficiency ($\sim 10^{-6}$)
Discharge	Easy to implement	Low efficiency and lack of selectability
Optical pumping	High efficiency	Expensive equipment and tedious implementation

Table 3.1: The advantages and disadvantages of select methods for creating metastable atoms.

experiment, is atom excitation via electric discharge. In such an apparatus, an atomic beam travels through electrodes. These two electrodes are biased at different voltages creating an electric field between them. Through random events, such as cosmic ray ionization or rogue electrons, electron and ion cascades take place which subsequently interact with our atomic beam leading to a portion of the atoms to be excited. A discharge source is significantly easier to build and implement in an experiment, but is plagued by low efficiency and lack of tunability. The experimentalists find themselves with an atomic beam containing various excited energy levels requiring further sieving. Lastly, optical pumping has the fine-precision to excite atoms at exactly the level of interest. There are two different approaches implementing optical pumping for creating metastable atoms. The first approach is to use enough power to overcome low excitation probability due to an energy level's long lifetime. The second approach is to use a combination of lasers which will allow a series of transitions leading to the targeted energy level. Even though optical pumping

is the most efficient way for producing metastable atoms, it requires a laser which tend to be expensive compared with the two previously mentioned approaches. Furthermore, a laser requires tuning in order to guarantee that the laser emits light at the right frequency. This process can be time consuming and in many cases lasers prove to be unstable requiring constant tuning.

3.2 Metastable atom-surface interaction

When a metastable atom comes close to a surface within a distance of $<10\,\text{Å}$, it falls down to its ground state almost with a probability close to unity. In most of the cases, this de-excitation phenomenon is followed by an electron emission. Depending on the material and the metastable atom we are using, there are different channels by which the atom de-excites [7], [26]–[30]. The location of the Fermi energy with respect to vacuum, the location of the metastable energy with respect to vacuum, and the unoccupied energy bands of the material determine which of the mechanisms can take place. The relevant concepts are illustrated in fig. 3.1.

3.2.1 Resonance ionization (RI) + Auger neutralization(AN)

When the Fermi energy of the sample is lower than the metastable level, the electron occupying the outermost shell in the metastable atom tunnels into an unoccupied energy level of the material as long as such an energy state exists. This causes the metastable atom to become a positive ion and this process is referred to as *resonance ionization* (RI) (see fig. 3.2a). As the

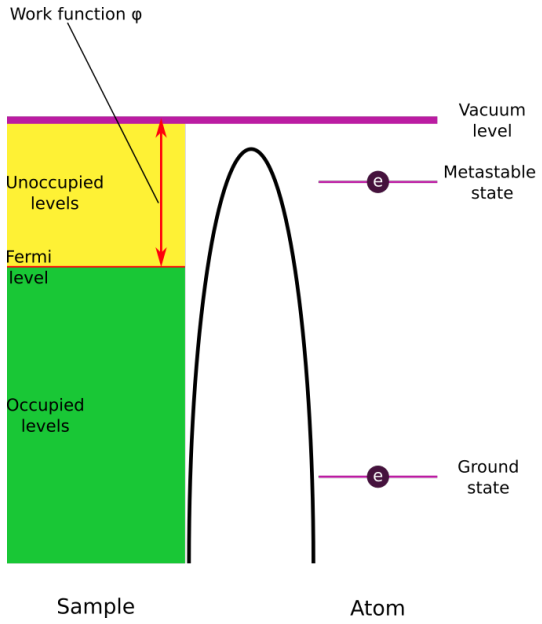

Figure 3.1: This figure illustrates the relevant concepts that dictate the metastable atom-surface interaction.

newly created ion gets even closer to the surface, a surface electron tunnels down to the ground state of the ion, thus neutralizing it, and a second surface electron is emitted. This process is called *Auger neutralization* (AN) (see fig. 3.2b) since the ion got neutralized and the whole process resembles an Auger process, where one electron makes a transition in order to fill a hole causing another electron's emission. During this two-step process we require for the total energy of the system to be conserved. Assuming negligible change in the kinetic energy of an atom, the emitted electron's kinetic energy needs

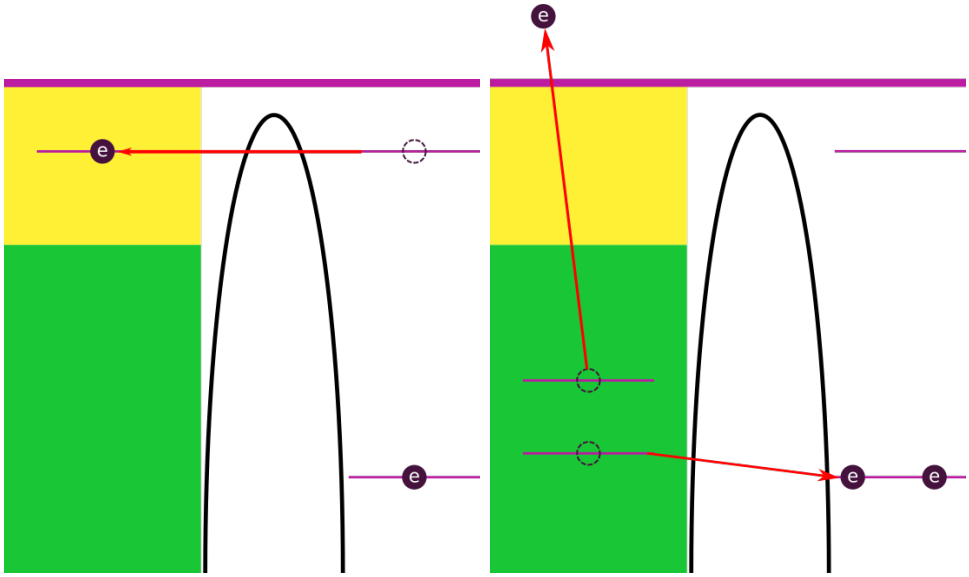

(a) The resonance ionization process where the outermost electron of the metastable atom tunnels into an empty energy state of the surface.

(b) The Auger neutralization process where a surface electron neutralizes the previously created ion and a second surface electron is emitted.

Figure 3.2: Resonance ionization followed by Auger neutralization.

to obey eq. (3.1).

$$\begin{aligned} E_k &= E^* - E_a - E_b \\ E_a &= \phi + \Delta - \epsilon \\ E_b &= \phi + \Delta + \epsilon \\ \Longrightarrow E_k &= E_i - 2\phi - 2\Delta \end{aligned} \tag{3.1}$$

where E_k stands for the kinetic energy of the emitted electron, E^* is the energy difference between the metastable and ground states of the incoming atom, E_i is the ionization energy of the neutral atom, E_a is the energy level that the surface electron occupied before it was emitted, E_b is the energy level of the surface electron that ended up tunneling into the ion, ϕ is the work

function of the sample, Δ is the average energy of E_a and E_b, and ϵ is the energy difference from E_a and E_b to Δ. It is important to remember that all energy levels are measured with respect to the vacuum level which signifies the boundary between the continuum, where electrons are unbound and can move freely, and the bound states of the atom and the solid. An important consequence of eq. (3.1) is that electrons occupying different energy levels can correspond to ejected electrons with the same kinetic energy as shown in fig. 3.3. As a result, the measured spectrum gets broadened requiring further analysis to extract the relevant information. Another important consequence

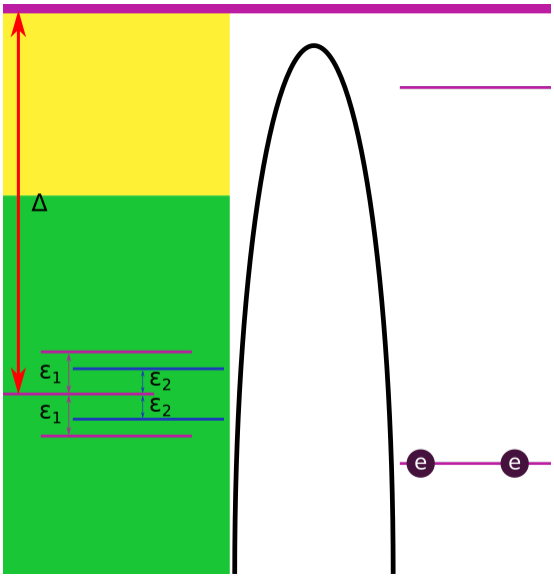

Figure 3.3: Two different combinations of energy levels that can lead to an ejected electron with the same kinetic energy.

of eq. (3.1) is the maximum kinetic energy an emitted electron can have is $E_k^{max} = E_i - 2\phi$. This situation corresponds to the case where both surface electrons are sitting exactly on the Fermi level. As a ballpark most metals have

a work function $\sim$4 eV. In our experiment we are using metastable helium which has ionization energy 24.6 eV, which leads to $E_k^{max} = 16.6\,\text{eV}$. Now if instead of helium we used metastable xenon whose ionization energy is 12.13 eV then $E_k^{max} = 4.13\,\text{eV}$. Using an atom with higher ionization energy allows us to probe a broader energy range of the surface states. This is one of the many reasons why helium is used in the vast majority of MAES experiments.

3.2.2 Auger de-excitation (AD)

On the other hand, if there are simply not available surface energy levels, such as in the case of an insulator where the metastable level falls in the band gap as shown in fig. 3.4a, or if the Fermi energy is higher than the metastable energy level, such as in materials with low work function as shown in fig. 3.4b, things take a different course. In this scenario, as the metastable atom approaches the surface, a surface electron tunnels in the atom's ground state causing the atom's outermost electron emission. This process is referred to as *Auger de-excitation*(AD) since the metastable atom de-excite to its ground state and we had once again an Auger-like process as in the previous scenario. This one step process is shown in fig. 3.5. Similarly with the previous scenario, we demand that the total energy of the system is conserved, neglecting any change to the atom's kinetic energy, as illustrated in eq. (3.2).

$$\begin{aligned} E_k + E_i - E^* &= E_i - E_a \\ \Longrightarrow E_k &= E^* - E_a \end{aligned} \tag{3.2}$$

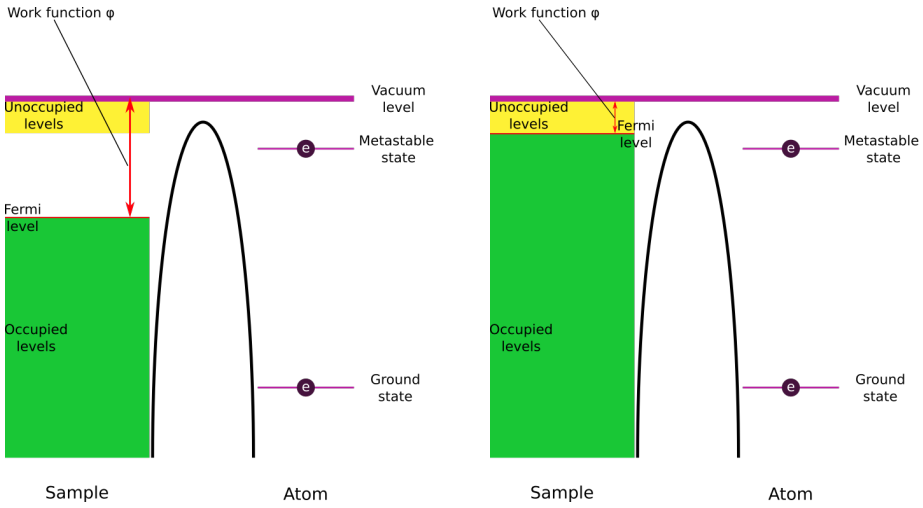

(a) Interaction between a metastable atom and a surface of an insulating material.

(b) Interaction between a metastable atom and a surface with low work function.

Figure 3.4: Materials that can undergo Auger de-excitation.

where E_k is the kinetic energy of the emitted electron, E^* is the energy difference between the atom ground and the metastable states, E_i is the atom's ionization energy, and E_a is the surface electron energy with respect to vacuum. This quasi-one electron emission in principle allows us to determine the energy density of states. This is due to the one-to-one correspondence between the kinetic energy of the emitted electron and the energy occupied by the surface electron before it tunneled.

3.2.3 General comments regarding MAES

From the above mechanisms we can see that the electron emission takes place concurrently or after a tunneling event with the metastable atom being

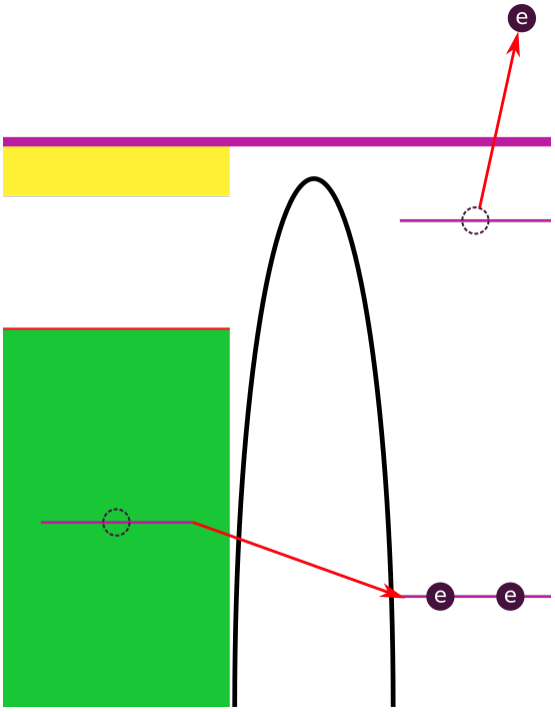

Figure 3.5: The Auger de-excitation process where a surface electron tunnels into the ground state of the atom and the outermost electron of the atom gets ejected.

only a few Angstroms away from the surface [7], [29], [30]. This implies that the metastable atoms probe almost exclusively the topmost surface atoms making MAES a surface-sensitive technique. As a result, MAES can be compared with other surface sensitive techniques such as scanning tunneling spectroscopy. Nevertheless, it is important to keep in mind that in MAES like any other electron emission spectroscopy techniques, there are also secondary electrons. Those are electrons that have either been emitted inwards to the solid and underwent multiple collisions before they escaped the sample, or electrons that were emitted as a result of the inwards emitted electrons. Having secondary

electrons reduces the surface sensitivity of the technique. Nevertheless, the majority of the secondary electrons have significantly lower kinetic energies than the primary emitted electrons allowing us to separate almost completely the two contributions. Further discussion about secondary electrons in MAES can be found in references [30], [31]. Another important point, is that electron emission in MAES is not isotropic. The majority of electrons are emitted along the normal to the surface as pointed out in references [32], [33]. Another crucial point is that the energy levels of the atoms shift as they approach a surface and vice versa. This is due to the fact that the atom-surface interaction becomes a significant perturbation in the overall system's Hamiltonian. In essence, we cannot treat the combined system's Hamiltonian as the addition of the sample's Hamiltonian with that of the atom's. As a result, the energy levels of an isolated atom are approximations to the ionization and metastable energy levels of the atom in the presence of a nearby surface. In most situations we can get the right results by using the approximation $E_i' \approx E_i - 2\ eV$ in place of the ionization energy and assuming that the metastable energy level has not shifted [7], [29], [30]. Lastly, almost the entire population ($> 99\%$) undergoes de-excitation once they encounter a surface. However, each de-excitation event does not yield an emitted electron and this is an unanswered phenomenon.

3.2.4 Advantages and disadvantages of MAES

MAES is an appealing spectroscopy technique for studying materials mainly due to its surface sensitivity. Additionally, typical MAES experiments

use atomic beams with kinetic energy $\sim$100 meV. Such amount of energy is not enough to break most chemical bonds which tend to be of the order of 1 eV. As a result, samples do not get damaged due to the beam impact. Nevertheless, the atom does release its internal energy which is somewhere in the 10 eV to 20 eV range. Such an amount of energy is enough to damage a material, but long exposures to bright beams are required [34], [35]. Another point in favor of MAES is the fact that it can be used for studying surfaces that cannot be studied using other surface sensitive techniques. More specifically, scanning tunneling spectroscopy cannot be used for studying insulators of arbitrary thickness; although STM can study thin insulating films as long as detectable tunneling currents can be established. Therefore, MAES can be applicable for studying surfaces of insulating materials regardless of how thick they are, with the following caveat. In MAES, electrons leave a sample and if a sample is insulating that causes charge accumulation over time. A way around this issue is to use a flood gun which is a source of low-energy electrons with the sole purpose of neutralizing the sample. Using a flood gun does not guarantee that the sample will be completely neutral, but this is the best way to achieve almost perfect charge neutrality on a surface. Another useful aspect of MAES is that the atoms used in MAES experiments can be optically pumped in different magnetic levels allowing us to study surface spin dynamics. Unfortunately, we are not able to freely tune the energy levels of the atoms in an atomic beam, since the energy spectrum is an intrinsic property of an atom. Such a tunability can be useful if one is interested to study the effect

of metastable energy levels on the emitted electron spectra. Of course this can be done using different atomic species, but this still leaves a big energy gap unexplored between metastable energy levels of different atoms. Lastly, MAES experiments are performed using noble gas atoms which once they de-excite are chemically inert and do not react with the sample. This has the benefit of leaving the sample in a pristine condition.

3.3 X-ray photoelectron spectroscopy (XPS)

In addition to MAES, we have also used x-ray photoelectron spectroscopy (XPS) for some of our experiments. The reader is highly encouraged to read reference [36] in order to get a good overview of the field. The basic mechanism behind XPS is the photoelectric effect. A photon can liberate an electron free from a solid if the photon has at least a certain amount of energy as can be seen in eq. (3.3).

$$E_k = E_\gamma - E_B - \phi = hf - E_B - \phi \tag{3.3}$$

E_k is the kinetic energy of the liberated electron, $E_\gamma = hf$ is the energy of the incoming photon with frequency f, h is Planck's constant, E_B is the binding energy of the electron in the solid, and ϕ is the work function of the material. The binding energy E_B is the energy difference between the initial state (n-electron state) and the final state((n-1)-electron state) (see eq. (3.4).

$$E_B = E_f(n-1) - E_i(n) \tag{3.4}$$

Using Koopmans' theorem, the emitted electron's binding energy equals its energy level before its emission. The assumption behind Koopmans' theorem is that the photoelectron process happens significantly faster than the time it takes for the remaining electrons and ions in the solid to rearrange. This is a relatively good approximation giving theoretical values close to the experimentally observed ones. In real life, the remaining electrons and ions in the solid do change their configuration in response to the photoelectron emission causing a correction to the binding energy term. This correction is referred to as the *relaxation energy*. Besides the relaxation energy there are other corrections due to the solid's final state such as the electron-electron correlation and relativistic effects which both tend to be minor. A more significant correction term is the *chemical shift*. The chemical shift indicates the chemical environment the atom is embedded in. This can be used as a proxy to determine chemical changes that take place intentionally or unintentionally during our experiment. The chemical shift can be used to probe how a certain chemical environment influences a given element.

3.3.1 Background

Following a photoelectron emission, the electrons in the solid do eventually re-arrange resulting either in an Auger electron emission or x-ray emission in order to conserve energy. Both processes contribute to background signal. Furthermore, x-rays penetrate almost the entire sample causing photoelectron emission at various depths. Depending on its kinetic energy, the emitted elec-

tron can suffer multiple collisions; thus losing energy before it exits the sample. The number of collisions a photoelectron can have is encapsulated in its *inelastic mean free path*, which depends on the photoelectron's kinetic energy. Using Beer's law eq. (3.5), we can determine the number of electrons that can escape from a certain depth without undergoing any collisions.

$$I = I_0 e^{-\frac{d}{\lambda \cos\theta}} \tag{3.5}$$

The measured intensity of the electron beam that exits the sample is I with initial intensity of I_0. The electron beam originated at a depth d from the surface and was emitted at an angle θ with respect to the surface's normal. λ stands for the inelastic mean free path (IMFP).

3.3.2 Advantages and disadvantages of XPS

XPS is a powerful technique for determining not only surface chemical composition, but also the composition of the bulk. Furthermore, synchrotron facilities can provide bright and tunable x-ray sources; allowing one to study materials at different x-ray energies. Unfortunately, there are few solutions for making optical elements for x-rays. Most of the existing solutions for adjusting the spot size of an x-ray beam cause a reduction to the beam intensity. Besides the lack of x-ray optical elements, due to the secondary electrons and to a lesser degree to the photoemission process, XPS causes material damage. This is discussed in more detail in chapter 4. Lastly, XPS is not a surface-sensitive technique as a consequence of primary photoelectrons originating from various depths in the sample.

3.4 Conclusion

Electron emission spectroscopy techniques are the bread and butter of material scientists. These techniques allow us to determine the chemical composition and properties of a given material. No technique can do everything a scientist might want. This necessitates one to use a combination of different techniques to achieve their desired goal. In this chapter we have spent most of our focus on presenting MAES, the main technique used in our experiments. MAES allows us to study the surface of a material without inducing significant damage. It can be applied on any kind of material regardless its conductivity, as long as we maintain the sample's charge neutrality. We have also gave an overview of XPS, one of the powerhouses of the electron emission spectroscopy techniques. XPS is widely used because it allows chemical composition determination for both the surface and the bulk of a material. It also enables one to study the chemical environment in a material and how that changes under certain conditions. XPS causes damage on samples and scientists need to consider this when they deal with sensitive samples.

Chapter 4

Damage on organic materials

In this chapter we are going to briefly discuss damage to organic materials. Our starting point will be an overview of chemical bonds, including their formation and classification. In this overview we will encounter two different theoretical frameworks: the *valence bond* (VB) theory and the *molecular orbital* (MO) theory. Following this review, we will begin with self-assembly of alkanethiol molecules which create well-ordered structures on gold. We present this specific platform because they are easily grown, encapsulate many characteristics of organic materials, and are used in sensing applications. Next, we discuss damage and how the micro-scale phenomena give rise to the macro-scale effects we experience. We focus on damage caused by electron-matter and photon-matter interactions. The chapter concludes discussion on ways by which damage may be slowed, prevented, or healed.

4.1 Chemical bonding

4.1.1 Lewis structures and valence bond theory

When an atom is in its ground state, one can determine the principal and orbital angular momentum for every one of its electrons using the *Aufbau*

principle which relies on the Pauli principle (see section 2.3) and Hund's rules [14]; although there are some exceptions particularly for heavy nuclei. In essence, we use the hydrogen atom wavefunctions to label each electron of a heavier atom with a wavefunction as if the other electrons were not present (see section 2.4). Once every electron has been assigned their corresponding n and l the collective assignment is the *electron configuration* of a given atom. For example, a hydrogen (H) atom's ground state has only one electron and it occupies the *1s* state; thus it's configuration is *1s*. In the case of helium where there are two electrons, the electron configuration is $1s^2$ with the superscript indicating the number of electrons in that n, l state. Moving a bit higher to carbon (C), the ground state configuration is $1s^2 2s^2 2p^2$. All the states with the same principal quantum number (the number in front of the letters) correspond to the same *shell*. The last shell in an electron configuration is called the *outermost shell* and the electrons belonging to the outermost shell are called *valence electrons*. In 1916, Gilbert N. Lewis introduced the idea of electron-pairs and a visualizing method that uses dots to denote the atom's valence electrons [37]. According to Lewis, an atom will bond with another atom such that each atom's outermost shell will have eight electrons (or two for the $n = 1$ K-shell). This means that atoms with unfilled outer shells will form bonds in order to mutually fill their shells. Lewis used dots to indicate the number of valence electrons in an atom's outer shell as demonstrated below:

Using this representation, two or more atoms can form bonds either by sharing their valence electrons leading to a *covalent bond* or one atom donating and the other receiving valence electrons leading to an *ionic bond*. For example, the hydrogen molecule (H_2) is represented using the Lewis structure H:H or H–H, where the valence electrons are shared between the two atoms and the dash stands for the bond due to this sharing. A couple years later, Lewis's framework was recasted as the *valence bond (VB)* theory using the quantum mechanics formalism. Since then, the valence bond theory has undergone a lot of transformations and has fallen in disrepute; nevertheless, various concepts developed through the valence bond formalism are entrenched in chemists' parlance and provide an intuitive picture.

One idea stemming from valence bond theory is *orbital hybridization* with carbon being the poster child of this concept. Carbon's ground state electron configuration is $1s^2 2s^2 2p^2$ which means only the two electrons in the *2p* state are able to pair up, thus one would expect that carbon can form only two bonds. Nevertheless, we do observe molecules in which carbon forms four single bonds as in the case of methane (CH_4). One way people explained the ability of carbon to form four bonds is by assuming that carbon adopts the slightly different electron configuration $1s^2 2s 2p^3$ when it tries to bond. Using the hydrogen wavefunctions (see eq. (2.6)), we can derive the wavefunctions

describing the p states according to equations eqs. (4.1) to (4.3).

$$\psi_n^{p_x} = \frac{1}{\sqrt{2}}(\psi_{n,1,1} + \psi_{n,1,-1}) \qquad \propto x \tag{4.1}$$

$$\psi_n^{p_y} = \frac{i}{\sqrt{2}}(\psi_{n,1,1} - \psi_{n,1,-1}) \qquad \propto y \tag{4.2}$$

$$\psi_n^{p_z} = \psi_{n,1,0} \qquad \propto z \tag{4.3}$$

The reason for introducing wavefunctions eqs. (4.1) to (4.3) is so we can have wavefunctions that are proportional to the Cartesian coordinates x, y, z. This way it is easier to identify how the electron pairs will form in the coordinate space. The next assumption, responsible for the name of this whole process, is that the wavefunctions describing the valence electrons are a blend of the *2s* wavefunction and the three wavefunctions described by eqs. (4.1) to (4.3). The hybrid wavefunctions belong to the sp^3 hybrid orbital and explain the structure of the methane molecule. For further discussion about hybrid orbitals, including the sp and sp^2 hybrid orbitals, see reference [11].

Besides orbital hybridization, valence bond theory introduced the concept of *resonance* which simply states that in cases where there are more than one Lewis structure describing the system, the real molecule is a superposition of all those equivalent Lewis structures, with benzene (C_6H_6) being a good example. According to valence bond theory, a benzene molecules consists of six carbons connected in a circle. Each carbon atom is connected with a single bond one one side and a double bond on the other side with its neighboring carbon atoms, as shown below.

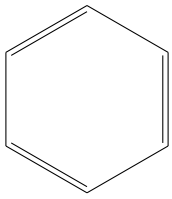

However, the following structure is equally valid for a benzene molecule:

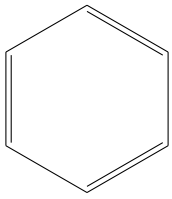

According to valence bond theory, the actual benzene molecule is a superposition of the above structures. Lastly, most chemical bonds are best described as a superposition of covalent and ionic bonds, instead of just being purely one or the other. Over the years, valence bond theory had had many successes, but eventually faced certain obstacles forcing scientists to play closer attention to an alternative approach developed almost concurrently with valence bond theory which we turn to next.

4.1.2 Molecular orbital theory

An alternative approach to the valence bond theory is the *molecular orbital (MO)* theory, which abandons the idea of electron-pairs in favor of delocalized electrons distributed over the entire molecule. The starting point is to construct wavefunctions by combining atomic orbitals derived in the absence of the other atoms in the molecule. During this step, we once again use the hydrogen wavefunctions (see eq. (2.6)) to create these atomic orbitals. Using

linear combination of atomic orbitals for all the valence electrons participating in the molecule, one gets electron orbitals that extend over the entire molecule. In essence, we assign a wavefunction for each electron from each atom in the molecule and add them all up. The end result is a molecular orbital that an electron can occupy. Similarly with valence bond theory, we start filling up all the molecular orbitals using the Aufbau principle until we run out of electrons. Molecular orbitals are categorized as *bonding* if the majority of the electron cloud falls between the paricipating nuclei, and *antibonding* if the majority of the electron cloud falls mostly outside the space between the nuclei [38]. A bonding molecular orbital creates a bond, whereas an antibonding negates one. If a molecular orbital is symmetric about the axis connecting the two nuclei then it is called a *sigma* (σ) molecular orbital. These molecular orbitals can be formed using wavefunctions with zero angular momentum corresponding to s orbitals, although one can also use orbitals with $l = 1$ and $m = 0$ which correspond to p_z orbitals. A molecular orbital is called a *pi* (π) molecular orbital if it is antisymmetric around the axis connecting the two nuclei. Last comment in nomenclature, an antibonding molecular orbital is indicated with an asterisk. For instance, a sigma antibonding orbital is indicated as σ^* and a pi antibonding orbital as π^*. Bonding orbitals do not take any superscripts so a bonding sigma orbital is just σ and a bonding pi orbital is π. Orbital hybridization is also adopted in molecular orbital theory in order to reconcile experimental results with the theory. This is an indication that molecular orbital theory has its own pitfalls and requires adjustments in order to develop

a reliable algorithm that outputs trustworthy results. An appealing feature of molecular orbital theory is that it tries to use the same ideas behind atomic structure to molecular structure. In the same way one talks about atomic energy levels and energy transition causing light emission, one can also talk about molecular energy levels and measure the emitted light due to transitions between molecular energy levels.

4.1.3 Bond energy and bond dissociation energy

Bond energy refers to the *average bond energy* associated with a certain bond, whereas *bond dissociation energy* refers to the amount of energy it takes to break a chemical bond between two atoms in a particular environment [39]. The main premise behind this difference is due to the fact that as a polyatomic molecule disintegrates the nuclei and electrons rearrange themselves shifting the energy associated with each bond. For example, it takes 9.62 eV to break water into its three constituents, two hydrogen atoms and an oxygen atom. One would assume that the two bonds each will require half of the total value, 4.82 eV. Nevertheless, it takes 5.17 eV to break the first bond and 4.45 eV to break the second [40]. Some bond dissociation energy values are presented in table 4.1 with typical values ranging from 3 eV to 5 eV. The bond dissociation energy is the enthalpy change corresponding to the homolytic reaction shown in eq. (4.4) at 298 K [40], [41].

$$AB \rightarrow A + B \tag{4.4}$$

One can clearly deduce from this definition that the dissociation energy is a temperature dependent quantity.

Bond	**Bond dissociation energy (eV/bond)**
H —— H	4.51[a]
H_2O	5.17[a]
OH	4.45[a]
CH_4	4.56[a]
CH_3CH_2 —— H	4.38[a]
CH_3 —— CH_3	3.91[b]
Br —— $C_{10}H_7$	3.43[b]

Table 4.1: Bond dissociation energies for different bonds in certain molecules. The initial values were either quoted in kcal/mol or $\mathrm{kJ\,mol^{-1}}$ and we used the conversion $100\,\mathrm{kcal/mol} = 418.4\,\mathrm{kJ\,mol^{-1}} \rightarrow 4.34\,\mathrm{eV/bond}$. [a] ref. [40], [b] ref. [41].

4.1.4 Intermolecular forces

The interactions between different molecules known as *intermolecular forces*, are responsible for the structure found in liquids and solids. Intermolecular forces are due to electrostatic interactions between molecules. More specifically, they are due to electric multipole interactions, magnetic multipole interactions (which tend to be small), and Pauli's exclusion principle which prevents electrons and protons occupying the same wavefunction creating a repulsion at small distances. From table 4.1 we have seen that typical dissociation energies due to the internal structure of the molecule are $\sim$3 eV to 5 eV, whereas bonds due to intermolecular forces tend to be weaker by an order of magnitude. Intermolecular forces are split in two categories: *long range* and

short range. Long range interactions have an R^{-n} dependence, with R being the internuclear separation, whereas short range interactions have an e^{-aR} dependence [42]. As a result, it requires significantly less energy to break the latter bonds. The reader is encouraged to read reference [42], [43] for an in-depth discussion. These forces are behind the self-assembly process described in section 4.2 and also for the adsorption of thiol molecules on graphene as shown in section 4.2.1.

4.2 Self-assembled monolayers

Various organisms exhibit self-organizing behavior, like migrating birds and schools of fish. This mechanism is also present in the microcosm where atoms and molecules do assemble and organize themselves. In this section we are going to discuss how alkanethiol molecules self-assemble in well ordered monolayers on a gold surface. Alkanethiols are hydrocarbon chains with a sulfur-hydrogen group on one end, the *head*, and a functional group on the other end, *the tail*. The carbon chain between the head and the tail ends is called the *backbone*. In our experiments, we have used two different alkanethiols and both had an eleven long carbon backbone. More specifically, we used ethanol solutions of 11-bromo-1-undecanethiol $Br(CH_2)_{10}CH_2SH$ and 1-dodecanethiol $CH_3(CH_2)_{10}CH_2SH$. In the majority of our experiments, we used a gold coated silicon wafer as our substrate and for the rest we used a graphene monolayer deposited on top of silicon oxide SiO_2. A cartoon version of a monolayer formation due to self-assembly of alkanethiol molecules on gold

is depicted in fig. 4.1. Even though there is no clear picture of the reaction

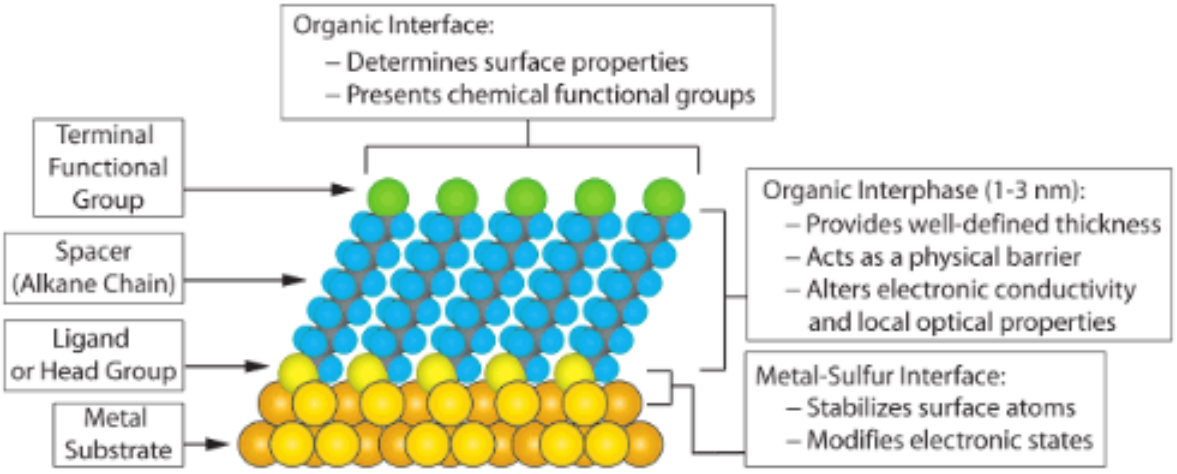

Figure 4.1: Ideal formation of a self-assembled monolayer. The green spheres are the tails or terminal functional groups of each alkanethiol molecule. The blue and grey spheres together comprise the backbones of the alkanethiol molecules. The smaller yellow spheres are the heads (sulfur-hydrogen group) of the molecules. Figure taken from reference [44].

pathway via which the sulfur atom forms a bond with the gold surface, self-assembled monolayers do form reliably on a gold substrate [44], [45]. It has been found that the gold-thiolate bond has a bond dissociation energy in the range 1.74 eV to 2.17 eV [44], [46] which is a relatively strong bond allowing the alkanethiolate molecules to stay anchored on the substrate.

Self-assembly takes place in two stages: the first stage that lasts seconds and the second stage that lasts hours. Several attempts have been made, both experimentally and theoretically, to better understand the kinetics of self-assembled monolayers [47], [48]. The way molecules organize themselves depends on the surface coverage [48], [49]. At the very early stages when most

of the surface is pristine and uncovered, only a few molecules are adsorbed on the surface and they are lying flat on the surface. As more molecules adsorb to the surface, the newly adsorbed molecules attach their head groups on sites with other neighboring molecules' head groups and this stage is called the *pin stripe phase* [49]. Later on, the neighboring alkyl chains start getting on top of their neighbors and subsequently the alkyl chains start standing up in coordination with their neighbors. Finally, each molecule's backbone interacts via intermolecular forces with its neighbor causing all the molecules to tilt at a certain angle. The energy associated with the intermolecular interactions among the backbones is $\sim$0.6 eV(value corresponds to hexanethiol [46]). As pointed out in reference [45] and from the bond values mentioned previously in this paragraph, the strong interaction of sulfur with gold (1.74 eV to 2.17 eV) in comparison with the interaction between the molecules' chains facilitates the self-assembly. In essence, the intermolecular forces are not strong enough to cause the molecule to desorb from the surface and allow the neighboring molecules to coordinate in a standing tilted structure.

4.2.1 Self-assembled monolayers on graphene

Part of our project was to study the role the substrate can play in preventing damage and more precisely how the substrate's conductivity reduces the induced damage. In reference [8], it was argued that graphene can be the ideal candidate due to its high electron mobility allowing the organic molecules to replenish electrons from the substrate as it loses electrons due to photon

and electron exposure. Previous researchers have attempted to interface alkanethiols with graphene [50]–[52] having technological applications in mind. In reference [52] they grew 1-octadecanethiol on graphene and found that the alkanethiol molecules were laying flat and parallel to each other. This is in stark contrast with self-assembled monolayers on gold which are standing up. Although, if a gold substrate does not spend enough time in the thiol solution one can find a layer of flat-laying alkanethiol molecules.

4.2.2 Verifying self-assembled monolayers

The presence of self-assembled monolayers and the degree of organization may be inferred using Fourier Transform Infrared Spectroscopy (FTIR) [53], [54] (see fig. 4.2). Besides FTIR, x-ray photoelectron spectroscopy [4]

Structural group	**C-H stretching mode**	**Peaks** (cm^{-1})
CH_2	Asymmetric	2919
CH_2	Symmetric	2851
CH_3	Asymmetric in-plane	2965
CH_3	Symmetric	2937
CH_3	Symmetric	2879

Table 4.2: FTIR peaks for 1-dodecanethiol ($CH_3(CH_2)_{11}SH$). The values were taken from reference [53].

and metastable atom electron spectroscopy [55], [56] (see fig. 4.3) have been used to characterize self-assembled monolayers. FTIR provide us with sharp features that can indicate both chemical and structural information. For this reason, we had used FTIR for characterizing our samples and determining their quality. The values corresponding to a self-assembled monolayer of 1-

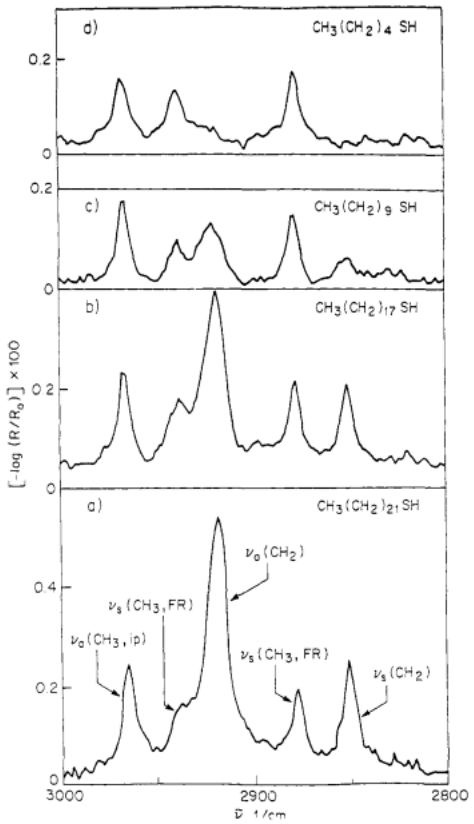

Figure 4.2: FTIR spectra using p-polarized light incident at 86° for self-assembled of different alkanethiol chain length. Each peak corresponds with different parts of the alkanethiol molecules. Data taken from reference [53].

dodecanethiol $CH_3(CH_2)_{11}SH$ are shown in table 4.2.

4.2.3 Applications

Self-assembled monolayers are a popular platform that has found many applications. Scientists are attracted to the fact that they can change the monolayer's functionality by choosing the appropriate tail group [44], [57]. Doing so one can control an entire surface's functionality. There have also

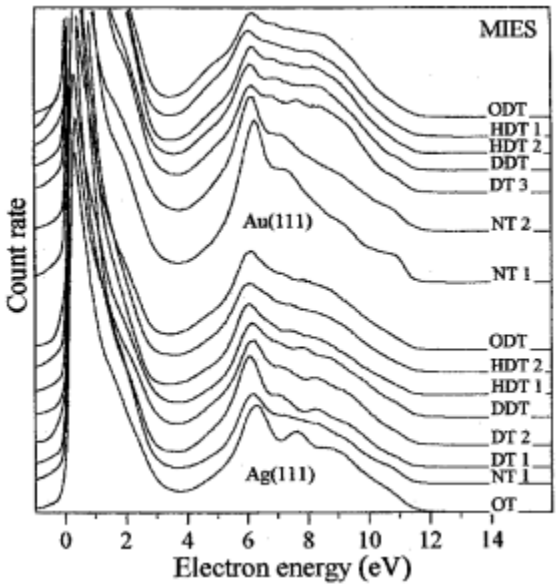

Figure 4.3: Spectra for self-assembled monolayers of alkanethiols on Au(111) and Ag(111) at120 K. Figure was taken from reference [55].

been proposals to use self-assembled monolayers as field-effect transistors [58], as well as sensors for toxic materials such as mercury [52] and cadmium [59] and as biosensors [60]. Another technological application is using self-assembled monolayers as resists for nanolithography [34], [61]–[67]. In order to make lithography efficient and reliable it is useful to understand the mechanisms responsible for damaging self-assembled monolayers.

4.3 Damage

Most of us are familiar with damage caused by photon exposure (sunburns), high temperatures (melting of a plastic bag), and impact (sledgehammer breaking a wall). Fundamentally, damage is due to the breaking of molec-

ular bonds. It is worthwhile to keep in mind that damage is not always unwelcome. For instance, photon and electron lithography are essential for electronic device manufacturing and hinges on the ability to effectively damage a resist [68], [69].

As photons, such as x-rays and ultraviolet light, or charged particles, such as ions and electrons, traverse a material, they deposit energy. Photons can get absorbed causing an excitation, ionization, or dissociation event. They can also experience *Compton scattering* where the photon loses some energy and the electrons of the material get a momentum kick. Photons can also go through a material without any interaction which happens with x-rays. Reference [70] goes in detail about the different phenomena observed due to photon damage. Hans Bethe developed eq. (4.5) which determines the energy-loss rate for a charged particle's energy as it travels through a material. The variables present in eq. (4.5) are explained in table 4.3.

$$-\frac{dE}{dx} = \frac{4\pi}{m_e c^2}\frac{N_A Z\rho}{AM_u\beta^2}\left(\frac{e^2}{4\pi\epsilon_0}\right)^2\left[\ln\left(\frac{2m_e c^2\beta^2}{I(1-\beta^2)}\right)-\beta^2\right] \tag{4.5}$$

Bethe's equation works well for high energies, but for energies $\leq$100 kV one should use modified versions [71], [72]. This energy deposition causes electron emission which, on its own, contributes to the overall damage. Reference [73] provides an in-depth discussion regarding damage due to exposure to an electron beam. Both photon and electron beams cause local heating upon impact which can also contribute to a material's deterioration. Bond breaking events for long molecules can cause fragmentation into smaller molecules, which is

Symbol	Variable
E	Electron's instantaneous energy
x	Distance along electron's path
m_e	Electron mass
c	Speed of light
N_A	Avogadro's number
Z	Material's mean atomic number
ρ	Material' mean density
A	Material's mean atomic weight
M_u	Molar mass constant
β	$\frac{v}{c}$ where v is the electron's velocity
e	Electron charge
ϵ_0	Permittivity of free space

Table 4.3: Variables that appear in eq. (4.5)

referred to as *chain scission*. In many cases, the newly created fragments can bond with each other creating an even bigger molecule than before. This effect is called *cross-linking*.

4.3.1 Damage to self-assembled monolayers

Damage to self-assembled monolayers has been extensively studied mainly due to interest of using self-assembled monolayers as resists for technological applications. In most cases, researchers exposed the samples to electron beams [2], [5], or photons [74]. Interestingly Zharnikov et al [3], saw a similarity between a damaged sample due to x-ray exposure and of that exposed to electrons, leading them to conclude that the majority of the damage is done by the secondary electrons. In our experiments we used metastable atoms to determine the induced damage due to electron impact triplet state $^3S_1$ releases

19.8 eV upon impact which is comparable with the helium He I ultraviolet photons which have 21.2 eV. Indeed metastable atoms do cause damage to self-assembled monolayers as has been shown in [34], [35], [63], [65], [66], [75]. In the case of helium, according to [34], a few metastable helium atoms are needed to damage one surface molecule. Having said that, if a surface has $\sim 1 \times 10^{15}$ atoms/cm^2 that means we need at least 1×10^{15} He*/cm^2 to damage the surface. In our experiment, our atomic beam has $\sim 6 \times 10^8$ He*/pulse requiring 10^7 pulses before a sample with 1 cm^2 cross section gets completely damaged.

4.4 Healing damage

Currently, we cannot study sensitive materials, such as DNA and proteins, without damaging or significantly altering them. Charge accumulation, as a result of electron emission due to electron and photon impact, is one of the mechanisms leading to material degradation due to Coulomb explosion. A potential solution is to use a substrate with high conductivity that can readily provide free electrons helping the sample to restore charge neutrality. Fill et al. [8] suggested that graphene is best suited for this task due to its extremely high electron mobility compared with typical conductors. On a similar note, Sader et al. [76] demonstrated high quality transmission electron images of sensitive samples which were frozen in ice and were supported on graphene. They attributed the enhancement in image quality to the charge reduction that accumulates on the ice that encloses the sample as a result of

the graphene's high conductivity. There are reasons to suspect graphene might not completely mitigate damage. For starters, self-assembled monolayers seem to attach to graphene via intermolecular forces which are significantly weaker than the gold-sulfur bond. Therefore, even if the molecules of interest do not get damaged by impinging photons or electrons, there is a high probability they will desorb from the surface. Furthermore, Zhou et al [6] showed that the substrate conductivity plays a crucial role in damaging a self-assembled monolayer. Nevertheless, they also determined the monolayer's structure plays a more significant role. More specifically, disordered monolayers were found to be more susceptible to damage. Another important finding from their work was that well-ordered self-assembled monolayers on doped GaAs (resistivity $\sim 1 \times 10^{-5}\,\Omega \cdot \mathrm{m}$), seemed to be equally protected to electron induced damage compared with well-ordered monolayers on gold (resistivity $3.8 \times 10^{-8}\,\Omega \cdot \mathrm{m}$). This indicates that the substrate's conductivity might play a role down to a certain resistivity. Even if graphene proves to be a good solution for electron and photon induced damage, a graphene substrate will not be able to prevent sputtering damage due to heavier particle, such as ions and neutral atoms. On a different note, graphene might prevent damage at the interface of the sample and the graphene, but the bulk of the sample will not benefit from graphene's high electron mobility. Lastly, the charge carrier density for graphene is lower than most conductors which might lead to a situation where there are not enough free charges to maintain a sample's neutrality as it is exposed to electrons or photons.

4.5 Conclusion

In this chapter, we presented the concept of a chemical bond and the main theories describing it: valence bond and molecular orbital theory. We have also introduced the bond dissociation energy which tells us how much energy is needed to break a bond. Following that, we presented the main mechanisms behind self-assembled monolayers of alkanethiols. In the last section, we addressed the notion of damage and its underlying mechanisms. At the very last section, we investigated how can one prevent damage on organic samples by an appropriate choice of a substrate. Ultimately we want to identify a viable platform for studying organic materials without altering their structure and allowing indefinite probing without damaging.

Chapter 5

Electron and Atom Optics

The field of optics, for the most part, deals with how to affect particle trajectories whether those are photons, electrons, or neutral atoms. All three categories share similar concepts, such as lens systems and mirrors, but each of them also exhibits some unique properties. For instance, electrons repel each other via the Coulomb interaction causing the so called space charge limitation. The goal of this chapter is to present some basic concepts of electron and atom optics and how we used them to construct instrumentation necessary for our experiments, like our home-made electron gun, and how we are using some of those concepts to construct aberration corrected atom lenses for an atom microscope.

5.1 Photon optics

5.1.1 Optical elements

Our discussion will start with photon optics since most terminology and concepts used by charged and neutral particle optics stem from photon optics. The three major elements in optics are lenses, mirrors, and apertures with lenses being probably the most important of the three. The working principle

behind lenses is Snell's law which is described in eq. (5.1) and illustrated in fig. 5.1. Snell's law relates the incidence angle θ_i of a light ray as it travels through a medium with index of refraction n_i, to the exit angle θ_o of the ray traveling through a medium with index of refraction n_o [77].

$$n_i \sin\theta_i = n_o \sin\theta_o \tag{5.1}$$

The most important quantity describing a lens is its *focal length f*. The focal

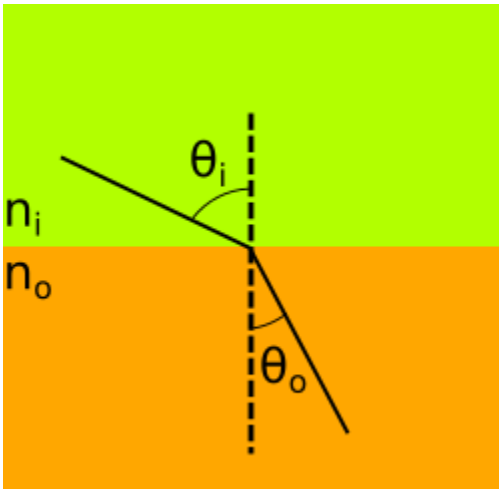

Figure 5.1: A light ray traveling from a material with index of refraction n_i to a material with index of refraction n_o. The light ray forms an angle θ_i with the normal at the two materials interface as it enters the boundary and θ_o as it exits.

length is the distance from the lens where a collimated beam is focused to a point. Having said that it is important to point out that there are two kinds of lenses: *converging* and *diverging*. A converging lens (see fig. 5.2) takes a collimated beam on one side and outputs a converging beam on the other side. A diverging lens (see fig. 5.3) does exactly the opposite. It takes a collimated

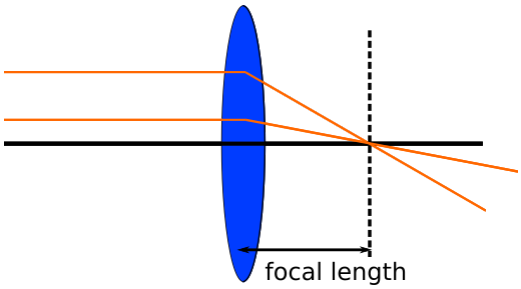

Figure 5.2: The effect of a converging lens on a collimated beam of light.

beam on one side and outputs a diverging beam on the other side. One might reasonably wonder "how is the focal length defined for a diverging lens?" In order to minimally alter the definition for the case of a diverging lens, we extend the diverging light rays that are coming out of the output side in the region of the input side until they all meet at a point. The distance from this point to the lens is the diverging lens's focal length and it is a negative number. Besides focusing a collimated beam down to a point, lenses are used

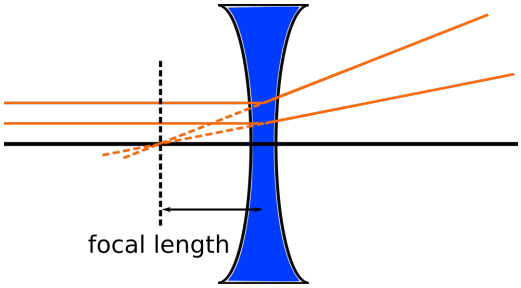

Figure 5.3: The effect of a diverging lens on a collimated beam of light.

most of the time to image objects. In the thin lens approximation [77], an object at a distance s_o from a lens with focal length f is imaged on the other side of the lens at a distance s_i away from the lens according to eq. (5.2). The

distances s_i and s_o are the *object distance* and the *image distance* respectively and M (see eq. (5.3)), is the *magnification* indicating the ratio of image's size to that of the object's. The negative sign in front of the magnification formula indicates an inverted image.

$$\frac{1}{f} = \frac{1}{s_i} + \frac{1}{s_o} \tag{5.2}$$

$$M = -\frac{s_i}{s_o} \tag{5.3}$$

Another important quantity characterizing a lens is the *numerical aperture (NA)*, described in eq. (5.4), which tells us the biggest input angle from the optical axis, θ_i^{max}, a ray traveling in a medium with index of refraction n_i can have in order to be captured by the lens.

$$NA = n_i \sin \theta_i^{max} \tag{5.4}$$

The next thing one can do with lenses is combine them in order to achieve either variable magnification or variable image distance. A good example is a combination of two converging lenses with focal lengths f_1 and f_2 respectively, separated by $L = f_1 + f_2$. Assuming $f_1 < f_2$, a collimated beam entering the first lens with diameter d_1 will exit the second lens with a diameter $d_2 = \frac{f_2}{f_1} d_1$ and remain collimated. Besides lenses, we often use apertures in an effort to select which light rays end up being imaged. This may be done to block light from unwanted sources or to control the *depth of field (DOF)*. The depth of field is the deviation from an object's distance that will create a relatively focused image. This definition is rather vague and subjective, but one can see

that an image taken with a camera with a big aperture makes the background appear blurry in comparison with an image taken with a smaller aperture. Lastly, mirrors are another important component in photon optics and they are governed by equation $\theta_i = \theta_o$ where θ_i and θ_o are the incoming and outgoing angles with respect to the surface normal, respectively. Mirrors can be used for creating a focused or dispersed beam and the reader is encouraged to read reference [77] for more details.

5.1.2 Aberrations

Unfortunately real lenses are not as perfect as presented and there are different factors limiting the ability to perfectly focus a beam at a single point. These effects are collectively referred to as *optical aberrations*. For a given lens, light of different wavelenghts will experience different focal lengths, a phenomenon referred to as *chromatic aberrations*. Chromatic aberrations are due to the material's dispersion function dependency on wavelength. Some other common aberrations are *spherical aberrations* where rays at different radii from the optical axis are focused at different locations, and *astigmatism* where rays from two perpendicular planes have different focal lengths. There are of course many more sources of optical aberrations and we wanted to provide an overview of some common ones. Even if we make lenses that are able to eliminate aberrations, the wave nature of light prevents us from focusing a beam of light down to a point. The diffraction limit, as explained by Abbe's criterion, limits the resolution we can achieve with photons down to the

scale of the wavelength used; thus using visible light with wavelength ∼400 nm will allow us to resolve structures down ∼200 nm. This was the main impetus pushing scientists, who wanted to study atoms which have sizes ∼0.1 nm, to develop electron microscopes.

5.2 Electron optics

As mentioned above, electron microscopes and the relevant charged particle optics were developed in an effort to probe materials at the atomic scale. A thorough exposure to charged particle optics can be found in [78], [79]. The majority of charged particle optics has been developed using classical electrodynamics theory and more specifically using the Lorentz force (see eq. (5.5)). The Lorentz force formula states that a charged particle with charge q and velocity $\boldsymbol{v}$, experiences a force $\boldsymbol{F}$ proportional to the electric field $\boldsymbol{E}$ and magnetic field $\boldsymbol{B}$.

$$\boldsymbol{F} = q(\boldsymbol{E} + \boldsymbol{v} \times \boldsymbol{B}) \tag{5.5}$$

One will notice that the two contributions, electric and magnetic, cause different behaviors on a charged particle. On one hand, the magnetic component is always perpendicular to the particle's trajectory causing no change to the particle's kinetic energy as can be seen in eq. (5.6).

$$\begin{aligned} W &= \int \boldsymbol{F} \cdot \boldsymbol{dx} \\ \boldsymbol{F} \cdot \boldsymbol{dx} &= F dx \sin\theta,\ \boldsymbol{F_B} \perp \boldsymbol{dx} \\ \Longrightarrow W_B &= 0 \end{aligned} \tag{5.6}$$

Nevertheless, the magnetic component can change the particle's trajectory causing it to move in curved trajectories. One who is interested in measuring a charged particle's kinetic energy will be naturally inclined to utilize magnetic fields in order to maintain the particle's kinetic energy. However, making a magnetic lens system for imaging is not a trivial affair. For this reason, electrostatic lens systems tend to dominate the field of charged particle optics. Unlike a magnetic field, an electric field can change both the trajectory and kinetic energy of a particle. A good example illustrating this point is an electron moving in a constant electric field. For the sake of simplicity the trajectory of one electron having velocity pointing in the y-axis and experiencing the force of an electric field pointing in the x-axis is illustrated in fig. 5.4. The trajectories

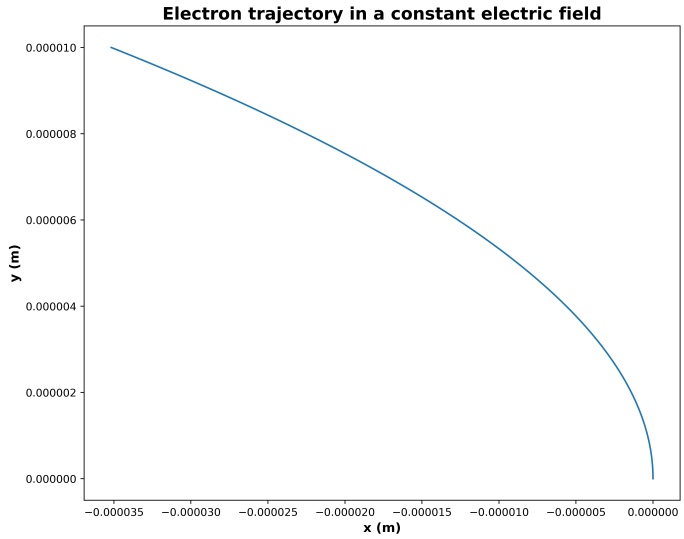

Figure 5.4: Trajectory of an electron with initial velocity $\boldsymbol{v} = 500\,\mathrm{m\,s^{-1}}\ \hat{y}$ moving in an electric field $\boldsymbol{E} = 1\,\mathrm{V\,m^{-1}}\hat{x}$.

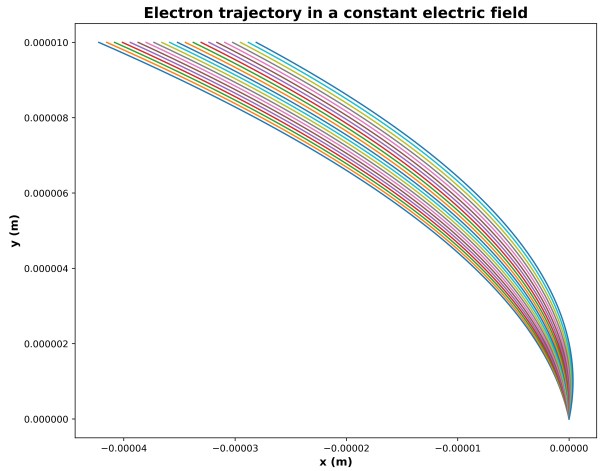

Figure 5.5: Trajectories of electrons with different initial velocities moving in an electric field $\boldsymbol{E} = 1\,\mathrm{V\,m^{-1}}\hat{x}$. Each electron moves with a speed of $500\,\mathrm{m\,s^{-1}}$ with different initial direction.

of a divergent electron beam being deflected by a constant electric field are shown in fig. 5.5. The motion of charged particles in a constant electric field is almost an analogous situation to a mirror in photon optics. In our experiment we have utilized this concept (see section 6.2.4) in order to deflect ions from our atomic beam.

5.2.1 Electron lens

The most common way to create an electron lens with a cylindrical symmetry analogous to optical lenses is to use two cylinders biased at different voltages. For a configuration where the separation s between the two cylinders is significantly smaller than the radius R of the two cylinders ($s \ll R$) the

electrostatic potential in the region between the two cylinders is given by eq. (5.7):

$$\Phi(r,z) = \frac{V_1 + V_2}{2} + \frac{V_2 - V_1}{\pi} \int_0^\infty \frac{I_0(tr)}{I_0(tR)} \frac{\sin tz}{t} dt \tag{5.7}$$

where r is the radius from the optical axis, z is the distance parallel to the optical axis, V_1 is the potential on the first cylinder, V_2 is the potential on the second cylinder, and I_0 is the zero-order modified Bessel function [79]. A common configuration of electrostatic lenses is to bias the first and last electrodes at the same voltage, while adjusting the voltages of the electrodes in-between. Such a configuration is called an *einzel lens* or a *unipotential lens* [79]. In an einzel lens, charged particles enter and exit the lens with the same kinetic energy; however, their trajectories are altered. The trajectories of a collimated beam of electrons with kinetic energy 200 eV entering an einzel lens are shown in fig. 5.6.

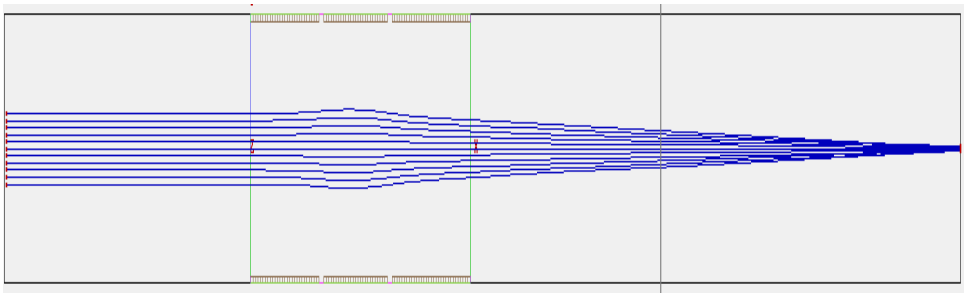

Figure 5.6: SIMION simulation of electrons with kinetic energy 200 eV entering an einzel lens from the left. The first (left) and third (right) electrodes are both at 0 V and the second (center) electrode is at 110 V. In this configuration, the electrons are focused to a point while retaining their initial kinetic energy.

5.2.2 Electron gun design

A simple design of an electron gun (see fig. 5.7) consists of three electrodes: the *cathode*, the *Wehnelt cylinder*, and the *anode*. The cathode is the source of the electrons and can be biased at different voltages. The Wehnelt cylinder is placed right in front of the electron source in order to control the beam size at the source. A small source comes at the expense of beam current and vice versa. Additionally, the anode allows us to determine the beam's kinetic energy and divergence. Of course, most electron guns employ a series of electrodes in order to control as much as possible the kinetic energy, size, current, and monochromaticity of the produced electron beam. This design was used to develop the electron gun (see section 6.3.4) that was used to damage our samples.

5.2.3 Electron analyzers

Electron analyzers play a relatively simple role: they filter the collected electrons based on their kinetic energy. That is they detect the number of emitted electrons in a given energy interval. There are many different designs for electron analyzers; however, we are going to concentrate our discussion around the hemispherical electron analyzer design due to the fact that this is the kind used in our experiments. An excellent review discussing the various designs can be found in [80]. For every electron analyzer, the name of the game is to achieve high energy resolution while collecting as many electrons as possible. A high electron number corresponds to a high sensitivity. Unfortu-

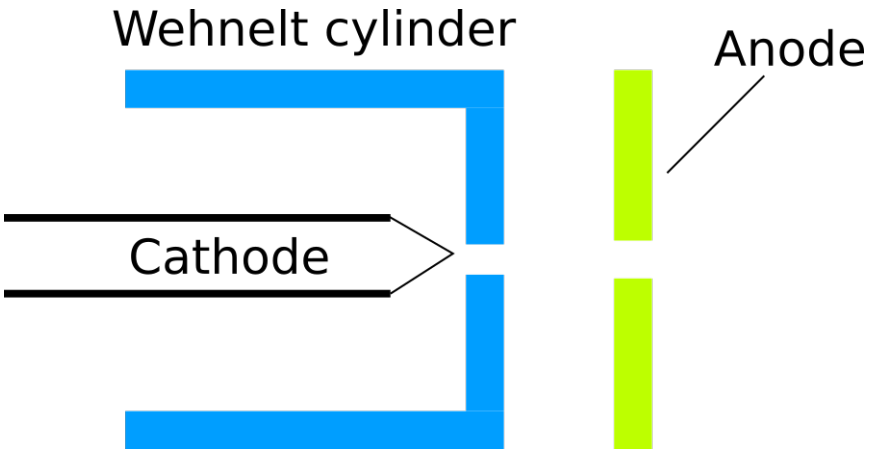

Figure 5.7: Design of a three electrode electron gun. Electrons are emitted from the tip of the cathode (left electrode). Typically the cathode floats at a high negative voltage. The Wehnelt cylinder (center electrode) is normally at a voltage slightly more negative than the cathode. By adjusting the voltage at the Wehnelt cylidner we can change the size of the source of electrons. The anode (right electrode) is normally at ground and determines the beam's kinetic energy and divergence.

nately, these two requirements actually compete with each other and one has to choose between high signal to noise ratio at the expense of energy resolution and vice versa. Nevertheless, most electron analyzers incorporate a series of electron lenses in an effort to increase their sensitivity. This collection of electron lenses also adjusts the kinetic energy and trajectories of the electrons either to make detection easier or to enhance resolution. In a hemispherical analyzer, the electron lens focuses the electron beam at a slit placed between two hemispheres with a potential difference such that only electrons within a certain energy range could go around and exit through another slit and finally get collected by a detector. The energy resolution of a hemispherical analyzer

obeys eq. (5.8) according to [80].

$$\Delta E = E_p \left(\frac{d}{2R_0} + \frac{\alpha^2}{4} \right) \tag{5.8}$$

where ΔE is the energy full-width-half-maximum around the energy we are probing at, E_p is the pass energy which is the kinetic energy of the electrons as they enter the entrance slit, d is the entrance and exit slit opening (we assumed the slits have the same dimensions), R_0 is the average radius of the two hemispheres, and α is the maximum half angle with which the electrons enter the slit. Hemispherical analyzers can be operated in two different modes: fixed pass energy analyzer transmission (FAT) and fixed ratio retardation (FRR). In the FAT mode, electrons get focused at the entrance slit and at the same time are retarded such that the electrons with the correct kinetic energy will be decelerated to the pass energy right before they enter the hemispheres. In this mode, we have the advantage that the energy resolution is constant in the entire data acquisition process, thus a spectrum is taken with the same energy resolution. The disadvantage of this mode is that the electron lens images bigger or smaller areas of the sample depending on the kinetic energy we are currently investigating. This is a problem in situations when we care about probing a specific region in a sample. In FAT mode, both the resolution and the sensitivity are fixed giving higher intensities at low kinetic energies and low intensities at high kinetic energies due to conservation of phase space volume [80]. In the FRR mode, the electron lens and the hemispheres are biased such that the ratio $\frac{E_k}{E_p}$ of incoming kinetic energy to pass energy is kept constant. The main advantage of this mode is that we are always probing the same

region of a sample. The main disadvantage is that energy resolution depends on the kinetic energy we are investigating as a consequence of a changing pass energy; thus peaks at different kinetic energies are acquired at different energy resolutions. Lastly, this mode has reduced sensitivity for low kinetic energies where it has high energy resolution and high sensitivity at high kinetic energies where it has low energy resolution. In our experiments we chose to operate in the fixed pass energy mode in order to keep the energy resolution the same for all energies.

5.3 Atom optics

Atom optics is the extension of principles from photon and charged particle optics to atoms. Atom optics use electric fields, magnetic fields, and light (electromagnetic fields) to guide atoms. One can think of the Stern-Gerlach experiment as the starting point of atom optics. As a reminder, in the Stern-Gerlach experiment atoms of silver ($J = \frac{1}{2}$) passed through an inhomogeneous magnetic field and experienced a force whose direction depended on the atoms' magnetic state ($m_j = \pm\frac{1}{2}$). One can therefore combine optical pumping (see section 2.5.1) to place atoms in the right magnetic state with inhomogeneous magnetic fields to exert forces on atoms in order to create the atom analogue of a lens. The force due to an inhomogeneous magnetic field is

shown in eqs. (5.9) to (5.13) below:

$$U = -\boldsymbol{\mu} \cdot \boldsymbol{B} \tag{5.9}$$

$$|\boldsymbol{\mu}| = -g_{jl} m_j \mu_b \tag{5.10}$$

$$U = g_{jl} m_j \mu_b |\boldsymbol{B}| \tag{5.11}$$

$$\boldsymbol{F} = -\boldsymbol{\nabla} U \tag{5.12}$$

$$\boldsymbol{F} = -g_j m_j \mu_b \boldsymbol{\nabla} |\boldsymbol{B}| \tag{5.13}$$

where U is the potential energy, μ is the atom's magnetic dipole moment, $\boldsymbol{B}$ is the magnetic field, g_{jl} is the Landé g factor, m_j is the magnetic quantum number, and $\boldsymbol{F}$ is the force exerted on the atom. The Landé g factor g_{jl}, as shown in [9], can be calculated using eq. (5.14):

$$\begin{aligned} g_{jl} &= 1 + (g_e - 1)\left(\frac{j(j+1) - l(l+1) + s(s+1)}{2j(j+1)}\right) \\ g_e &\approx 2 \\ s &= \frac{1}{2} \end{aligned} \tag{5.14}$$

The above expressions are valid in the small magnetic field regime ($|\boldsymbol{B}| < 10\ G$). Another important assumption is that the atoms' magnetic moments *adiabatically follow* the magnetic field lines such that their magnetic moments maintain their orientation with respect to the local magnetic field. Mathematically speaking the requirement is $\omega_z \gg \frac{|\frac{d\boldsymbol{B}}{dt}|}{|\boldsymbol{B}|}$ where $\omega_z = \frac{\mu B}{\hbar}$ is the Larmor frequency of an atom with magnetic moment μ in a magnetic field with magnitude B [81]. In an early effort, researchers build an atom lens using a hexapole configuration made out of permanent magnets [82]. A hexapole configuration

approximates a harmonic potential close to the optical axis ($r < \frac{r_0}{2}$) since the magnitude of the magnetic field is $|\boldsymbol{B}| \propto r^2$ [83]. Their results are illustrated in fig. 5.8. One of the issues that, according to them, hindered the lens's performance was the fringe field at the boundaries of the lens. To that end, our lab proposed to resolve this issue by using a pulsed electromagnet hexapole lens [84]. My former colleagues, Drs. Jamie Gardner and Erik Anciaux, were

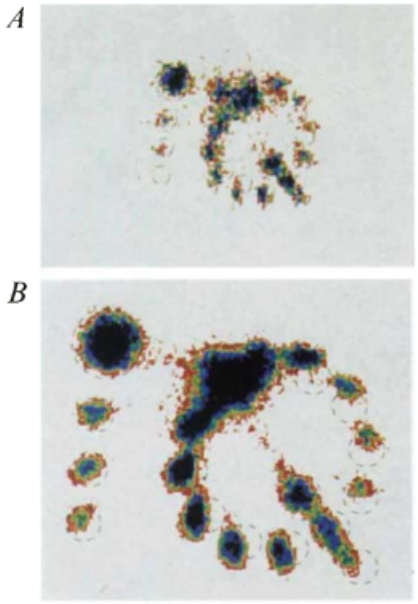

Figure 5.8: Imaging an atomic beam using a hexapole of permanent magnets. Image a) shows magnification 0.8 and image b) shows magnification 1.4. The figure was taken from reference [82].

able to use a pulsed electromagnetic hexapole lens to image an atomic beam going through apertures of various shapes [85]. Their results are shown in fig. 5.9 where we can see the images coming to focus as a function of the current passing through the hexapole lens. As it was mentioned above, besides

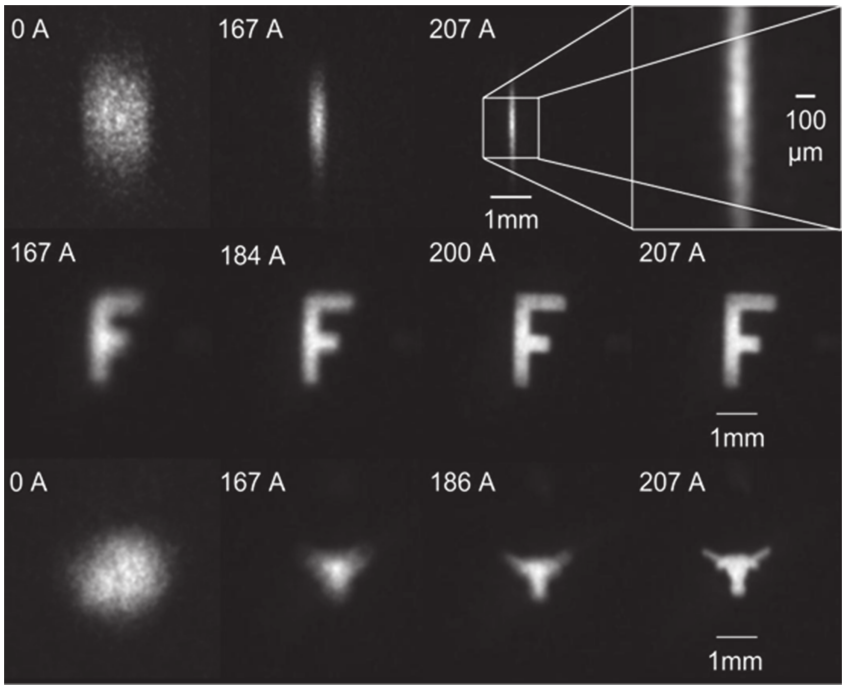

Figure 5.9: Imaging an atomic beam using a pulsed electromagnetic hexapole lens. The atomic beam went through apertures of various shapes, such as the Batman symbol and a longhorn, and were imaged on an MCP detector.

pure magnetic fields one can use laser light to affect atom trajectories. A photon with wavelength λ carries a momentum given by eq. (5.15). One can therefore imagine using photons to transfer momentum to atoms and change their trajectories. However, the momentum transfer is most efficient when the photons are in resonance with an atomic transition.

$$\boldsymbol{p} = \hbar \boldsymbol{k} = \hbar \frac{2\pi}{\lambda} \hat{k} \tag{5.15}$$

Using two counter-propagating beams with wave-vector $k = \frac{c}{\omega}$, with a frequency detuning $\delta = \omega_0 - \omega$ from an atomic transition that corresponds to a frequency ω_0 and lifetime γ one can create a damping force proportional to

the atom's velocity according to eq. (5.16).

$$\begin{aligned} \boldsymbol{F}_{\pm} &= \pm\frac{\hbar\boldsymbol{k}\gamma}{2}\frac{s_0}{1+s_0+(2\frac{\delta\mp|\omega_D|}{\gamma})^2} \\ \boldsymbol{F} &\approx \frac{8\hbar k^2\delta s_0\boldsymbol{v}}{\gamma\left(1+s_0+(\frac{2\delta}{\gamma})^2\right)^2} \end{aligned} \tag{5.16}$$

where $s_0 = \frac{I}{I_{sat}}$ with I being the laser intensity and I_{sat} being the saturation intensity, ω_D is the atom's Doppler shifted atomic transition frequency due to the atom moving with velocity $\boldsymbol{v}$ [81]. My colleague Dr. Erik Anciaux and I combined the focusing effect of a magnetic hexapole lens with two-dimensional transverse cooling to create an atomic beam with increased brightness [86] and our results are shown in fig. 5.10. Despite the successes of our experiments, our lens systems could not achieve resolution better than $\sim$100 µm for a couple of reasons. One of the obstacles we faced was the strong dependence that the lens's focal length has on the atoms' longitudinal velocity component. More specifically, the focal length obeys the relation $f \propto v_l^2$ for a permanent magnet hexapole and $f \propto v_l$ for a pulsed electromagnetic hexapole as long as the atoms spend the duration of the pulse inside the lens [83]. As a consequence, atoms with different longitudinal velocities will have different focal lengths. Furthermore, as the atomic beam propagates the slower atoms eventually accumulate behind the faster atoms. Our approach to resolve the aforementioned issues was by tapering our lens, that is having the lens wires further away from the optical axis at the entrance and closer to the optical axis at the exit [84]. An image of the proposed tapered lens is shown in fig. 5.11. Unfortunately, implementing this solution has faced various challenges. For

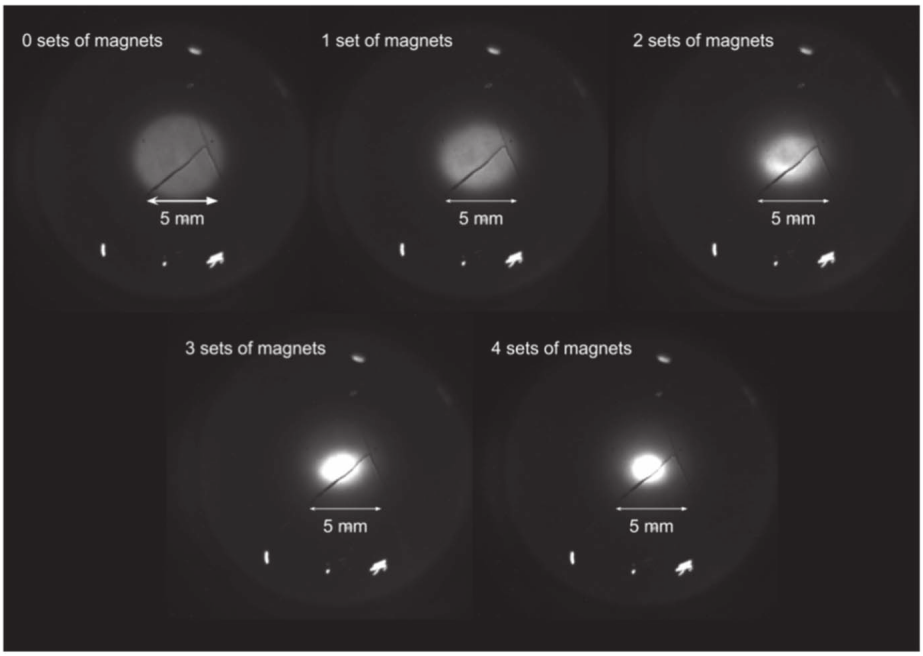

Figure 5.10: Brightening of an atomic beam using a permanent hexapole configuration followed by transverse laser cooling. Each image shows the beam spot size at our detector as we increased the length of our hexapole magnets.

starters, the ambient magnetic field, the wire locations with respect to each other, and the wire connectors create two minima close to the axis of propagation. An ideal lens will have only one minimum and that will coincide with the axis of propagation. The overall solution is to use pairs of Helmholtz coils to correct for all those effects since they seem to exhibit the same character. Lastly, we have not found a robust way of making a tapered lens with the necessary precision and we are currently exploring alternative manufacturing techniques such as 3D printing.

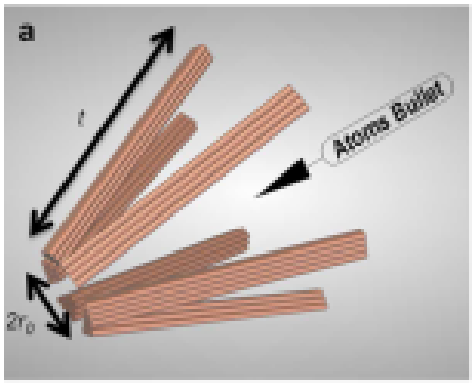

Figure 5.11: The proposed tapered magnetic hexapole lens that should address the chromatic aberrations due to the atoms' velocity spread. The figure was taken from reference [84].

5.4 Conclusion

We have presented some concepts from charged particle and atom optics that we have used in our experiments. Electric fields can be used both for deflecting as well as for focusing electron beams. We have used a pair of rectangular bars with a potential difference between them to deflect ions from our atomic beams and built an electron gun to induce damage on our samples. Moreover, in all of our experiments we had used an electron analyzer and needed to understand the basic principles behind its operation. Lastly, we had used permanent magnet hexapole lens in conjunction with transverse laser cooling to create a bright atomic beam.

Chapter 6

Experiment

6.1 Introduction

Our experimental apparatus consisted of two ultra-high vacuum chambers ($\sim 5 \cdot 10^{-9}\ Torr$) connected with each other: the *source chamber* and the *sample chamber*. The main experimental apparatus is shown in fig. 6.1. The

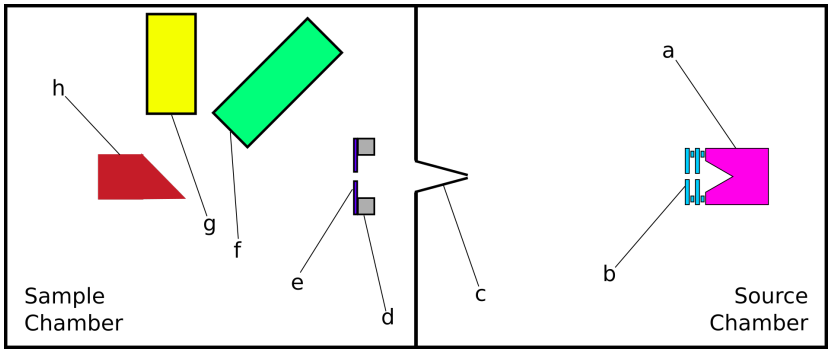

Figure 6.1: A cartoon version of the experimental apparatus not to scale. The parts are: a) nozzle, b) high-voltage discharge, c) skimmer, d) ion-removal bars, e) aperture, f) electron analyzer, g) electron gun, and h) sample holder.

source chamber is the chamber where we excite the helium atoms to the $^3S_1$ state. The atoms are introduced in the source chamber via a pulsed nozzle that is connected with an external helium cylinder. Once introduced to the chamber, the helium atoms pass through two hollow cylindrical electrodes that have $-950\,\mathrm{V}$ voltage difference and that creates an electric discharge which subse-

quently excites and ionizes portion of the helium beam. What separates the two chambers is a *skimmer* that selects the centermost part of the atomic beam creating a beam with low divergence. Following the skimmer and entering the sample chamber, where all the measurements and experiments take place, there is a pair of electrodes with 219 V voltage difference with the goal of deflecting ions from the atomic beam. Attached to these electrodes is a ceramic piece with an aperture in its center acting as a further beam collimator guaranteeing that only the sample will be probed by the metastable atoms. In the main part of the chamber, there is the sample attached on a floating sample holder, an electron gun used as the damaging agent in the experiments, and the electron analyzer used to detect the emitted electrons and filter them based on their kinetic energy. In this chapter, we will provide more detail about the functionality of each component and provide some performance data for some of them. In order to determine the performance of each component, we recorded the induced current on our sample as a result of ultraviolet photons and metastable atom impact. The signal was amplified with a transimpedance amplifier and integrated with respect to the time duration. In this manner, we were able to deduce the number of ultraviolet photons and metastable atoms in a given configuration. For all the measurements, we assumed an electron emission efficiency of unity, which is definitely not true, but allows us to establish a lower bound to the actual number of ultraviolet photons and metastable atoms. The recorded signals had similar forms as the one depicted in fig. 6.2 and the parameters had the values listed in table 6.1

apart from the parameter we were varying for each scenario.

Parameter	**Default value**
Gas pressure	400 psi
Nozzle pulse duration	32.5 µs
Discharge delay	60 µs
Discharge duration	30 µs
Discharge voltage	−950 V
Ion removal voltage	219 V
Sample bias	−50 V

Table 6.1: Default operation parameters.

6.2 Source chamber

6.2.1 Nozzle

Both of our chambers operate in ultra high vacuum ($\sim 5 \cdot 10^{-9}\ Torr$) and we interface an external helium cylinder with an in-vacuum pulsed supersonic nozzle. The gas line connecting the cylinder with the nozzle is connected with $\frac{1}{16}\ in$ stainless steel tubing pressurized at $\sim 400\ psi$. Our nozzle is a pulsed supersonic Even-Lavie nozzle able to output pulses with duration 10 µs to 35 µs and a circular opening of 200 µm diameter. For our experiments, the nozzle operated using a 32.5 µs pulse. According to [87] the Even-Lavie nozzle is able to produce pulses with density of $\sim 1 \times 10^{23}\,\mathrm{atoms/m^3}$ moving at $\sim 1760\,\mathrm{m\,s^{-1}}$. The speed is based on the formula $v_{rms} = \sqrt{\frac{5k_bT}{m}}$ [88], [89] describing a supersonic beam of a monoatomic gas, where k_b is Boltzmann's constant, T is the temperature, and m is the mass of the atom used. The dependence of metastable atom density to the line pressure is shown in fig. 6.3.

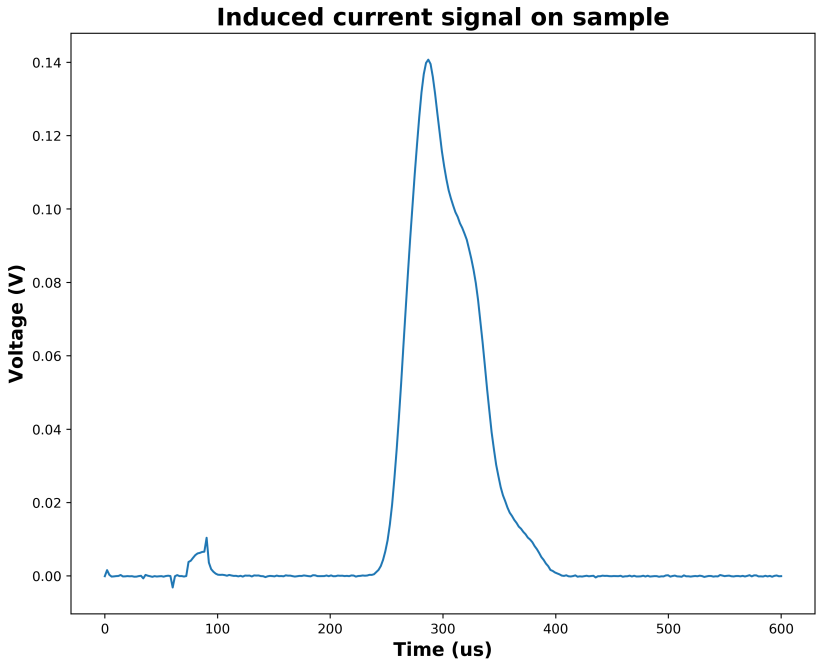

Figure 6.2: The amplified induced current signal on the sample due to ultraviolet photon and metastable atom impact. The parameter values used are those listed in table 6.1.

The dependence of metastable atom density to the nozzle pulse duration is shown in fig. 6.4.

6.2.2 Discharge

Attached to the nozzle, $\sim$3 mm in front of it, there is a pair stainless cylindrical electrodes with $\sim$3 mm separation and $\sim$2 mm apertures. The electrode closest to the nozzle is connected to a high voltage pulsed source and is electrically insulated from the nozzle. The second plate which is further away

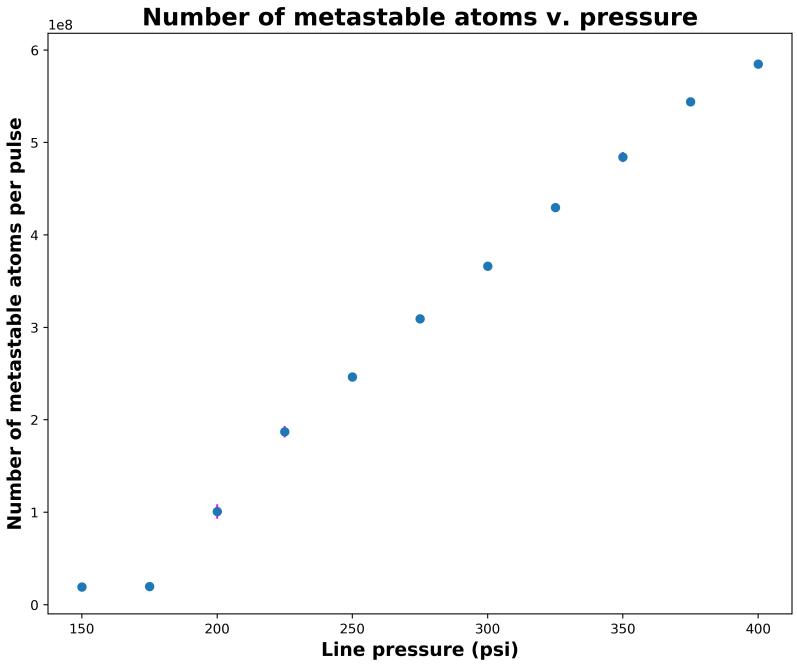

Figure 6.3: Experimental results showing atom number per shot as a function of the gas pressure supplying the helium gas to the nozzle.

from the nozzle is in electrical contact with the nozzle and therefore connected to ground since the nozzle is electrically grounded. By applying a high voltage between these plates we are able to excite portion of our atoms to the $^3S_1$ metastable state. Unfortunately, using a discharge also creates helium ions as well as other metastable states such as $^1S_0$ with $\sim$20 ms lifetime which is enough time for atoms in $^1S_0$ to reach and interact with the sample. The high voltage source can provide negative pulses $\leq$50 µs at a voltage down to -3 kV. This allows us to pulse the discharge electrodes at different times, for different

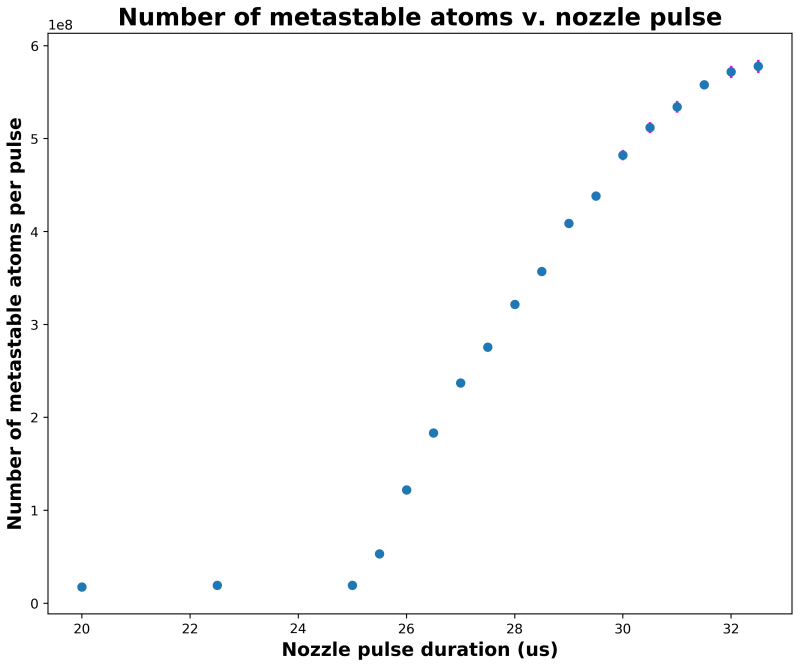

Figure 6.4: Experimental results showing atom number per shot as a function of nozzle pulse duration.

discharge pulse duration, and at different voltages. Typically the discharge electrodes operate with a 60 µs delay, for a duration of 30 µs, and at −950 V. The high voltage source uses a *Behlke HTS 31-GSM* push-pull high voltage switch with −3 kV maximum operating voltage. The push-pull switch can create pulses from 80 ns to infinity, and outputs 500 mA continuous current and 30 A peak current for pulses <10 µs with 1% duty cycle. The push-pull high voltage switch is connected with a 0.1 µFcapacitor bank rated for 3 kV. Our pulses are short enough that the voltage remains steady during the discharge

thus we can deliver up to 30 A. Based on the existing literature [25], [90], [91] a discharge apparatus can excite $10^{-7} - 10^{-4}$ of the atomic population into the desired metastable state. The produce beam is shown in fig. 6.5. The dependence of atom number versus nozzle delay are shown in fig. 6.6. The dependence of atom number versus nozzle pulse duration are shown in fig. 6.7. The dependence of atom number versus discharge voltage are shown in fig. 6.8.

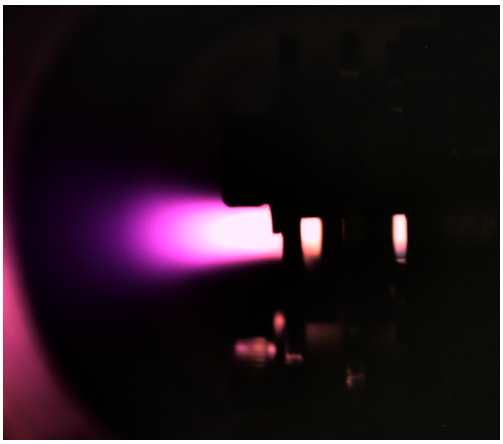

Figure 6.5: A picture of the discharge taking place while our nozzle is in operation.

6.2.3 Skimmer

Once the atoms leave the discharge electrodes region they travel for about 8 cm where they encounter the entrance of the skimmer. The entrance to the skimmer creates a collimated atomic beam, separating the source from the sample chamber as a consequence of differential pumping. Our skimmer was purchased from *Beam Dynamics*, it has a 3 mm orifice, and is 2.5 cm long,

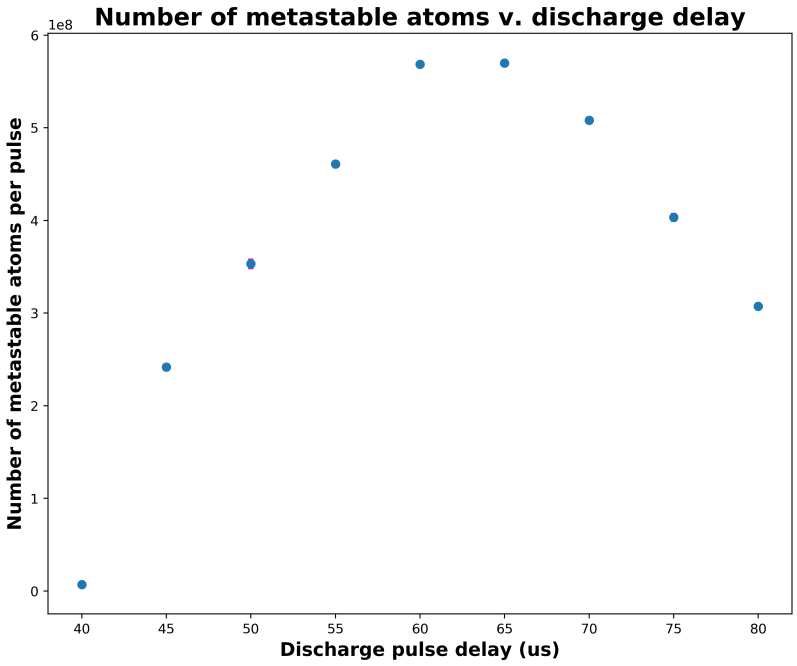

Figure 6.6: Atom number per shot as a function of time delay between the nozzle opening and the initiation of the discharge pulse.

with 25° internal angle and 30° external angle.

6.2.4 Ion removal

Following the skimmer, approximately 20 cm from the nozzle, is the ion removal apparatus that deflects ions present in the beam. The apparatus is shown in fig. 6.9. This guarantees that only metastable atoms will reach and interact with our samples. The apparatus consists of two rectangular stainless steel bars, $\frac{3}{8} \times \frac{3}{8} \times 3.5\ in$, that define a plane whose normal is the propagation

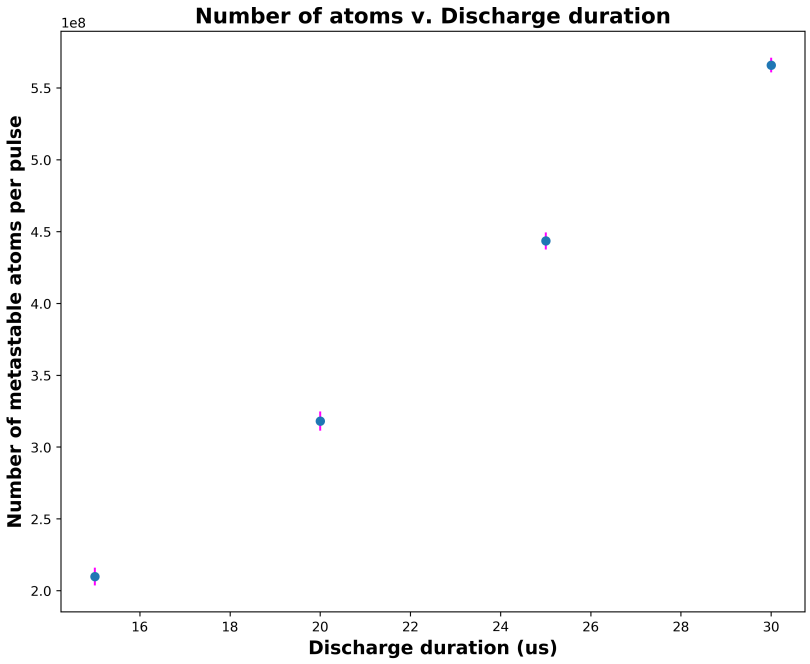

Figure 6.7: Atom number as a function of discharge pulse duration.

axis of the beam. One bar is usually biased at 219 V with respect to ground and the other bar is usually connected to a transimpedance amplifier that is subsequently connected to an oscilloscope in order to act as a diagnostic tool. For this reason, the second bar is considered as being connected with the ground. The diagnostic is shown in fig. 6.10. Attached to the two ion removal bars that are separated by 20 mm, is a ceramic square with a $\frac{3}{16}$ *in* diameter aperture which ensures that only the sample will be exposed to the atomic beam by blocking atoms with a high transverse position that can potentially interact with the other components in the experiment.

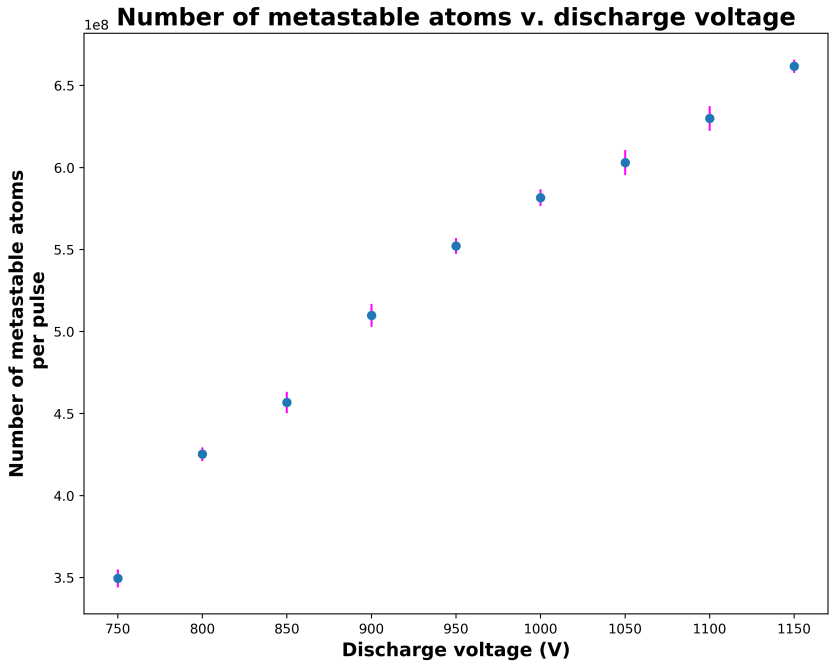

Figure 6.8: Atom number per shot as a function of discharge voltage.

6.2.5 Atomic beam characteristics

In our experiment it is pretty important to identify the various constituents present in our beam. The discharge is a pretty violent process and it creates pretty much anything one can imagine given an atom. Our atomic beam ends up having ultraviolet photons that travel almost instantaneously (speed of light, you guessed correct) to the sample, positive ions, excited states and of course neutral ground state atoms. It is worthwhile noting that part of the discharge electrodes and the other hardware used in the discharge apparatus are probably damaged during the discharge and probably seed the atomic

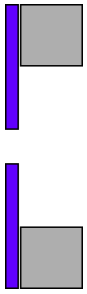

Figure 6.9: The ion removal apparatus with the ceramic aperture attached to it. One bar is at ground and the other bar is at 219 V with respect to ground. This transverse potential difference pushes ions outside of the metastable atom beam. In addition to this there is a ceramic aperture that selects portion of the beam.

beam. From what we have seen this is not a big concern in our apparatus since any other elements will exhibit a different time of flight compared to the helium atoms and should arrive much later than the helium atoms something that does not seem to be the case in our experiment. For starters, when we operate under the typical parameters (see table 6.1) we create an atomic beam with $\sim 5.8 \cdot 10^8 \frac{He^*}{pulse}$ and about $\sim 9 \cdot 10^6 \frac{UV}{pulse}$ giving us a ratio of ultraviolet photons to metastable atoms of 0.016. The results are shown in fig. 6.11. This is important because we can show that the amount of ultraviolet photons is small enough that does not damage the self-assembled monolayers during the duration of the entire experiment. Therefore any damage contributed to the ultraviolet photons is negligible. In a similar manner, we calculated the number of ions produced in each shot when the ion removal apparatus is off as demonstrated in fig. 6.12 and we have $\sim 3 \cdot 10^6 \frac{He^+}{pulse}$.

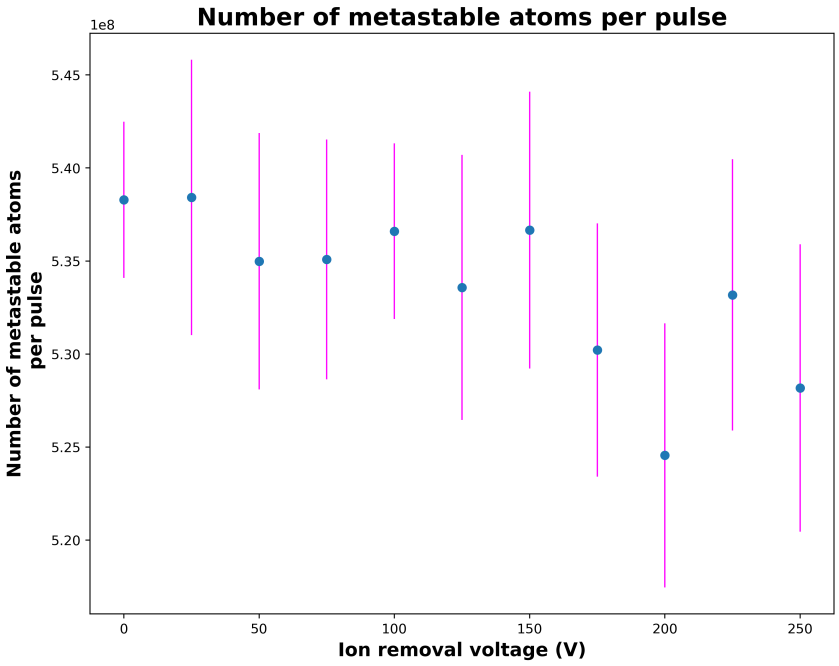

Figure 6.10: Atom number per shot as function of voltage difference between the two bars at the ion removal apparatus.

6.3 Sample chamber

The sample chamber operates at a base pressure of $2 \cdot 10^{-9}$ $Torr$ and new samples are introduced via a loading lock mechanism which separates a smaller compartment from the main chamber. This allows us to switch samples on demand without breaking vacuum every time we need to change samples.

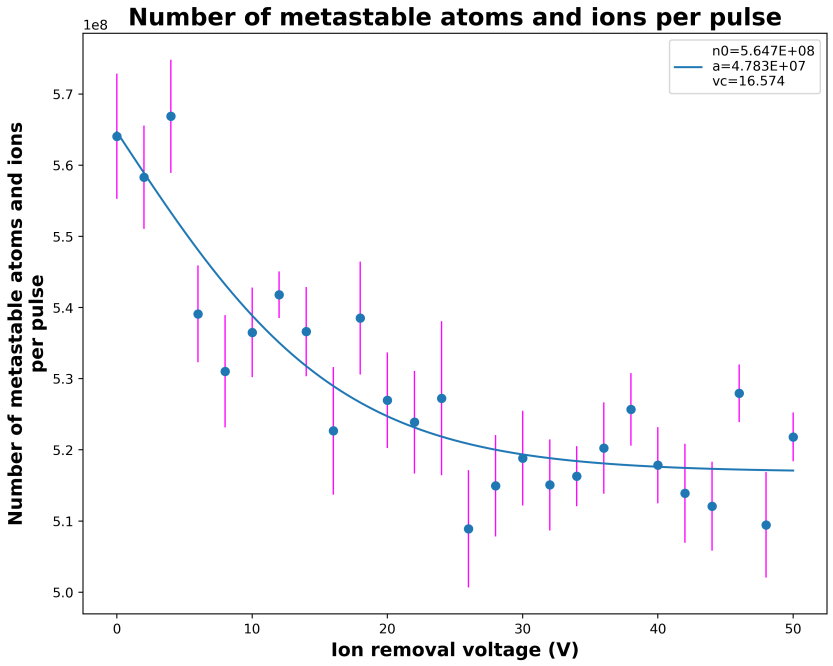

Figure 6.11: He* and ion population arriving at the sample as a function of the voltage across the ion removal bars.

6.3.1 Sample holder

Our samples are mounted on a custom made sample holder located ∼40 cm from the nozzle with a $\frac{3}{8} \times \frac{3}{8}$ *in* cross-section. The normal to the sample holder's face makes a 45° with respect to the axis of propagation of the atoms and coincides with optical axis of the electron analyzer. This choice was made due to the fact that the emitted electrons are not emitted isotropically and the majority of them are emitted normal to the surface. The sample to analyzer distance is 20 mm. Furthermore, the sample holder allows to float

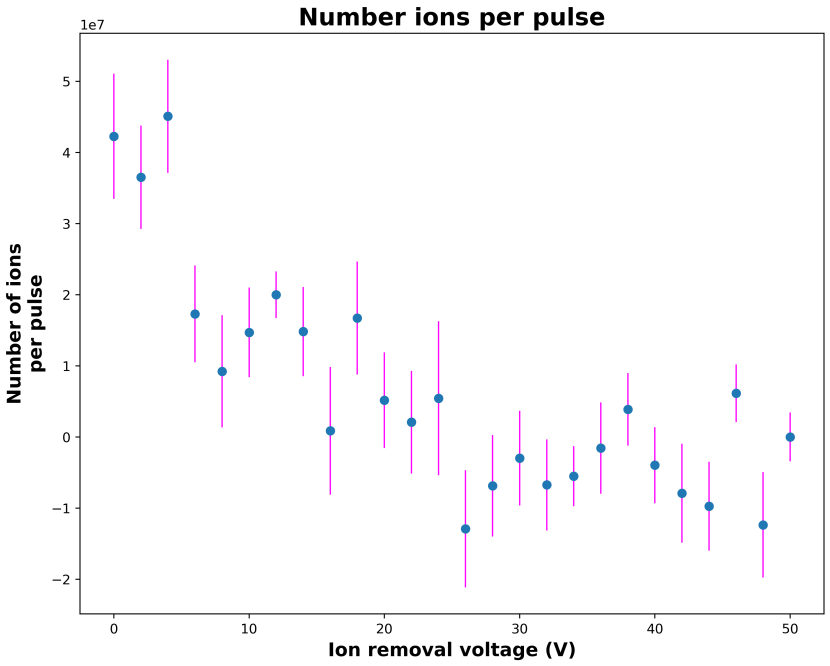

Figure 6.12: Ion population arriving at the sample as a function of the voltage across the ion removal bars.

the sample at an arbitrary voltage which is useful for guiding the emitted electrons from our sample towards the electron analyzer. Of course one might be weary that by biasing our sample we might alter the information content in our spectrum and the spectra at different bias voltages are shown in fig. 6.13. In our experiments the sample is biased at $-50\,\mathrm{V}$ and it is connected with a passive high pass filter in order to record the induced current on our sample. The induced current is a result of the electron emission due to the metastable helium atom de-excitation. The high pass filter is a passive RC filter with

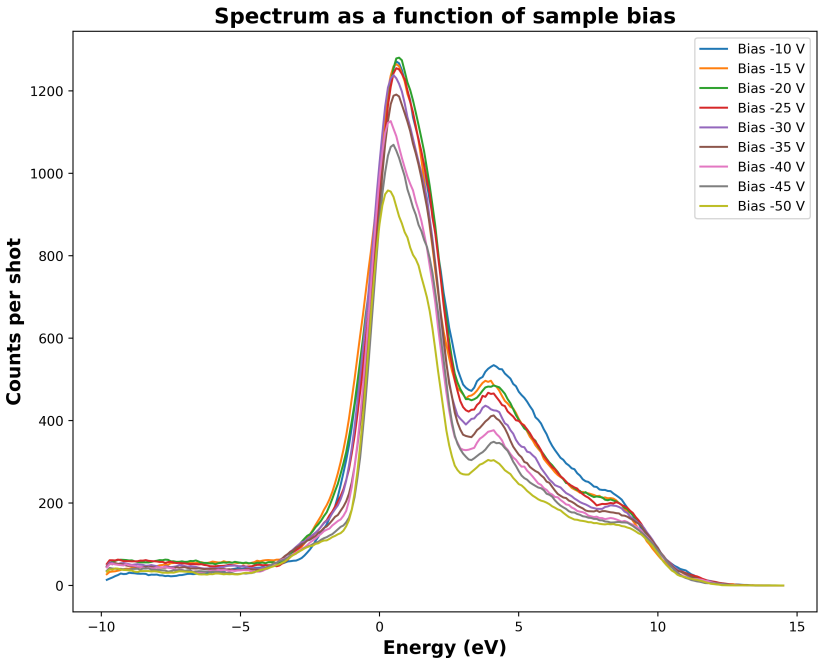

Figure 6.13: MAES spectrum of a damaged SAM as a function of the bias voltage applied to the sample. All the spectra have been shifted according to the bias voltage used in order to show how well they overlap.

$R = 1\,\mathrm{M\Omega}$ and $C = 2\,\mu\mathrm{F}$ giving us a time constant $\tau = RC = 2\,\mathrm{s}$. The output of the filter is connected to a *FEMTO DLPCA-200* transimpedance amplifier operating with a 400 kHz bandwidth and 10^5 gain.

6.3.2 Electron analyzer

The electron analyzer can be definitely worshiped as the workhorse of this experiment and at the same time it has been the bane of our existence for the last six years. In our apparatus, we used a *VSW HA 50* hemispherical

electron analyzer borrowed from professor James Erskine who is member of our physics department. It has an average hemisphere radius $R_0 = 50\,\text{mm}$ and $d = 6\,\text{mm}$ width for the entrance and exit slits. According to eq. (5.8) and using a half angle $\alpha = 4^\circ = 0.07\,\text{rad}$, the resolution for pass energy $E_p = 4.46\,\text{eV}$ (FAT50 mode) corresponds to a resolution of $0.27\,\text{eV}$. The resolution for pass energy $E_p = 9.03\,\text{eV}$ (FAT 125 mode) is $0.55\,\text{eV}$. In our experiments we scan electron kinetic energies between $40\,\text{eV}$ to $65\,\text{eV}$. This is due to the fact that we bias our sample at $-50\,\text{V}$ and the helium $^3S_1$ metastable atom has $19.8\,\text{eV}$ available energy. Based on our experiments, we do not see any electrons present at kinetic energies $>63\,\text{eV}$ which is the reason why we chose $65\,\text{eV}$ as our endpoint. The fig. 6.14 shows a cross-section of the electron analyzer and the fig. 6.15 shows a SIMION simulation. The operation parameters of the

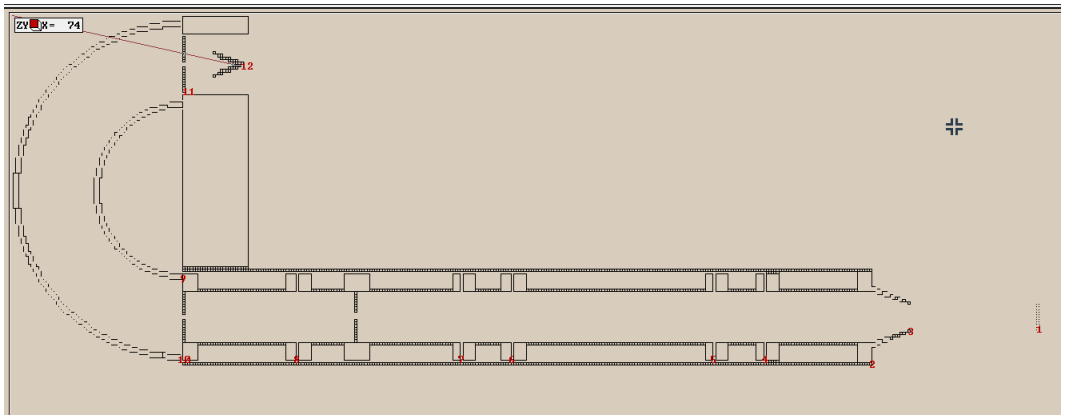

Figure 6.14: Cross section of the electron analyzer showing the electron optics that image and decelerate electrons at the entrance slit. Also shown are the two hemispheres and the channel electron multiplier detector. A grounded μ-metal shield surrounds the entire electron analyzer.

electron analyzer are presented in table 6.2 and table 6.3.

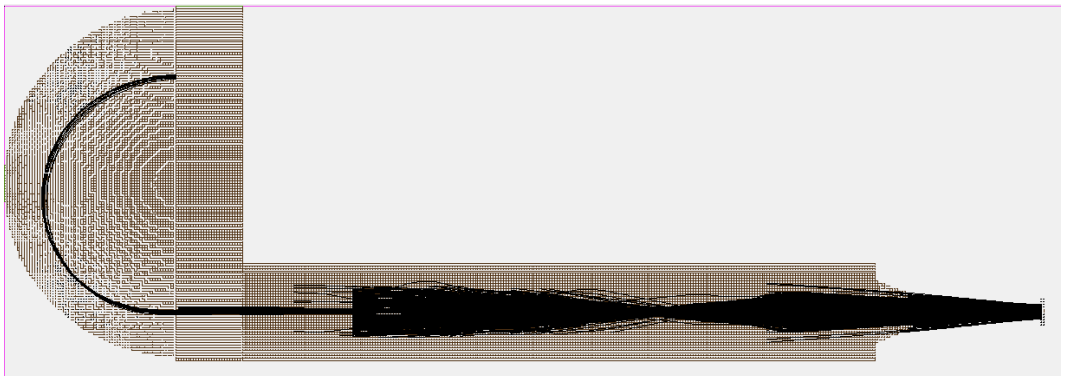

Figure 6.15: Simulating electron trajectories through the electron analyzer using SIMION an electron trajectories software. The electrons are moving with kinetic energy 10 eV with divergence 4°.

6.3.3 Channel electron multiplier

We use a channel electron multiplier (CEM) in order to detect the electrons that make it through the hemispheres . The main idea behind a CEM is to amplify the electrons entering the detector in order for typical electronic equipment to record the signal. The detector is divided in three regions: entrance, exit, and collector. The entrance is biased at a moderately low voltage ∼50 V in order to attract electrons to enter the detector, the exit is biased at a high voltage 2500 V in order to encourage electrons to come down the channel. As the electrons travel through the channel they collide with the walls, creating secondary electrons. Lastly, the collector is biased either at the same voltage as the exit or at slightly higher voltage in order to encourage electrons to reach the collector which is the stage connected with our electronic equipment. In our experiment, the collector is connected with a high pass filter filtering out the collector's high voltage ∼2500 V and only the

Lens element	5 eV	10 eV	15 eV	20 eV
1	30	48	59	70
2	20	15	10	5
3	46	41	36	31
4	20	15	10	5
Slit	-1	-6	-11	-16
Inner hemisphere	3	-2	-7	-12
Outer hemisphere	-3	-8	-13	-18
CEM front bias	54	49	44	39

Table 6.2: Voltages on each electron optical element operating in FAT 50 mode.

Lens element	5 eV	10 eV	15 eV	20 eV
1	30	49	68	87
2	43	38	33	28
3	93	88	83	78
4	43	38	33	28
Slit	4	-1	-6	-11
Inner hemisphere	12	7	2	-3
Outer hemisphere	0	-5	-10	-15
CEM front bias	54	49	44	39

Table 6.3: Voltages on each electron optical element operating in FAT 125 mode.

pulses (AC signal) due to the detected electrons is measured by our electronics. More specifically, we are using an RC high pass filter with $R = 1\,\mathrm{M}\Omega$ and $C = 1\,\mathrm{nF}$. Furthermore, our channel electron multiplier is a *Detech 206-10* with $\sim 10^8$ gain, $\sim$5 ns rise time, and $\sim$20 ns pulse width. The typical pulse from a channel electron multiplier going through the high pass filter and recorded on an oscilloscope terminated with a $50\,\Omega$ terminator is shown in fig. 6.16.

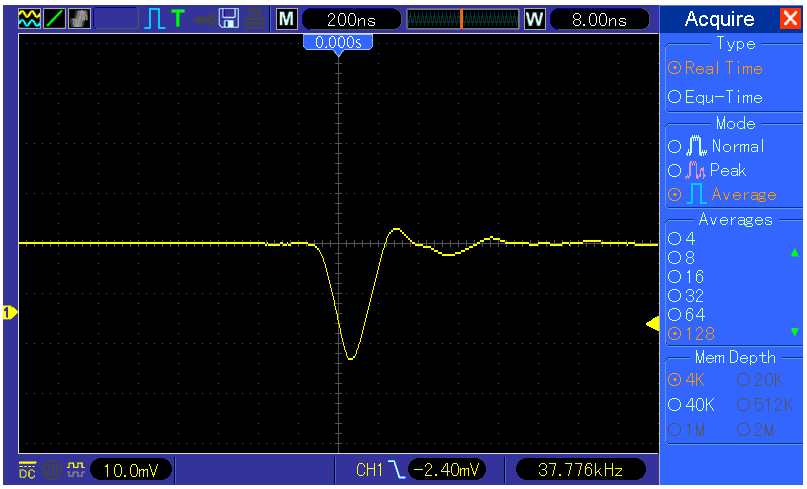

Figure 6.16: The signal output of our channel electron multiplier with potential difference 2400 V.

6.3.4 Electron gun

Our electron gun is designed and built in-house (see fig. 6.17) with the sole purpose of providing a tunable source of electrons in the low kinetic range (<450 eV). It consists of two square electrodes with a rectangular slit. The source of electrons is a tungsten filament that emits electrons as a result of thermionic emission. Typically we operate the tungsten filament at ∼2 A and we deliver ∼1.9 mC in thirty minutes exposures. As can be seen in fig. 6.18 the emission current reduces as the Wehnelt voltage became more negative. In fig. 6.19 we can see that the emission current was not affected by the bias voltage applied on the sample. The number of electrons reaching the sample increased as the Wehnelt electrode became more negative up until a certain point. As can be seen in fig. 6.20 the induced current at the sample kept increasing in magnitude until the Wehnelt electrode was biased at −40 V where

Figure 6.17: Our electron gun

the induced current magnitude dropped drastically. In fig. 6.21 we can clearly see that as the sample bias voltage increased the magnitude of the induced current on the sample also increased. Using the electron analyzer we were able to characterize the electron beam coming out of our electron gun. In fig. 6.22 we can see the kinetic energy profile of the beam. The beam's intensity as a function of the Wehnelt electrode voltage is shown in fig. 6.23. The most probable energy of the beam is shown in fig. 6.24. The standard deviation

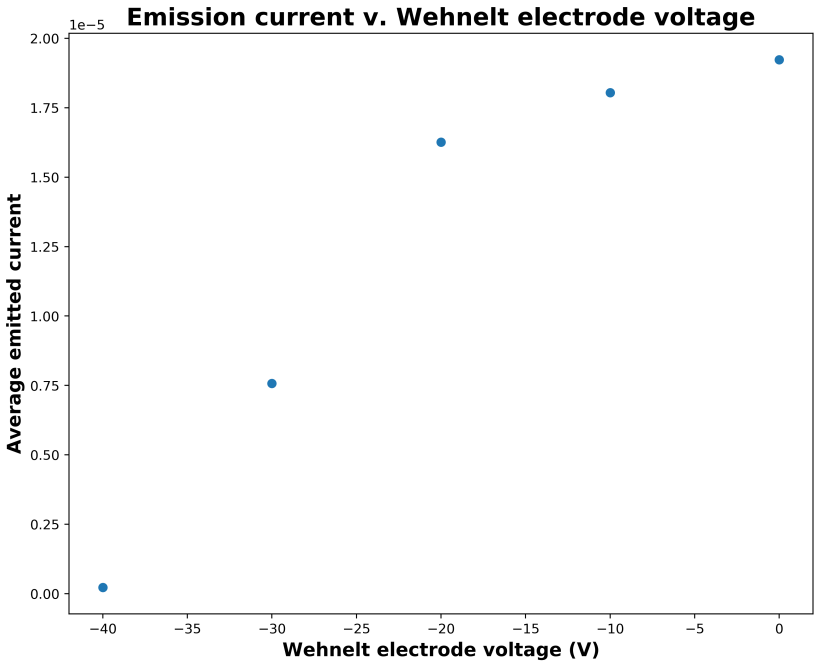

Figure 6.18: Emission current from our filament as a function of Wehnelt electrode voltage.

of the beam's energy distribution is shown in fig. 6.25. We determined the amount of electrons hitting our sample by connecting our sample with a picoammeter (Keithley 6485) that measured the current flowing through the sample during the electron exposure. We assume that almost all of the electrons in the primary beam emitted from the electron gun are going through the sample and measured by the picoammeter. Of course there is a portion of the primary electrons that gets reflected from the surface but that is an extremely small portion. We also have secondary electron emission which does

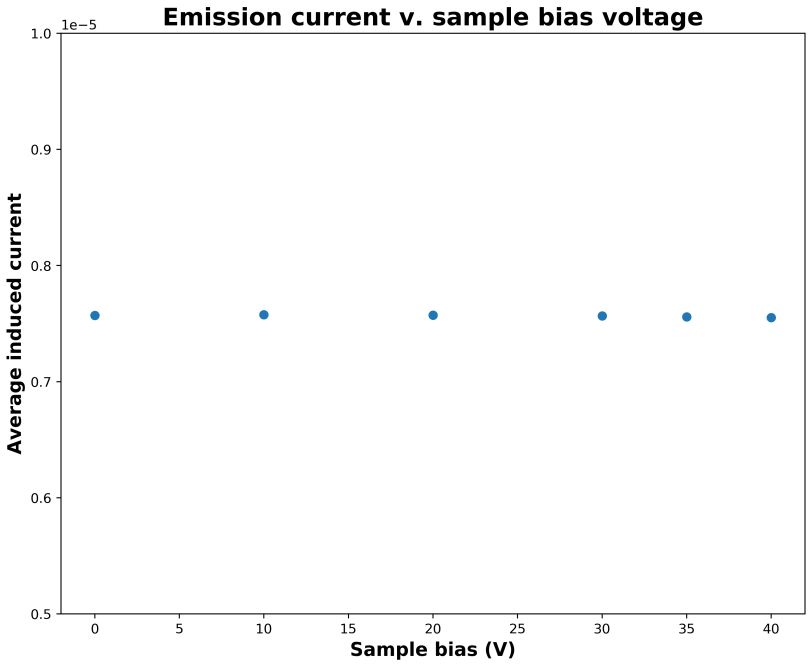

Figure 6.19: Emission current from our filament as a function of sample bias voltage.

complicate things, but we also assume that this emission has a negligible effect on the picoammeter measurements. In this manner, we are able to determine the electron dose delivered on our sample for a given amount of time.

6.3.5 Data acquisition

All of the data are acquired by interfacing our hardware with a computer that runs a data acquisition module written in *LabVIEW*. This module allows one to control various aspects of the experiment, but definitely leaves a

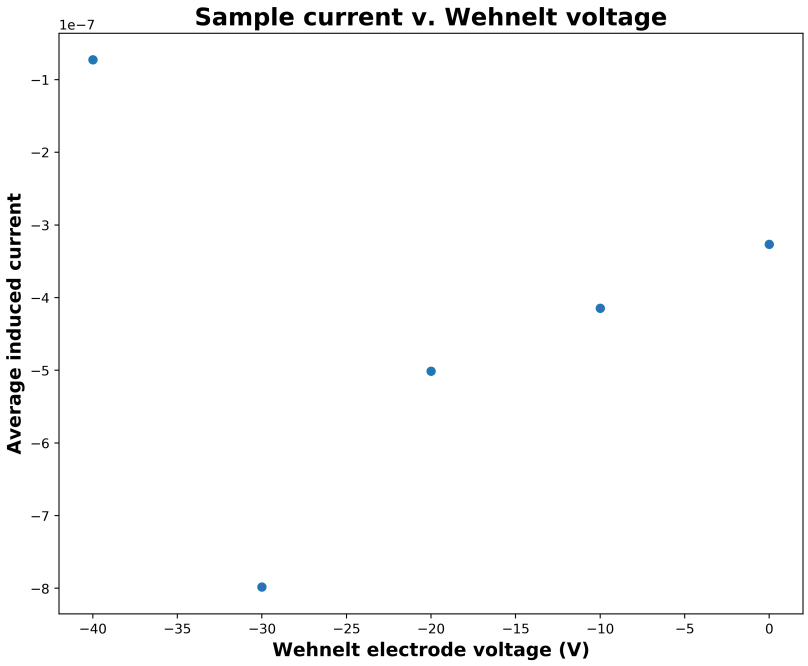

Figure 6.20: Induced current on the sample due to the electron gun beam as a function of the Wehnelt electrode voltage.

significant portion to the user. Using the time of flight difference, it discriminates any detected electrons due to ultraviolet photons and records only the electrons emitted as a result of metastable atom impact. We take advantage of the fact that once we initiate the discharge, the ultraviolet photons arrive almost instantaneously whereas the metastable atoms require $\sim$200 µs to reach the sample.

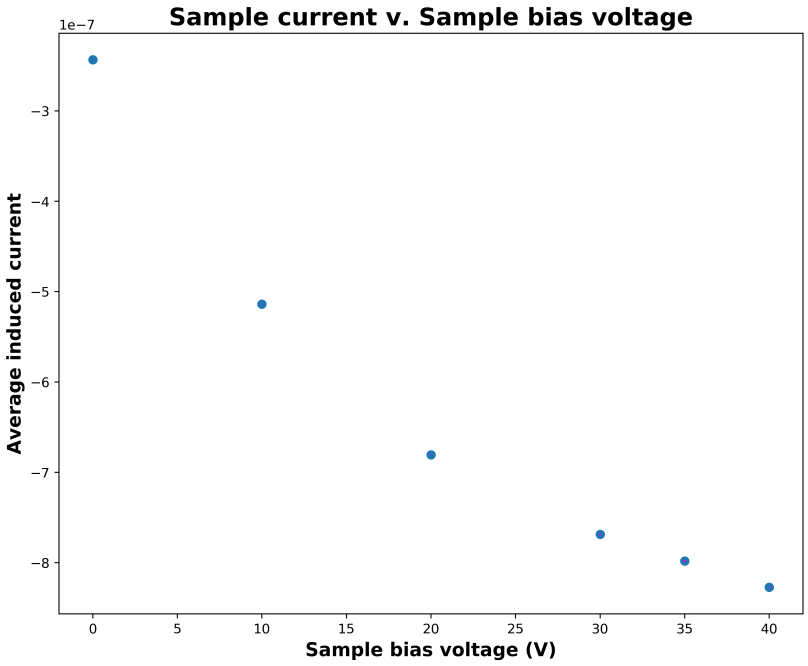

Figure 6.21: Induced current on the sample due to the electron gun beam as a function of the sample bias voltage.

6.4 Making the samples

Lastly, a crucial aspect of our experiment is making the samples, a task carried out in professor Lauren Webb's lab located in the Faulk Nanoscience and Technology building here at the University of Texas. The samples were grew on gold-coated silicon wafer which we had previously cut in wafer in squares 10 mm by 10 mm. After we had cut the samples we rinsed them very well with acetone and ultra high purity water. Before a sample making session, in order to remove any organic contaminants from our surfaces, we immersed

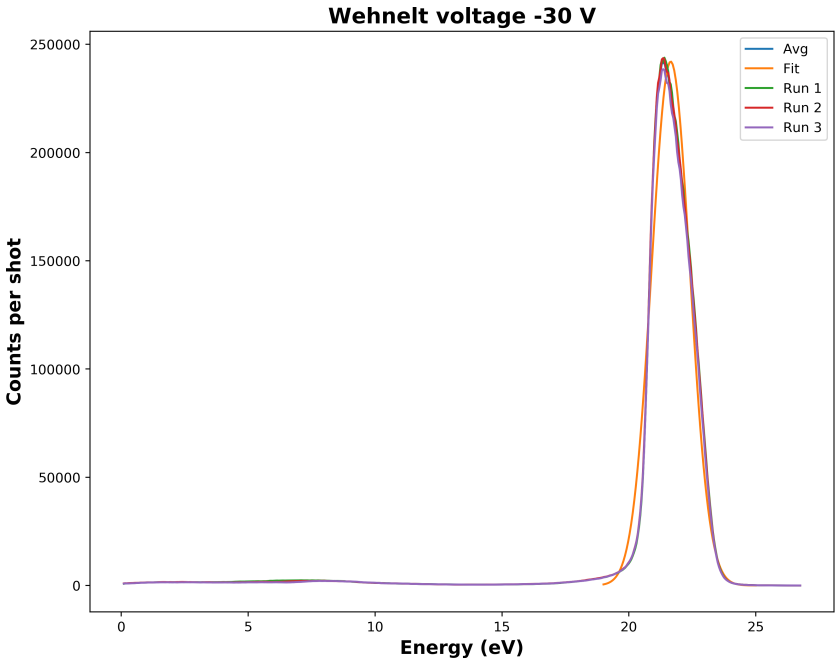

Figure 6.22: The electron gun's beam kinetic energy spectrum. The spectrum was recorded using the electron analyzer set at the FAT 50 mode.

the gold-coated squares in a piranha solution ($25\%\ H_2O_2, 75\%\ H_2SO_4$) for one minute. After the piranha treatment we rinsed the squares for $\sim$10 s in ultra high pure water and after that rinsed it again for another $\sim$10 s in 200 proof ethanol. Following this process, we had to anneal the substrate by exposing it to a hydrogen flame in order to make sure that the surface is as flat and smooth as possible. The hydrogen flame was created using a really low pressure $\sim$ 10 *psi* hydrogen flow from a cylinder. We would then heat up a certain area of the fireproof counter for about a minute, long enough

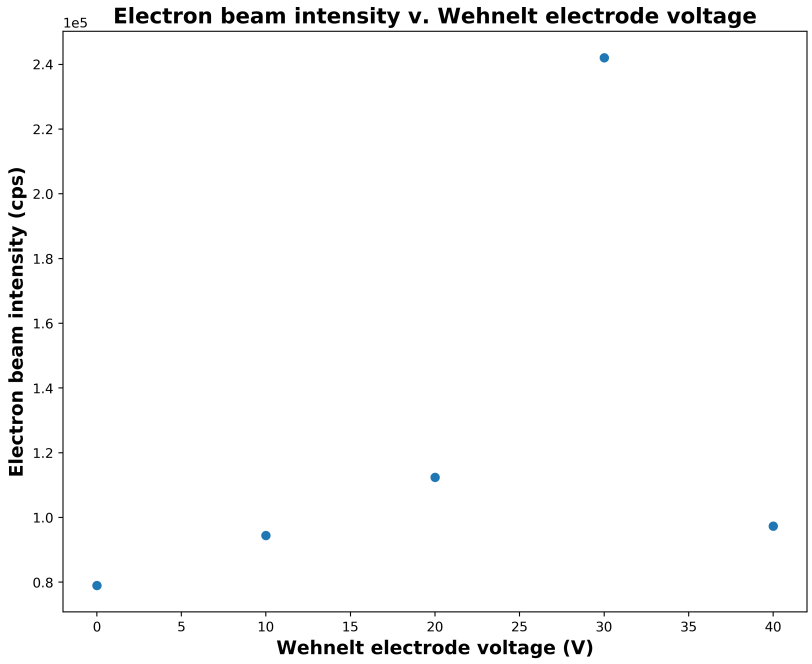

Figure 6.23: The electron beam's intensity as a function of the voltage applied on the Wehnelt electrode.

to make sure that no water created from the hydrogen burning will condense on the surface. After heating the counter, we placed a glass microscope slide on top of the hot area and heat it up with the flame by moving the flame across the slide slowly but steadily without lingering too long over a certain spot. Lingering causes hot spots which will make the slide crack. Ideally it should take ∼1 s to go from an end of the slide to the next with the hydrogen flame. Once the slide was warm enough (∼30 s) we placed the squares on the slide. The annealing process consisted of ten rounds of 25 s of moving the

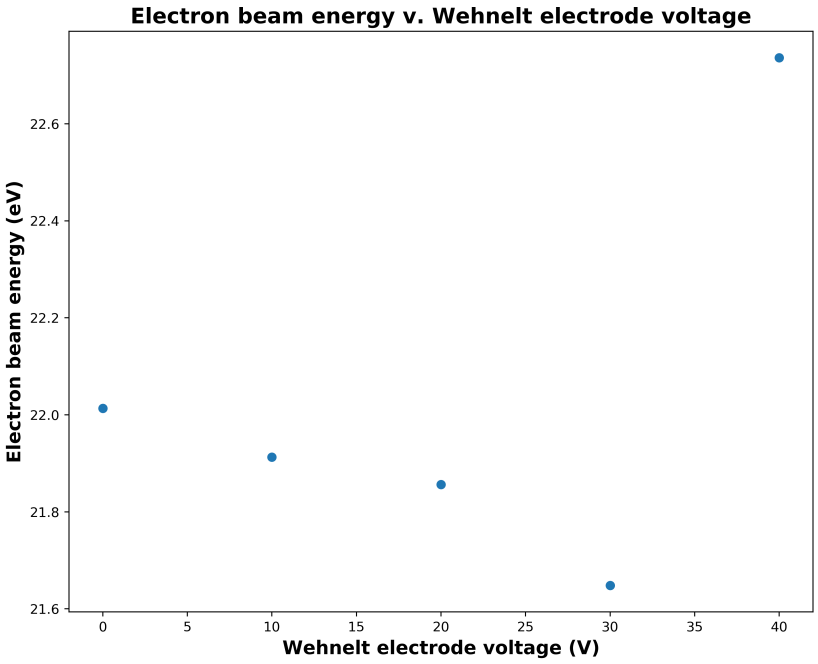

Figure 6.24: The energy of the electron beam produced by the electron gun as a function of the voltage applied on the Wehnelt electrode.

flame over the squares and 5 s of cooling down. The flame was kept about one inch away from the squares and it was tilted at 45° with respect to the normal of the squares surface. Using a shallower angle will blow the squares of the microscope slide and using a bigger angle will cause the hydrogen to reflect towards our hand holding the hydrogen nozzle causing burns. Again while the squares were exposed to the flame we had to be careful not to linger over one area too long because that could create a hot spot in the slide under and cause a crack. Once the annealing process was over we allowed the squares to cool

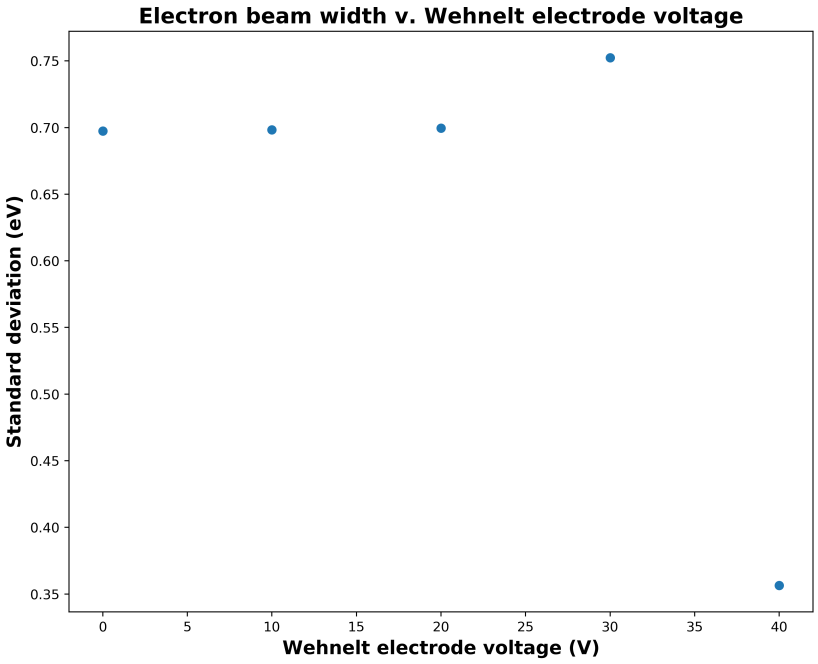

Figure 6.25: The standard deviation of the electron beam produced by the electron gun as a function of the voltage applied on the Wehnelt electrode.

down and immersed them in the organic solution which in our case was 11-bromo-1-undecanethiol and 1-dodecanethiol. In order for the self-assembled monolayers to form we had to place the immersed sample in a dark space for twenty four hours. The next day we performed Fourier transform infrared spectroscopy (FTIR) in order to determine if the monolayer has formed and how well ordered it was. The FTIR spectrum of 11-bromo-1-undecanethiol is shown in fig. 6.26 and that for 1-dodecanethiol in fig. 6.27.

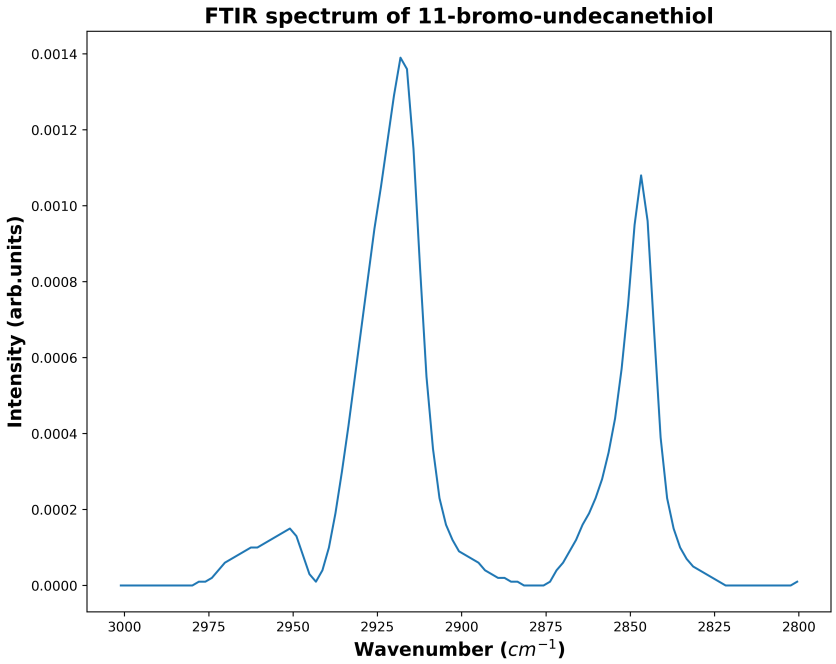

Figure 6.26: FTIR spectrum of 11-bromo-1-undecanethiol

6.4.1 Making samples on graphene

The procedure for making samples using graphene on silicon as a substrate was much easier. Since we did not want to disturb the graphene monolayer sitting on top of the silicon wafer we neither did the piranha process nor the annealing. We just took the substrate and directly immersed it in the solution and waited twenty four hours for the monolayer to form. We did not perform FTIR spectroscopy in order not to mess with our sample.

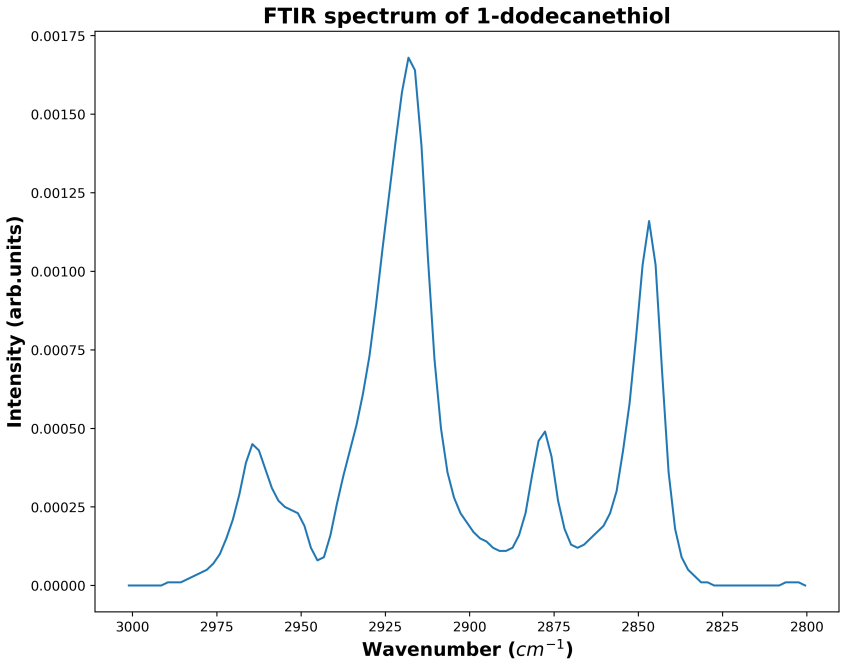

Figure 6.27: FTIR spectrum of 1-dodecanethiol

6.5 The workflow of the experiment

Our experiments with metastable atoms were divided in two segments. One segment was the data acquisition using metastable atoms determining the state of the self-assembled monolayer that we were studying. The other segment was exposing the monolayer to a beam of electrons emanating from our custom made electron gun. In our experiments we repeated these two segments back to back, with data acquisition followed by electron beam exposure in order to record a spectrum after each exposure. The goal was to see how these spectra changed over a series of exposures and which features

remained the same. For the XPS experiments, we placed the samples in the XPS chamber and exposed the samples to x-rays for 4 hours without turning the x-ray source off. The x-rays that were used to damage the sample were alsoused to probe it.

6.6 Improvements

Our apparatus is pretty robust and easy to modify. Having said that there are a couple things we could replace or modify. First and foremost, we should get a new electron analyzer that is properly calibrated and comes with proper documentation as well as technical support. Furthermore, having a commercial electron gun will be much more beneficial for our studies since we will in principle know the primary beam current and its spot size and could tune it over a bigger range of energies. A new electron gun could also be used for performing other spectroscopy techniques such as Auger electron spectroscopy which can be used for sanity check or as a complementary technique in our studies. Another important addition is to have a laser or a discharge lamp dedicated for quenching atoms in undesirable metastable states such as the helium $^1S_0$ in our case. Having a laser for polarizing our atomic beam could also prove beneficial in cases where we want to test the magnetic properties of a sample. Lastly, we should get a new sample chamber made out of μ-metal in order to minimize the magnetic field inside our chamber.

Chapter 7

Results

7.1 Introduction

We performed experiments using both metastable atom electron spectroscopy (MAES) as well as x-ray photoelectron spectroscopy (XPS). In the MAES set of experiments we determined the damage induced on a self-assembled monolayer when exposed to a low energy (65 eV) electron beam for thirty minutes (total charge ∼1.9 mC). These results have conclusively shown that MAES is non-destructive and can be employed to monitor damage induced on organic materials. In the XPS set of experiments, we exposed the self-assembled monolayer to x-rays (1486.6 eV) for four hours and took spectra in regular time intervals. In each spectrum, we identified a peak corresponding to the element of interest and tracked it over time (peak location, amplitude, and full width half maximum). In this way, we deduced the effect of the x-ray exposure. For each set, we tried two different substrates: gold-coated silicon, and monolayer graphene on silicon. The main idea was to see if the electron mobility of the substrate had any noticeable effect in preventing damage from taking place.

7.2 MAES: 11-bromo-1-undecanethiol on gold

As can be seen in figs. 7.1 and 7.2 the electron spectra recorded using MAES do change after each electron exposure. More specifically, a peak

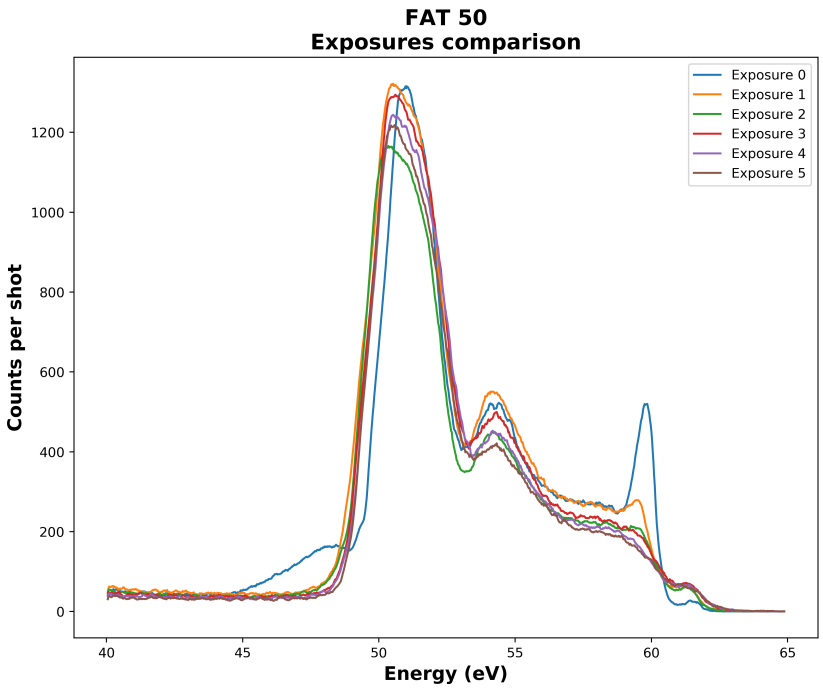

Figure 7.1: The MAES spectra recorded with 4.46 eV pass energy of 11-bromo-1-undecanethiol on gold after a series of 5 exposures.

$\sim$59.5 eV gets shorter with each electron exposure and a shoulder appears at $\sim$61.5 eV after the first electron exposure and maintains the same amplitude over the rest of exposures. We can also see a reduction of the peak located $\sim$54.5 eV after each electron exposure and a complete elimination of a shoulder present $\sim$49 eV that was present before any electron exposure took place. As

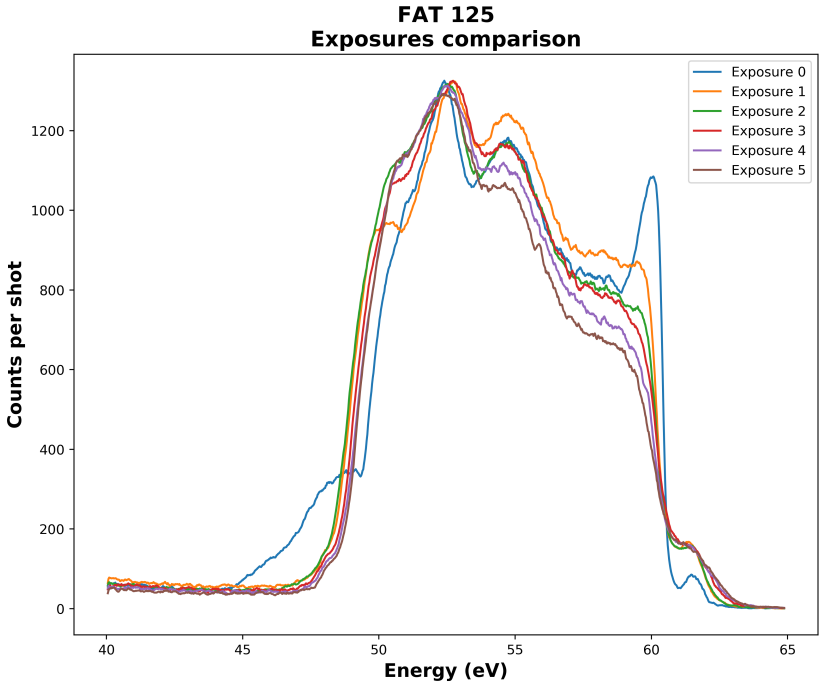

Figure 7.2: The MAES spectra recorded with 9.03 eV pass energy of 11-bromo-1-undecanethiol on gold after a series of 5 exposures.

a reminder all the spectra were taken by biasing the sample at $-50\,\mathrm{V}$ as described in section 6.3.1. The spectra shown in fig. 7.1 were taken at 0.27 eV resolution whereas those shown in fig. 7.2 were taken at 0.55 eV resolution (see section 6.3.2).

7.3 MAES: 1-dodecanethiol on gold

As a reference and sanity check, we performed the same experiment as the one described in section 7.2 using 1-dodecanethiol instead of 11-bromo-1-

undecanethiol. For this experiment, the sample was biased at −10 V instead of −50 V which qualitatively does not influence the spectra in a significant way. Essentially all the features are shifted by the bias voltage applied on the sample. As can be seen in figs. 7.3 and 7.4 there is no sharp peak present ∼19.5 eV which corresponds to ∼59.5 eV had we biased the sample at −50 V instead of −10 V. This is encouraging since we can tell the differences between

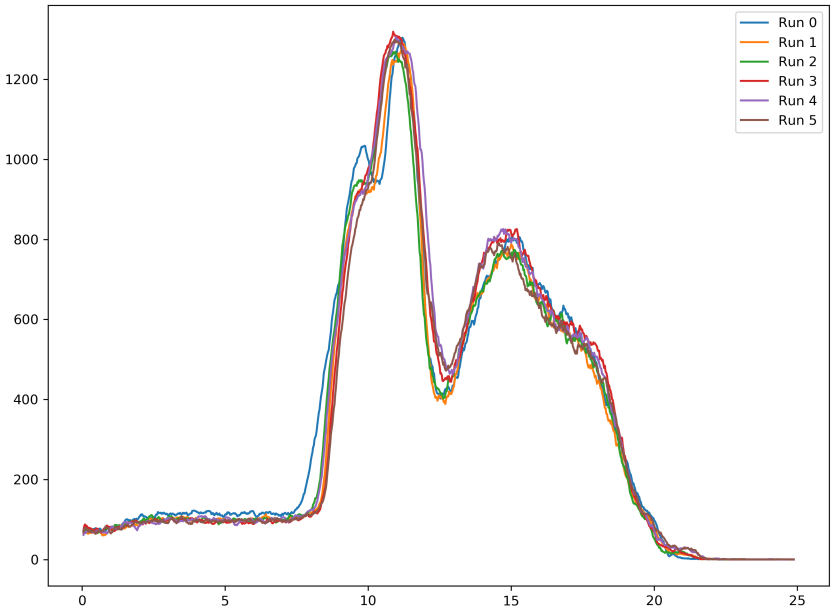

Figure 7.3: The MAES spectra recorded with 4.46 eV pass energy of 1-dodecanethiol on gold after a series of 5 exposures.

two molecules with the same head group and backbone chain length but with a different terminal group. The main distinct features of figs. 7.3 and 7.4 are the

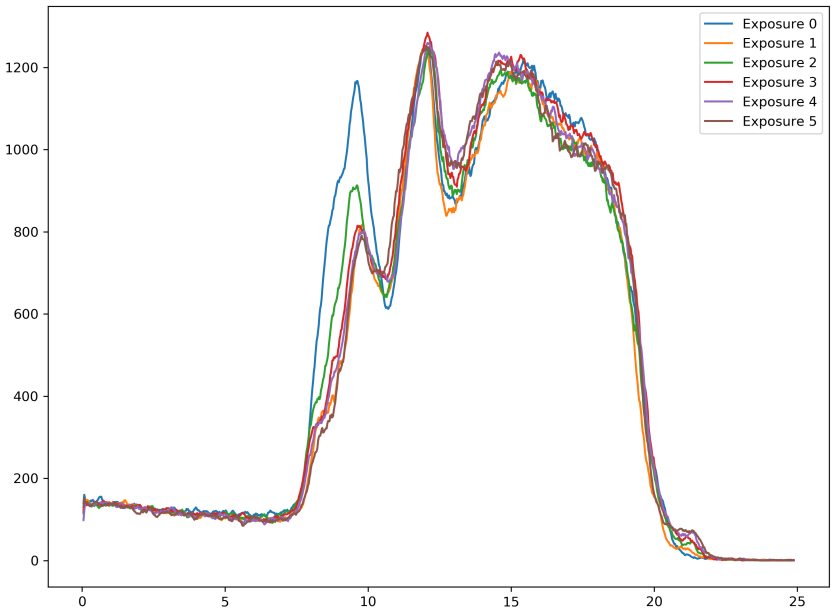

Figure 7.4: The MAES spectra recorded with 9.03 eV pass energy of 1-dodecanethiol on gold after a series of 5 exposures.

peak at ∼10 eV which gets shorter and the shoulder that develops at ∼21.5 eV after each electron exposure.

7.4 MAES: 11-bromo-1-undecanethiol on graphene

In figs. 7.5 and 7.6 we show the electron spectra for a graphene substrate. In these figures, the peak at ∼59.5 eV, which was prominent in figs. 7.1 and 7.2, has significantly less amplitude and bigger width. This is an indication of the thiol molecules laying flat on the graphene surface as it

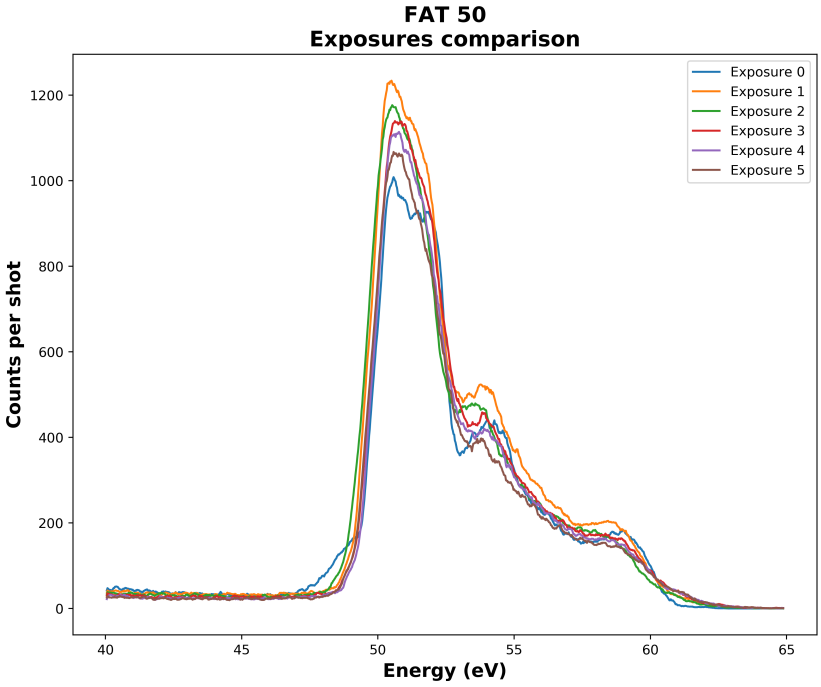

Figure 7.5: The MAES spectra recorded with 4.46 eV pass energy of 11-bromo-1-undecanethiol on graphene after a series of 5 exposures.

was observed in [52]. As it was mentioned before, the sharp peak, which was absent in the 1-dodecanethiol spectrum, it can be attributed to the bromine terminal group. Since alkanethiolates self-assemble on gold standing up, the metastable atoms interact mostly with the terminal bromine group. This is not the case when the alkanethiol molecules are laying flat since the metastable atoms can see and interact with the rest of the alkanethiol molecule. During the electron exposures, the MAES spectra did show changes indicating that the thiol molecule was damaged as well.

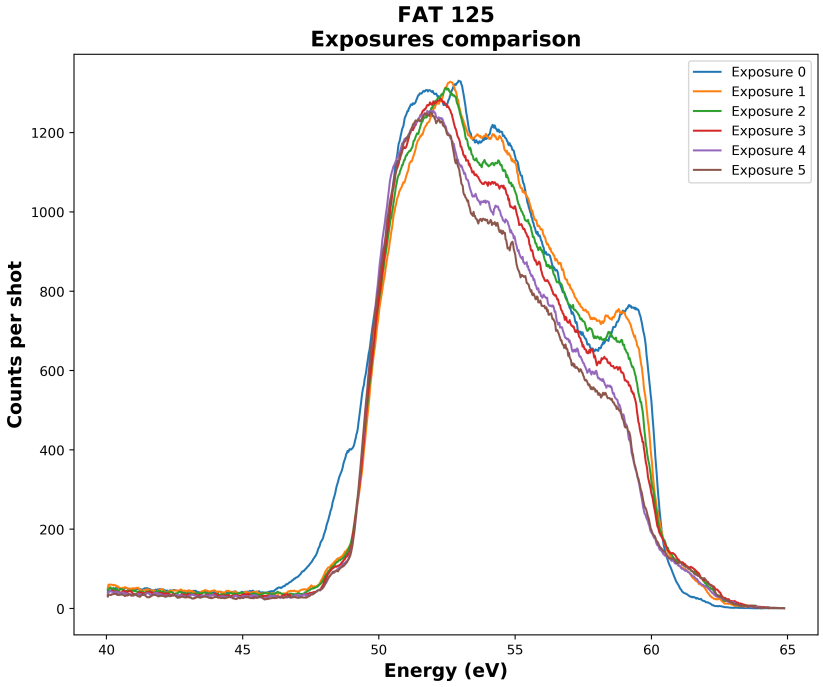

Figure 7.6: The MAES spectra recorded with 9.03 eV pass energy of 11-bromo-1-undecanethiol on graphene after a series of 5 exposures.

7.5 XPS: 11-bromo-1-undecanethiol on gold

For our XPS experiments with 11-bromo-1-undecanethiol on gold, we recorded a range of binding energies that encompassed the bromine $3p_{\frac{3}{2}}$ ($\sim$183 eV) and $3p_{\frac{1}{2}}$ ($\sim$190 eV) peaks. Even though the $3d_{\frac{5}{2}}$ and $3d_{\frac{3}{2}}$ are the prominent bromine peaks located at $\sim$70 eV, we could not easily resolve them probably due to the prevalence of the $4f$ gold peak located at $\sim$85 eV. The samples were exposed to a continuous stream of x-rays for 4 hours and recorded data in regular intervals. The spectra were analyzed using CasaXPS and fit with

two Lorentzian peaks one for $3p_{\frac{3}{2}}$ and one for $3p_{\frac{1}{2}}$. The latter peak's area was constrained to be $\frac{1}{2}$ of the former's peak and we constrained both peaks to have the same full-width-half-maximum. We used U2-Tougaard for the background signal which is a built-in function in the CasaXPS software. We performed the experiment twice the first time on 02 December 2019 and the second time on 06 January 2020. The first and last spectra with the fit are shown in fig. 7.7 for the December session and in fig. 7.8 for the January session. We can clearly see in all those figures a significant reduction to the two peaks intensities over time which is an indication of bromine leaving the sample. The figure of merit for our experiment were the peaks amplitudes which are proportional to the ratio of the area to the full-width-half-maximum. This is the quantity plotted in figs. 7.9 and 7.10 for the December session and in figs. 7.11 and 7.12 for the January session. For each dataset we used two different fitting models based on exponential decay. The first model used the function $y = y_0 e^{-\frac{x}{\tau}}$ and the second model used the function $y = y_0 e^{-\frac{x}{\tau}} + c$. The two models give us significantly different answers and we need to dig a bit further to decide which one provides a physical picture.

7.6 XPS: 11-bromo-1-undecanethiol on graphene

For our XPS experiments with 11-bromo-1-undecanethiol on graphene, we recorded a range of binding energies that encompassed the bromine $3d_{\frac{5}{2}}$ and $3d_{\frac{3}{2}}$ located at $\sim$70 eV. We did not use the $3p$ peaks, as we did in the gold dataset, due to the low signal to noise ratio. Like in section 7.5 the samples

were exposed to a continuous stream of x-rays for 4 hours and recorded data in regular intervals. The spectra were analyzed using CasaXPS and fit with two Lorentzian peaks one for $3d_{\frac{5}{2}}$ and one for $3d_{\frac{3}{2}}$. The latter peak's area was constrained to be $\frac{2}{3}$ of the former's peak and we constrained both peaks to have the same full-width-half-maximum. We used U2-Tougaard for the background signal which is a built-in function in the CasaXPS software. We performed the experiment twice the first time on 07 January 2020 and the second time on 21 February 2020. The first and last spectra with the fit are shown in fig. 7.13 for the January session and in fig. 7.14 for the February session. In both figures, there is a second peak present at $\sim$75 eV which we believe is due to copper used in the manufacturing of the graphene monolayer. We can clearly see in both figures a significant reduction to the bromine peak intensity over which indicates that portion of the bromine left the sample. The ratio of the area to the full-width-half-maximum for the January session is shown in figs. 7.15 and 7.16 and for February in figures figs. 7.17 and 7.18. We used the same fiiting models as in section 7.5 in order to make a comparison between the gold and the graphene data.

7.7 Comparison between gold and graphene substrate

Based on both MAES and XPS the thiolate bromine molecules do exhibit damage on both gold and graphene substrates. Using MAES we could not determine if the damage was more severe on gold in comparison with graphene and that could be due to the general low count rate. When we used

Var.	Gold 1	Gold 2	Graphene 1	Graphene 2
y_0	604.833 ± 12.946	1324.982 ± 12.693	92.092 ± 1.641	60.201 ± 1.907
τ	40.170 ± 2.940	27.533 ± 0.657	232.222 ± 67.876	55.633 ± 7.648

Table 7.1: Variable values for the $y = y_0 e^{-\frac{x}{\tau}}$ model for each data set.

XPS, the signal to noise ratio was also pretty low and that could be due to small amount of bromine atoms present on the surface. The signal to noise ratio can be improved by using longer acquisition times which will reduce the number of data points and will inevitably include damage effects occurring during the data acquisition. It is clear that we need to repeat the experiments for both gold and graphene using longer data acquisition times and monitoring other elements specifically carbon and sulfur in order to see the effect on those elements as well. Lastly, the values derived for each dataset for the first fitting model are presented in table 7.1 and for the second model are presented in table 7.2. The uncertainties for all datasets and both models are pretty high which do not allow us to make any concrete conclusions. This can be due to low signal to noise ratio preventing us from getting robust data and/or the fact we used a two-peak model for fitting the data in CasaXPS software. A different approach might be to increase the number of peaks used but given the data quality we doubt that will make any improvement.

Var.	Gold 1	Gold 2	Graphene1	Graphene 2
y_0	329.536 ± 38.103	1063.944 ± 59.260	15.827 ± 2.747	27.108 ± 2.156
τ	13.155 ± 3.912	18.381 ± 2.1225	2.991 ± 1.016	4.699 ± 0.827
c	302.897 ± 44.592	288.504 ± 66.687	85.171 ± 0.846	43.132 ± 0.984

Table 7.2: Variable values for the $y = y_0 e^{-\frac{x}{\tau}} + c$ model for each data set.

7.8 Conclusion

In this chapter we investigated the damage induced on self-assembled monolayers due to electron and x-ray impact. We first presented the main results of probing 11-bromo-1-undecanethiol monolayer set on gold. We probed it with MAES and found consistently how electrons damage the monolayers. We repeated the experiment with 1-dodecanethiol and saw that the spectra did not match that of 11-bromo-undecanethiol which was expected. We further exposed the samples to electrons and observed the degradation. Furthermore, we repeated the initial experiment with 11-bromo-1-undecanetiol on graphene instead of gold. The spectra before the electron exposure did look different than in the case of a gold substrate. The reason behind that is due to the fact that the self-assembled monolayers are flat instead of standing up. Similarly with before, the self-assembled monolayer degraded upon exposure to electrons. Following these experiments we exposed 11-bromo-1-undecanethiol on gold and on graphene to x-rays. The results show that in both cases the samples do get damaged, but further experiments are needed. In the future, we should trace the changes in the sulfur and the carbon peaks as well.

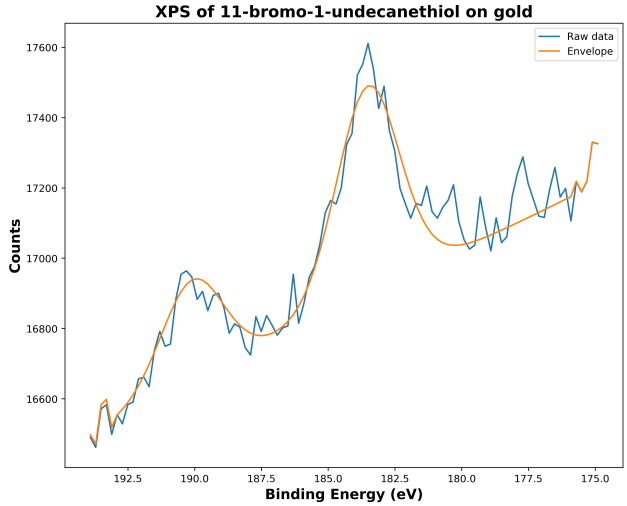

(a) First XPS spectrum

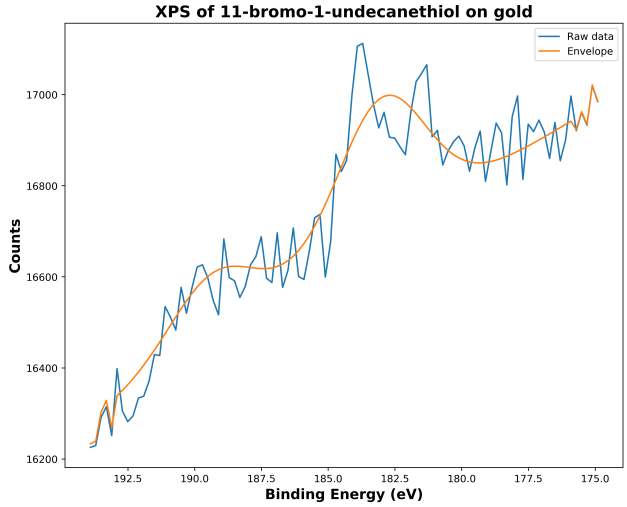

(b) Last XPS spectrum

Figure 7.7: First and last XPS spectra of 02 December 2019 run.

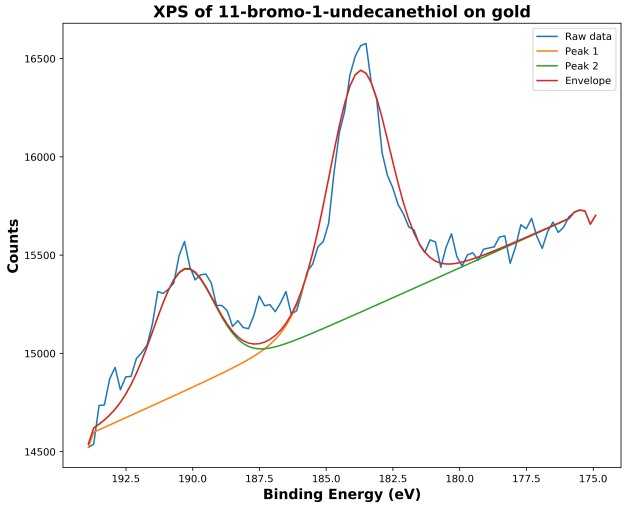

(a) First XPS spectrum

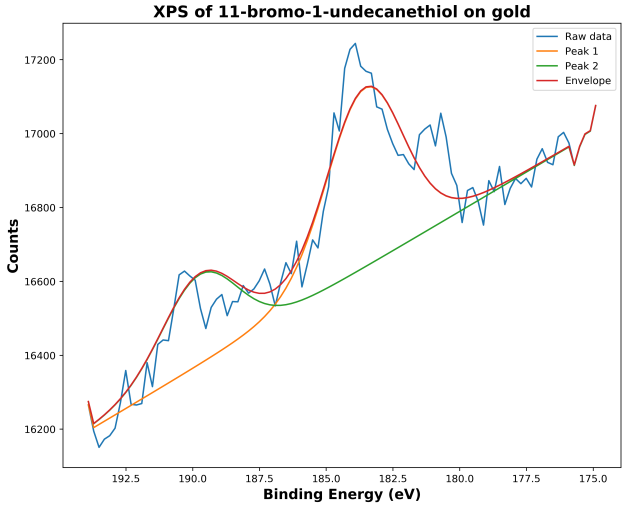

(b) Last XPS spectrum

Figure 7.8: First and last XPS spectra of 06 January 2020 run.

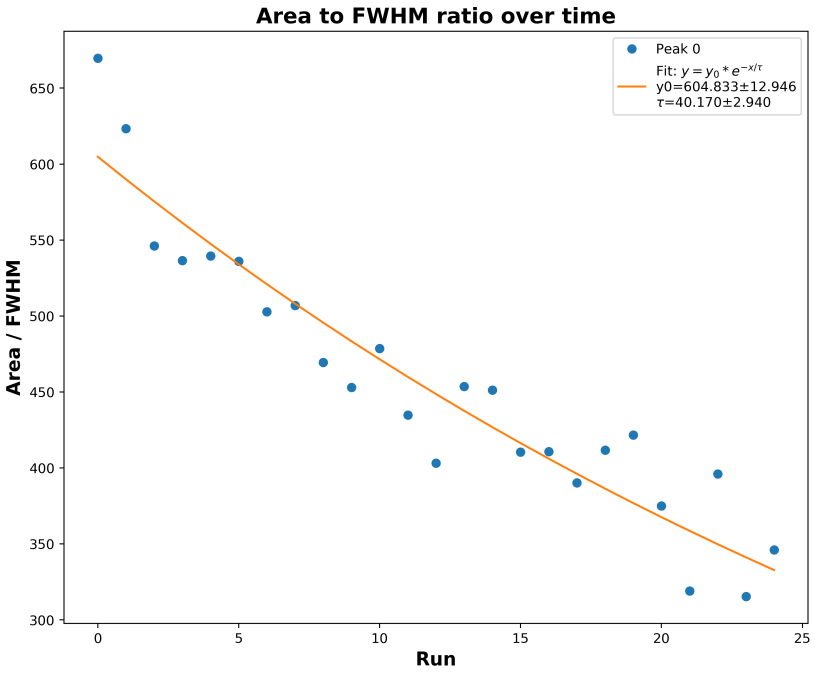

Figure 7.9: Fit using exponential decay with the form $y = y_0 e^{\frac{-x}{\tau}}$. Data were taken on 02 December 2019.

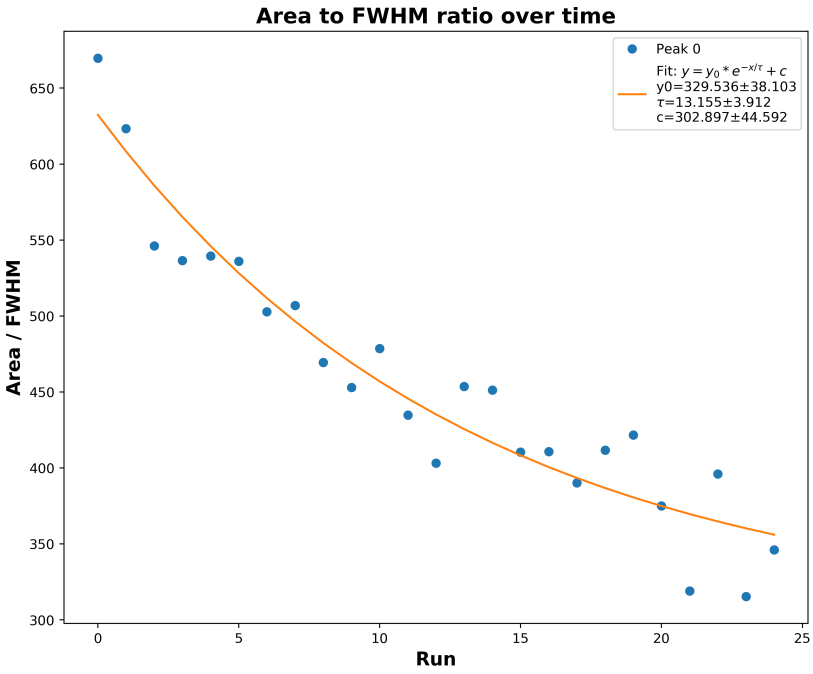

Figure 7.10: Fit using exponential decay with the form $y = y_0 e^{\frac{-x}{\tau}} + c$. Data were taken on 02 December 2019.

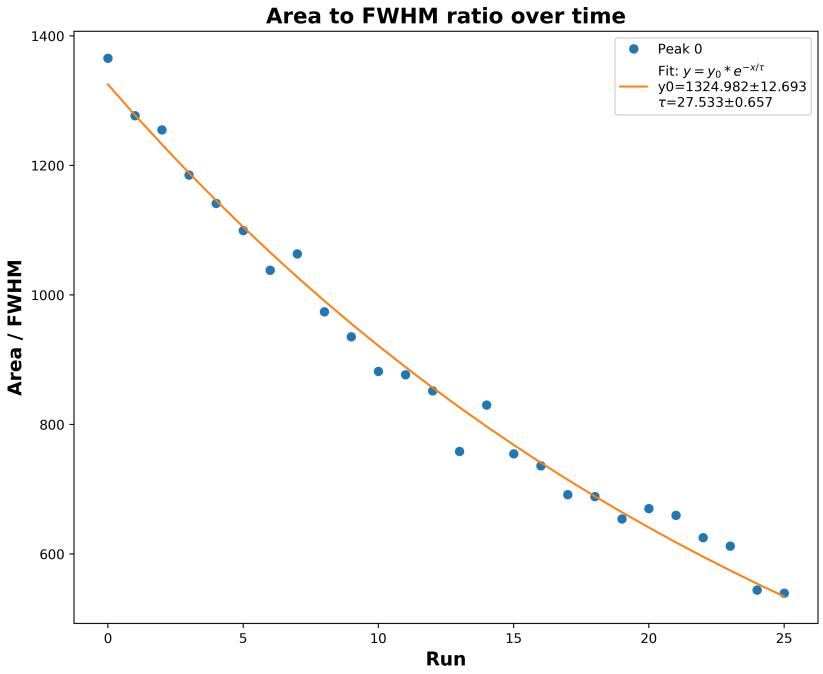

Figure 7.11: Fit using exponential decay with the form $y = y_0 e^{\frac{-x}{\tau}}$. Data were taken on 06 January 2020.

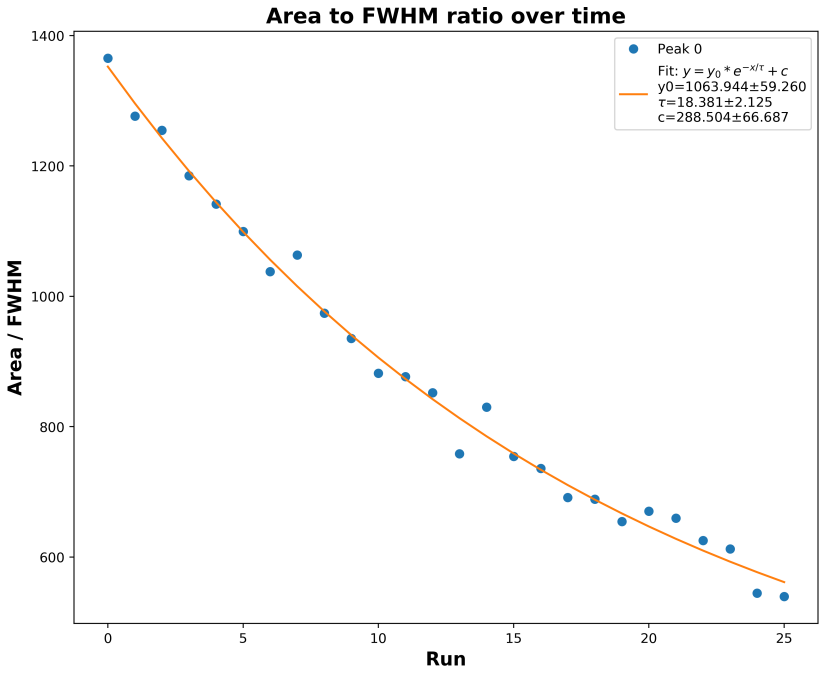

Figure 7.12: Fit using exponential decay with the form $y = y_0 e^{\frac{-x}{\tau}} + c$. Data were taken on 06 January 2020.

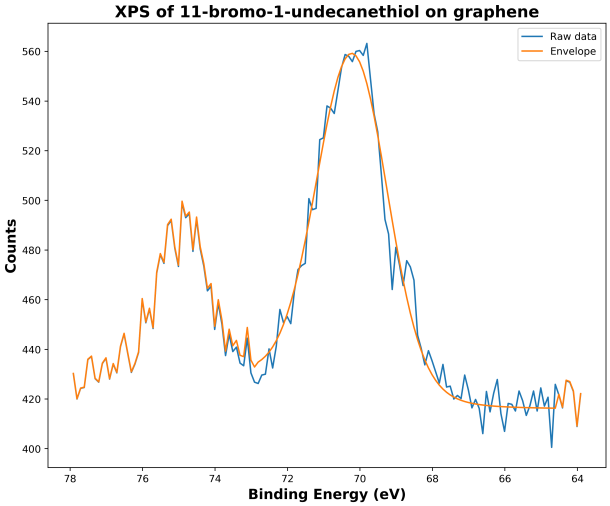

(a) First XPS spectrum

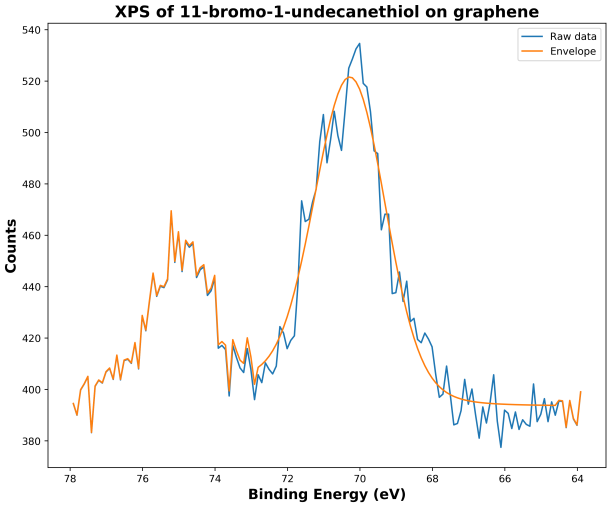

(b) Last XPS spectrum

Figure 7.13: First and last XPS spectra of 07 January 2020 run.

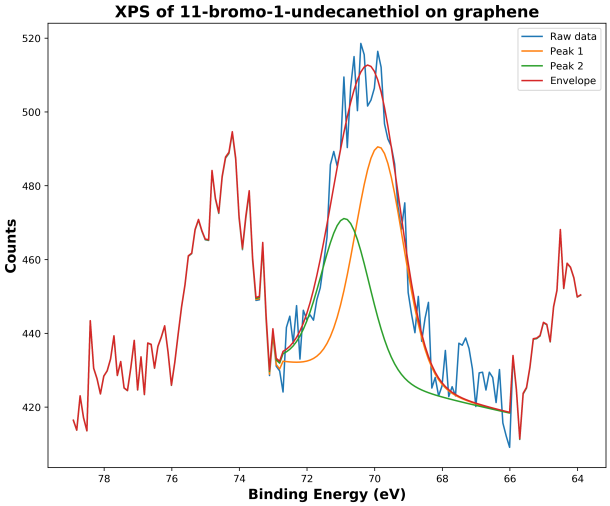

(a) First XPS spectrum

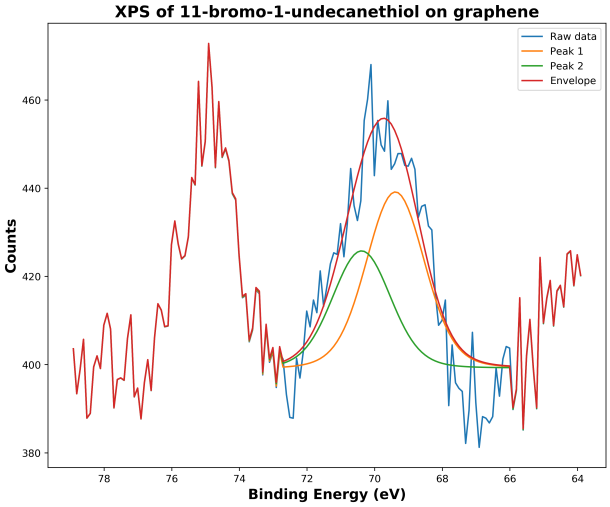

(b) Last XPS spectrum

Figure 7.14: First and last XPS spectra of 21 February 2020 run.

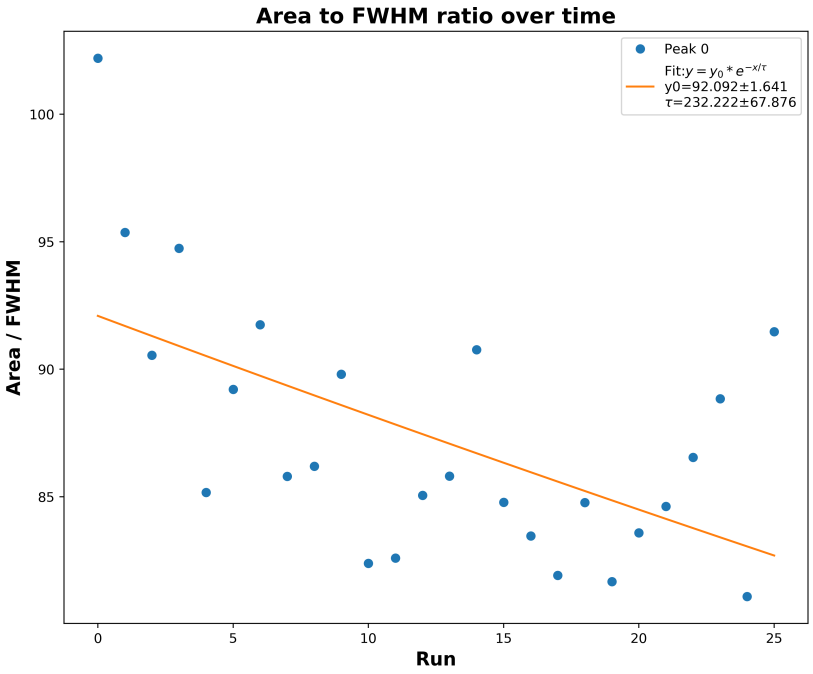

Figure 7.15: Fit using exponential decay with the form $y = y_0 e^{\frac{-x}{\tau}}$. Data were taken on 06 January 2020.

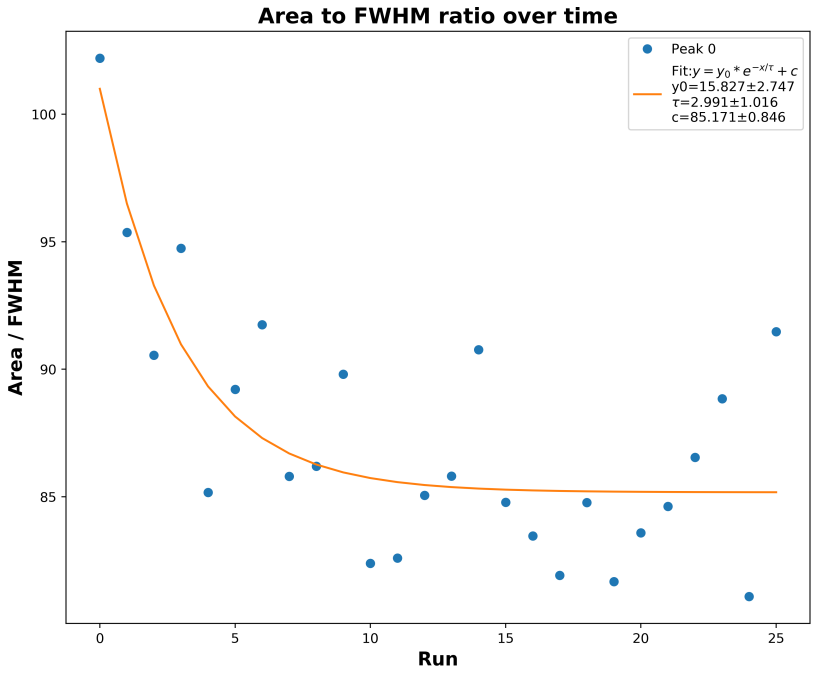

Figure 7.16: Fit using exponential decay with the form $y = y_0 e^{\frac{-x}{\tau}} + c$. Data were taken on 07 January 2020.

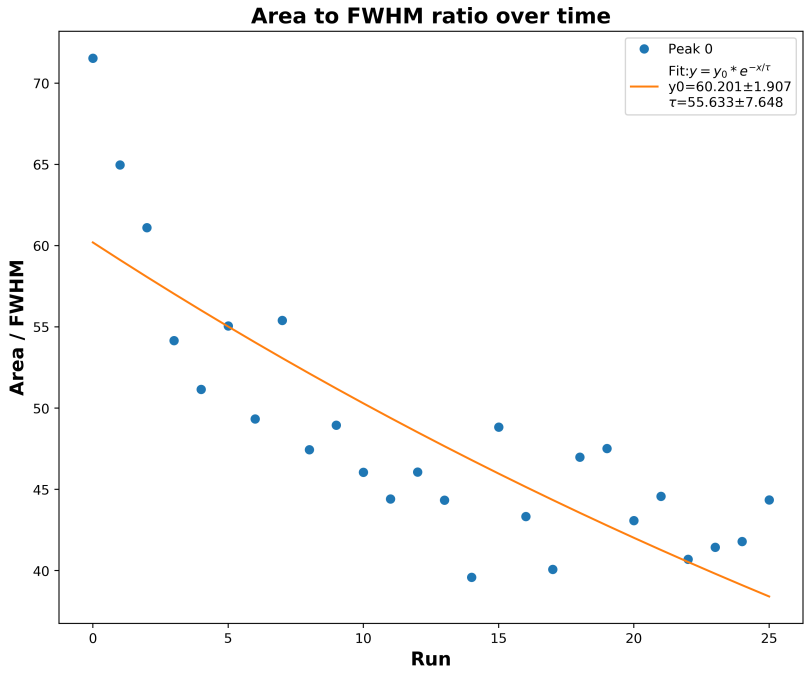

Figure 7.17: Fit using exponential decay with the form $y = y_0 e^{\frac{-x}{\tau}}$. Data were taken on 21 February 2020.

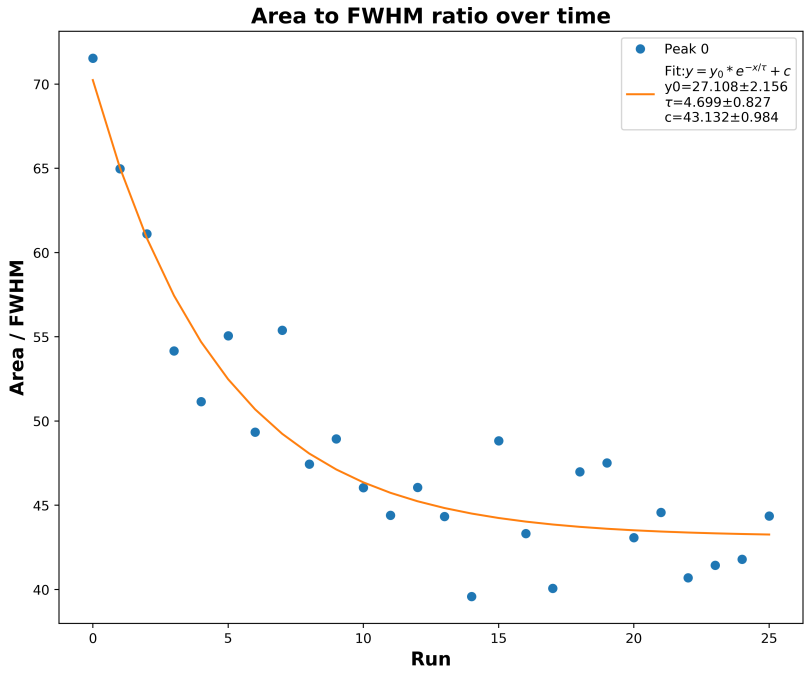

Figure 7.18: Fit using exponential decay with the form $y = y_0 e^{\frac{-x}{\tau}} + c$. Data were taken on 21 February 2020.

Chapter 8

Conclusion

We started this endeavor with a lot of ideas in mind and we have managed to explore a subset of our initial goals leaving the rest for future researchers. Projects always strive to do more things that they can actually achieve in the limited amount of time, but that is not to be thought as something discouraging. On the contrary, a plethora of ideas allows for many alternatives when your existing direction is not working out and can keep you constantly motivated because there is always something to be done. Even though, we initially embarked with the goal of building an atom microscope with nanometer resolution, we had the opportunity to learn something new and interesting about how organic materials get damaged. This was a great opportunity to work in an interdisciplinary environment with chemists and chemical engineers and see how our knowledge could be utilized in areas which are nominally outside of our field. In this last chapter, our goal is to summarize our results, present some improvements that can be done to our set-up, and dream about our project's future directions.

8.1 Studying damage on organic materials

We were able to demonstrate that metastable atom electron spectroscopy is a reliable technique for studying damage induced on organic materials. Using metastable helium atoms had the advantage of minimally damaging the material of interest thus allowing us to identify any changes to our spectra due to the damaging agent. This is to be contrasted with x-ray photoelectron spectroscopy and techniques that probe materials with electron beams, where the probe beam induces damage on the sample which makes it difficult to identify any change to a spectrum solely on the damage agent of interest. Furthermore, using metastable atoms allowed us to study the surface of a material. This can be both good and bad. In many cases, the signal from the bulk makes it hard to identify what changes occurred at the surface. In other cases, where the damaging agent, such as x-rays or electrons, penetrates into the bulk causing changes and damage at various depths, having a technique that is sensitive only to what happens at the surface can prevent us from a plethora of important phenomena that happen in the bulk.

For our experiments, we mainly focused our attention in seeing the bond breaking between the bromine terminal group from the backbone of the alkanethiol molecule and that was a surface phenomenon. When we preformed the same experiment using XPS we had difficulty identifying and monitoring the peaks representing the bromine. This was due to the fact that there were significantly fewer bromine atoms in our sample since they were only present on the surface monolayer. In contrast, the gold peak in the case of the gold-

coated silicon substrate was extremely high and obscured the most dominant peak of bromine, forcing us to choose a significantly less pronounced peak. When we tried to verify our hypothesis that organic molecules adsorbed on graphene will be protected from damage we could not find any clear indication based on our preliminary data. In order to resolve this question, we need to perform the same experiment with improved signal to noise ratio as well as trace the sulfur and carbon peaks over time. We have successfully used a non-destructive electron spectroscopy technique and studied how electrons damage self-assembled monolayers.

8.2 Improvements

For starters, having a calibrated electron analyzer with technical support from the manufacturer will provide a big boost. Most of the time during the Ph.D. was spent trying to understand and calibrate our electron analyzer. That was a necessary task since we wanted to extract reliable information from our electron spectra. Having a new analyzer will also improve our sensitivity and resolution allowing us to see features that are otherwise hidden in the noise or broad peaks. A crucial companion to the electron analyzer is a vacuum chamber made out of μ -metal in order to eliminate the stray magnetic fields. Stray magnetic fields do influence the emitted electrons trajectories through the Lorentz force and make the study of magnetic materials cumbersome.

Furthermore, it is of huge importance to have instrumentation allowing us to study materials using different techniques in the same chamber. This

is extremely important because having multiple ways to study a phenomenon acts as a sanity check. In our opinion the best choice is to install an electron gun with the goal of performing Auger electron spectroscopy and scanning electron microscopy. The added benefit of adding an electron gun is the ability to continue the studies of damaging self-assembled monolayers, but in this case the electron source will be better characterized (spot size, current, and energy) and can be hopefully adjusted over a bigger energy range. Lastly, it will be also important to have a region before the metastable atoms interact with the sample where we can optically pump atoms in the desired energy level and magnetic state giving us atoms in a beam with a well characterized internal energy.

8.3 Future directions

8.3.1 Studying magnetism and other effects

As it was mentioned in section 8.2, having an optical pumping station will guarantee an atomic beam with almost all of its population occupying the energy level of our choice. Besides achieving beam purity, we can use optical pumping to select the magnetic state of our preference in order to study the magnetic properties of a surface in a similar manner as it was done in reference [92].

8.3.2 Making an atom microscope

As it was mentioned before, our initial goal was to construct an atom microscope with nanometer resolution, surface sensitivity, while inducing minimal amount of damage on the sample under investigation. The atom focusing can be achieved using a series of multipole electromagnetic lenses, such as the hexapole lens we have constructed [85], in conjunction with transverse laser cooling and apertures. Doing the above will enable us to have a bright enough beam for studies at the micrometer scale which will necessitate aberration correction such as incorporating a geometric taper on our lenses. In light of the manufacturing difficulties we have faced in making a tapered hexapole lens it is worthwhile exploring the possibility of operating the hexapole lens with a time dependent current pulse. The main issue with this idea is that we will not correct the aberrations if all the atoms are in the lens for the duration of the pulse. Instead, the current pulse should begin when the fastest atoms enter the lens so they will experience the magnetic force a longer amount of time in comparison with the slower atoms. However, even this approach faces the challenge of eliminating the fringe field effects.

Bibliography

[1] M. Zharnikov, W. Geyer, A. Gölzhäuser, S. Frey, and M. Grunze, "Modification of alkanethiolate monolayers on Au-substrate by low energy electron irradiation : Alkyl chains and the S/Au interface," *Phys. Chem. Chem. Phys.*, vol. 1, no. 13, pp. 3163–3171, 1999.

[2] M. Zharnikov, S. Frey, K. Heister, and M. Grunze, "Modification of Alkanethiolate Monolayers by Low Energy Electron Irradiation: Dependence on the Substrate Material and on the Length and Isotopic Composition of the Alkyl Chains," *Langmuir*, vol. 16, no. 6, pp. 2697–2705, Mar. 2000, ISSN: 0743-7463, 1520-5827. DOI: 10.1021/la991034r.

[3] M. Zharnikov and M. Grunze, "Modification of thiol-derived self-assembling monolayers by electron and x-ray irradiation: Scientific and lithographic aspects," *J. Vac. Sci. Technol. B Microelectron. Nanometer Struct.*, vol. 20, no. 5, pp. 1793–1807, 2002, ISSN: 0734211X. DOI: 10.1116/1.1514665.

[4] M. Zharnikov, "High-resolution X-ray photoelectron spectroscopy in studies of self-assembled organic monolayers," *J. Electron Spectrosc. Relat. Phenom.*, vol. 178-179, pp. 380–393, May 2010, ISSN: 03682048. DOI: 10.1016/j.elspec.2009.05.008.

[5] K. Seshadri, K. Froyd, A. N. Parikh, D. L. Allara, M. J. Lercel, and H. G. Craighead, "Electron-Beam-Induced Damage in Self-Assembled Monolayers," *J. Phys. Chem.*, vol. 100, no. 39, pp. 15 900–15 909, Jan. 1996, ISSN: 0022-3654, 1541-5740. DOI: 10.1021/jp960705g.

[6] C. Zhou, A. Trionfi, J. W. P. Hsu, and A. V. Walker, "Electron-Beam-Induced Damage of Alkanethiolate Self-Assembled Monolayers (SAMs): Dependence on Monolayer Structure and Substrate Conductivity," *J. Phys. Chem. C*, vol. 114, no. 20, pp. 9362–9369, May 27, 2010, ISSN: 1932-7447, 1932-7455. DOI: 10.1021/jp911402u.

[7] H. Morgner, "The characterization of liquid and solid surfaces with metastable helium atoms.pdf," in *Advances in Atomic, Molecular, and Optical Physics*, ser. Advances in Atomic, Molecular, and Optical Physics, vol. 42, Academic Press, 2000, pp. 387–483.

[8] E. E. Fill, F. Krausz, and M. G. Raizen, "Single-molecule electron diffraction imaging with charge replacement," *New J. Phys.*, vol. 10, no. 9, p. 093 015, Sep. 12, 2008, ISSN: 1367-2630. DOI: 10.1088/1367-2630/10/9/093015.

[9] S. Weinberg, *Lectures on Quantum Mechanics*, First edition. Cambridge University Press, 2013.

[10] *Interpretations of quantum mechanics*, in *Wikipedia*, Page Version ID: 942201265, Feb. 23, 2020. [Online]. Available: https://en.wikipedia.org/w/index.php?title=Interpretations_of_quantum_mechanics&oldid=942201265 (visited on 03/02/2020).

[11] C. Cohen-Tannoudji, B. Diu, and F. Laloë, *Quantum Mechanics*, First edition. Wiley-Interscience, 1977.

[12] *Hydrogen atom*, in *Wikipedia*, Page Version ID: 936493979, Jan. 19, 2020. [Online]. Available: https://en.wikipedia.org/w/index.php?title=Hydrogen_atom&oldid=936493979 (visited on 02/04/2020).

[13] A. Kramida, Yu. Ralchenko, J. Reader, and NIST ASD Team, "NIST ASD," 2019.

[14] G. K. Woodgate, *Elementary Atomic Structure*, Second edition. Oxford: Clarendon Press, 1980, ix+228, ISBN: 978-0-19-851146-5.

[15] R. C. Massé and T. G. Walker, "Accurate energies of the He atom with undergraduate quantum mechanics," *American Journal of Physics*, vol. 83, no. 8, pp. 730–732, Aug. 2015, ISSN: 0002-9505, 1943-2909. DOI: 10.1119/1.4921821.

[16] R. Loudon, "The quantum theory of light," in *The Quantum Theory of Light*, Third edition, Oxford: Oxford University Press, 2000, ISBN: 0-19-850177-3.

[17] V. B. Berestetskii, E. M. Lifshitz, and L. P. Pitaevskii, *Quantum Electrodynamics*, Second edition, ser. Course of Theoretical Physics. Pergamon Press, 1982, vol. 4.

[18] S. S. Hodgman, R. G. Dall, L. J. Byron, K. G. H. Baldwin, S. J. Buckman, and A. G. Truscott, "Metastable Helium: A New Determination of the Longest Atomic Excited-State Lifetime," *Phys. Rev. Lett.*, vol. 103, no. 5, Jul. 30, 2009, ISSN: 0031-9007, 1079-7114. DOI: 10.1103/PhysRevLett.103.053002.

[19] W. Happer, "Optical Pumping," *Rev. Mod. Phys.*, vol. 44, no. 2, pp. 169–249, Apr. 1, 1972, ISSN: 0034-6861. DOI: 10.1103/RevModPhys.44.169.

[20] J. J. McClelland, "Optical state-preparation of atoms," in *Atomic, Molecular, and Optical Physics: Atoms and Molecules*, ser. Experimental Methods in the Physical Sciences, vol. 29B, Academic Press, 1996, pp. 145–170.

[21] M. P. Marder, *Condensed Matter Physics*, Second edition. John Wiley & Sons, Inc., 2010.

[22] T. Shida, *The Chemical Bond: A Fundamental Quantum-Mechanical Picture*, ser. Springer Series in Chemical Physics 76. Springer-Verlag Berlin Heidelberg, 2004.

[23] M. W. Schmidt, J. Ivanic, and K. Ruedenberg, "The physical origin of covalent bonding," in *The Chemical Bond: Fundamental Apsects of Chemical Bonding*, vol. 1, 2 vols., Weinheim: Wiley-VCH, 2014, pp. 1–67, ISBN: 978-3-527-33314-1.

[24] G. Frenking and F. M. Bickelhaupt, "The EDA perspective of chemical bonding," in *The Chemical Bond: Fundamental Apsects of Chemical Bonding*, vol. 1, 2 vols., Weinheim: Wiley-VCH, 2014, pp. 121–157, ISBN: 978-3-527-33314-1.

[25] T. J. Gay, "Sources of metastable atoms and molecules," in *Atomic, Molecular, and Optical Physics: Atoms and Molecules*, ser. Experimental Methods in the Physical Sciences, vol. 29B, Academic Press, 1996, pp. 95–114.

[26] H. D. Hagstrum, "Theory of Auger Ejection of Electrons from Metals by Ions," *Phys. Rev.*, vol. 96, no. 2, pp. 336–365, Oct. 15, 1954, ISSN: 0031-899X. DOI: 10.1103/PhysRev.96.336.

[27] ——, "Ion-Neutralization Spectroscopy of Solids and Solid Surfaces," *Phys. Rev.*, vol. 150, no. 2, pp. 495–515, Oct. 14, 1966, ISSN: 0031-899X. DOI: 10.1103/PhysRev.150.495.

[28] ——, "Studies of adsorbate electronic structure using ion neutralization and photoemission spectroscopies," in *Electron and Ion Spectroscopy of Solids*, ser. NATO Advance Study Institutes Series, vol. 32, Plenum Press, 1978.

[29] ——, "Excited-Atom Deexcitation Spectroscopy using Incident Ions," *Phys. Rev. Lett.*, vol. 43, no. 14, pp. 1050–1053, Oct. 1, 1979, ISSN: 0031-9007. DOI: 10.1103/PhysRevLett.43.1050.

[30] Y. Harada, S. Masuda, and H. Ozaki, "Electron Spectroscopy Using Metastable Atoms as Probes for Solid Surfaces," *Chem. Rev.*, vol. 97,

no. 6, pp. 1897–1952, Oct. 1997, ISSN: 0009-2665, 1520-6890. DOI: 10.1021/cr940315v.

[31] T. Munakata, T. Hirooka, and K. Kuchitsu, "Electron emission from crystal surfaces of condensed aromatics under the impact of metastable rare gas atoms," *Journal of Electron Spectroscopy and Related Phenomena*, vol. 13, no. 3, pp. 219–228, Jan. 1978, ISSN: 03682048. DOI: 10.1016/0368-2048(78)85028-2.

[32] W. Allison, F. B. Dunning, and A. C. H. Smith, "Secondary electron ejection from metal surfaces by metastable atoms. III. Energy and angular distributions of the ejected electrons," *J. Phys. B: At. Mol. Phys.*, vol. 5, no. 6, pp. 1175–1185, Jun. 1972, ISSN: 0022-3700. DOI: 10.1088/0022-3700/5/6/020.

[33] S. Masuda, "Angle-resolved metastable atom electron spectra of Xe layers formed on graphite," *J. Electron Spectrosc. Relat. Phenom.*, vol. 76, pp. 359–364, Dec. 1995, ISSN: 03682048. DOI: 10.1016/0368-2048(95)02442-5.

[34] A. Bard, K. K. Berggren, J. L. Wilbur, J. D. Gillaspy, S. L. Rolston, J. J. McClelland, W. D. Phillips, M. Prentiss, and G. M. Whitesides, "Self-assembled monolayers exposed by metastable argon and metastable helium for neutral atom lithography and atomic beam imaging," *J. Vac. Sci. Technol. B Microelectron. Nanometer Struct.*, vol. 15, no. 5, p. 1805, Sep. 1997, ISSN: 0734211X. DOI: 10.1116/1.589529.

[35] S. Nowak, T. Pfau, and J. Mlynek, "Writing nanostructures with a metastable helium beam," *Microelectron. Eng.*, vol. 35, no. 1-4, pp. 427–430, Feb. 1997, ISSN: 01679317. DOI: 10.1016/S0167-9317(96)00124-4.

[36] B. D. Ratner and D. G. Castner, "Electron spectroscopy for chemical analysis," in *Surface Analysis - The Principal Techniques*, Second, John Wiley & Sons, Ltd, 2009, pp. 47–112.

[37] G. N. Lewis, "The atom and the molecule," *J. Am. Chem. Soc.*, vol. 38, no. 4, pp. 762–785, 1916.

[38] H. B. Gray, *Chemical Bonds : An Introduction to Atomic and Molecular Structure*. Sausalito, CA: University Science Books, 1994, ISBN: 0-8053-3402-5.

[39] R. T. Sanderson, *Chemical Bonds and Bond Energy*, Second, ser. Physical Chemistry: A Series of Monographs. Academic Press, Inc., 1976, vol. 21.

[40] S. J. Blanksby and G. B. Ellison, "Bond Dissociation Energies of Organic Molecules," *Acc. Chem. Res.*, vol. 36, no. 4, pp. 255–263, Apr. 2003, ISSN: 0001-4842, 1520-4898. DOI: 10.1021/ar020230d.

[41] Y.-R. Luo, *Handbook of Bond Dissociation Energies in Organic Compounds*. Boca Raton, Fla: CRC Press, 2003, 380 pp., ISBN: 978-0-8493-1589-3.

[42] A. Stone, *The Theory of Intermolecular Forces*, Second edition. Oxford University Press, 2013.

[43] J. N. Israelachvili, *Intermolecular and Surface Forces*, Third edition. Burlington: Elsevier Science, 2011, ISBN: 1-283-13731-3.

[44] J. C. Love, L. A. Estroff, J. K. Kriebel, R. G. Nuzzo, and G. M. Whitesides, "Self-Assembled Monolayers of Thiolates on Metals as a Form of Nanotechnology," *Chem. Rev.*, vol. 105, no. 4, pp. 1103–1170, Apr. 2005, ISSN: 0009-2665, 1520-6890. DOI: 10.1021/cr0300789.

[45] A. Ulman, *An Introduction to Ultrathin Organic Films: From Langmuir-Blodgett to Self-Assembly*. Academic Press, 1991.

[46] E. Pensa, E. Cortés, G. Corthey, P. Carro, C. Vericat, M. H. Fonticelli, G. Benítez, A. A. Rubert, and R. C. Salvarezza, "The Chemistry of the Sulfur–Gold Interface: In Search of a Unified Model," *Acc. Chem. Res.*, vol. 45, no. 8, pp. 1183–1192, Aug. 21, 2012, ISSN: 0001-4842, 1520-4898. DOI: 10.1021/ar200260p.

[47] G. E. Poirier, "Characterization of Organosulfur Molecular Monolayers on Au(111) using Scanning Tunneling Microscopy," *Chem. Rev.*, vol. 97, no. 4, pp. 1117–1128, Jun. 1997, ISSN: 0009-2665, 1520-6890. DOI: 10.1021/cr960074m.

[48] D. K. Schwartz, "Mechanisms and kinetics of self -assembled monolayer formation," *Annu. Rev. Phys. Chem.*, vol. 52, no. 1, pp. 107–137, Oct. 2001, ISSN: 0066-426X, 1545-1593. DOI: 10.1146/annurev.physchem.52.1.107.

[49] T. Kondo, R. Yamada, and K. Uosaki, "Self-assembled monolayers (SAM)," in *Organized Organic Ultrathin Films*, Wiley-VCH, 2013, pp. 7–42.

[50] Q. H. Wang and M. C. Hersam, "Room-temperature molecular-resolution characterization of self-assembled organic monolayers on epitaxial graphene," *Nat. Chem.*, vol. 1, no. 3, pp. 206–211, Jun. 2009, ISSN: 1755-4330, 1755-4349. DOI: 10.1038/nchem.212.

[51] B. Lee, Y. Chen, F. Duerr, D. Mastrogiovanni, E. Garfunkel, E. Y. Andrei, and V. Podzorov, "Modification of Electronic Properties of Graphene

with Self-Assembled Monolayers," *Nano Lett.*, vol. 10, no. 7, pp. 2427–2432, Jul. 14, 2010, ISSN: 1530-6984, 1530-6992. DOI: 10.1021/nl100587e.

[52] T. Zhang, Z. Cheng, Y. Wang, Z. Li, C. Wang, Y. Li, and Y. Fang, "Self-Assembled 1-Octadecanethiol Monolayers on Graphene for Mercury Detection," *Nano Lett.*, vol. 10, no. 11, pp. 4738–4741, Nov. 10, 2010, ISSN: 1530-6984, 1530-6992. DOI: 10.1021/nl1032556.

[53] M. D. Porter, T. B. Bright, D. L. Allara, and C. E. D. Chidsey, "Spontaneously organized molecular assemblies. 4. Structural characterization of n-alkyl thiol monolayers on gold by optical ellipsometry, infrared spectroscopy, and electrochemistry," *J. Am. Chem. Soc.*, vol. 109, no. 12, pp. 3559–3568, Jun. 1987, ISSN: 0002-7863. DOI: 10.1021/ja00246a011.

[54] Z. G. Hu, P. Prunici, P. Patzner, and P. Hess, "Infrared Spectroscopic Ellipsometry of n -Alkylthiol (C_5 -C_{18}) Self-Assembled Monolayers on Gold," *J. Phys. Chem. B*, vol. 110, no. 30, pp. 14 824–14 831, Aug. 2006, ISSN: 1520-6106, 1520-5207. DOI: 10.1021/jp060596y.

[55] B. Heinz and H. Morgner, *MIES investigation of alkanethiol monolayers self-assembled on Au(111) and Ag(111) surfaces*, Feb. 27, 1996.

[56] E. Ito, M. Yamamoto, K. Kajikawa, D. Yamashita, H. Ishii, Y. Ouchi, K. Seki, H. Okawa, and K. Hashimoto, "Orientational Structure of Thiophene Thiol Self-Assembled Monolayer Studied by Using Metastable Atom Electron Spectroscopy and Infrared Reflection Absorption Spectroscopy," *Langmuir*, vol. 17, no. 14, pp. 4282–4286, Jul. 2001, ISSN: 0743-7463, 1520-5827. DOI: 10.1021/la001671d.

[57] A. Ulman, "Formation and Structure of Self-Assembled Monolayers," *Chem. Rev.*, vol. 96, no. 4, pp. 1533–1554, Jan. 1996, ISSN: 0009-2665, 1520-6890. DOI: 10.1021/cr9502357.

[58] S. Casalini, C. A. Bortolotti, F. Leonardi, and F. Biscarini, "Self-assembled monolayers in organic electronics," *Chem. Soc. Rev.*, vol. 46, no. 1, pp. 40–71, 2017, ISSN: 0306-0012, 1460-4744. DOI: 10.1039/C6CS00509H.

[59] T. Noyhouzer and D. Mandler, "Determination of low levels of cadmium ions by the under potential deposition on a self-assembled monolayer on gold electrode," *Analytica Chimica Acta*, vol. 684, no. 1-2, pp. 1–7, Jan. 2011, ISSN: 00032670. DOI: 10.1016/j.aca.2010.10.021.

[60] N. K. Chaki and K. Vijayamohanan, "Self-assembled monolayers as a tunable platform for biosensor applications," *Biosens. Bioelectron.*, vol. 17, no. 1-2, pp. 1–12, Jan. 2002, ISSN: 09565663. DOI: 10.1016/S0956-5663(01)00277-9.

[61] G. Gillen, S. Wight, J. Bennett, and M. J. Tarlov, "Patterning of self-assembled alkanethiol monolayers on silver by microfocus ion and electron beam bombardment," *Appl. Phys. Lett.*, vol. 65, no. 5, pp. 534–536, Aug. 1994, ISSN: 0003-6951, 1077-3118. DOI: 10.1063/1.112289.

[62] J. A. M. Sondag-Huethorst, H. R. J. van Helleputte, and L. G. J. Fokkink, "Generation of electrochemically deposited metal patterns by means of electron beam (nano)lithography of self-assembled monolayer resists," *Appl. Phys. Lett.*, vol. 64, no. 3, pp. 285–287, Jan. 17, 1994, ISSN: 0003-6951, 1077-3118. DOI: 10.1063/1.111182.

[63] K. K. Berggren, A. Bard, J. L. Wilbur, J. D. Gillaspy, A. G. Helg, J. J. McClelland, S. L. Rolston, W. D. Phillips, M. Prentiss, and G. M. Whitesides, "Microlithography by Using Neutral Metastable Atoms and Self-Assembled Monolayers," *Science*, vol. 269, no. 5228, pp. 1255–1257, 1995, ISSN: 0036-8075. [Online]. Available: https://www.jstor.org/stable/2888009 (visited on 03/08/2019).

[64] W. Geyer, V. Stadler, W. Eck, M. Zharnikov, A. Gölzhäuser, and M. Grunze, "Electron-induced crosslinking of aromatic self-assembled monolayers: Negative resists for nanolithography," *Appl. Phys. Lett.*, vol. 75, no. 16, pp. 2401–2403, Oct. 18, 1999, ISSN: 0003-6951, 1077-3118. DOI: 10.1063/1.125027.

[65] L. P. Ratliff, R. Minniti, A. Bard, E. W. Bell, J. D. Gillaspy, D. Parks, A. J. Black, and G. M. Whitesides, "Exposure of self-assembled monolayers to highly charged ions and metastable atoms," *Appl. Phys. Lett.*, vol. 75, no. 4, pp. 590–592, Jul. 26, 1999, ISSN: 0003-6951, 1077-3118. DOI: 10.1063/1.124451.

[66] M. L. Chabinyc, J. C. Love, J. H. Thywissen, F. Cervelli, M. G. Prentiss, and G. M. Whitesides, "Self-Assembled Monolayers Exposed to Metastable Argon Beams Undergo Thiol Exchange Reactions," *Langmuir*, vol. 19, no. 6, pp. 2201–2205, Mar. 2003, ISSN: 0743-7463, 1520-5827. DOI: 10.1021/la026495i.

[67] R. Klauser, I.-H. Hong, S.-C. Wang, M. Zharnikov, A. Paul, A. Gölzhäuser, A. Terfort, and T. J. Chuang, "Imaging and Patterning of Monomolecular Resists by Zone-Plate-Focused X-ray Microprobe," *J. Phys. Chem. B*, vol. 107, no. 47, pp. 13 133–13 142, Nov. 2003, ISSN: 1520-6106, 1520-5207. DOI: 10.1021/jp0307396.

[68] F. Saimura and M. Santorelli, "Photoresists," in *Phenolic Resins: A Century of Progress*, L. Pilato, Ed., Berlin, Heidelberg: Springer Berlin

Heidelberg, 2010, pp. 363–382, ISBN: 978-3-642-04713-8 978-3-642-04714-5. DOI: 10.1007/978-3-642-04714-5_15.

[69] H. J. Levinson, "Photoresists," in *Principles of Lithography*, Third edition, SPIE Press, 2011, pp. 51–108.

[70] J. H. I. Thomas, "Photon beam damage and charging at solid surfaces," in *Beam Effects, Surface Topography, and Depth Profiling in Surface Analysis*, ser. Methods of Surface Characterization, vol. 5, Plenum Press, 1998, pp. 1–37.

[71] D. C. Joy and S. Luo, "An empirical stopping power relationship for low-energy electrons," *Scanning*, vol. 11, no. 4, pp. 176–180, 1989, _eprint: https://onlinelibrary.wiley.com/doi/pdf/10.1002/sca.4950110404, ISSN: 1932-8745. DOI: 10.1002/sca.4950110404.

[72] H. T. Nguyen-Truong, "Modified Bethe formula for low-energy electron stopping power without fitting parameters," *Ultramicroscopy*, vol. 149, pp. 26–33, Feb. 2015, ISSN: 03043991. DOI: 10.1016/j.ultramic.2014.11.003.

[73] C. G. Pantano, A. S. D' Souza, and A. M. Then, "Electron beam damage at solid surfaces," in *Beam Effects, Surface Topography, and Depth Profiling in Surface Analysis*, ser. Methods of Surface Characterization, vol. 5, Plenum Press, 1998, pp. 39–96.

[74] K. Heister, M. Zharnikov, M. Grunze, L. S. O. Johansson, and A. Ulman, "Characterization of X-ray Induced Damage in Alkanethiolate Monolayers by High-Resolution Photoelectron Spectroscopy," *Langmuir*, vol. 17, no. 1, pp. 8–11, Jan. 2001, ISSN: 0743-7463, 1520-5827. DOI: 10.1021/la001101d.

[75] P. Engels, S. Salewski, H. Levsen, K. Sengstock, and W. Ertmer, "Atom lithography with a cold, metastable neon beam," *Appl. Phys. B*, vol. 69, no. 5-6, pp. 407–412, Dec. 1999, ISSN: 0946-2171, 1432-0649. DOI: 10.1007/s003400050827.

[76] K. Sader, M. Stopps, L. J. Calder, and P. B. Rosenthal, "Cryomicroscopy of radiation sensitive specimens on unmodified graphene sheets: Reduction of electron-optical effects of charging," *Journal of Structural Biology*, vol. 183, no. 3, pp. 531–536, Sep. 2013, ISSN: 10478477. DOI: 10.1016/j.jsb.2013.04.014.

[77] E. Hecht, *Optics*, Fourth edition. Reading, Mass: Addison-Wesley, 2002, ISBN: 0-8053-8566-5.

[78] P. W. Hawkes and E. Kasper, *Principles of Electron Optics: Basic Geometrical Optics.* Second edition, 2 vols. London, England: Academic Press, 2017, vol. 1, ISBN: 978-0-08-102257-3.

[79] P. Hawkes and E. Kasper, *Principles of Electron Optics: Applied Geometrical Optics*, Second edition, 2 vols. London, England: Academic Press, 2017, vol. 2, ISBN: 0-12-813405-4.

[80] J. Erskine, "Electron energy analyzers," in *Experimental Methods in the Physical Sciences*, vol. 29A, Academic Press, 1995.

[81] H. J. Metcalf and P. van der Straten, *Laser Cooling and Trapping*, First edition, ser. Graduate Texts in Contemporary Physics. New York: Springer Science+Business Media New York, 1999.

[82] W. G. Kaenders, F. Lison, A. Richter, R. Wynands, and D. Meschede, "Imaging with an atomic beam," *Nature*, vol. 375, no. 6528, pp. 214–216, May 1995, ISSN: 0028-0836, 1476-4687. DOI: 10.1038/375214a0.

[83] J. R. Gardner, *Neutral Atom Imaging Using a Pulsed Electromagnetic Lens*, ser. Springer Theses. Cham: Springer International Publishing, 2018, ISBN: 978-3-319-68429-1 978-3-319-68430-7. DOI: 10.1007/978-3-319-68430-7.

[84] R. Castillo-Garza, J. Gardner, S. Zisman, and M. G. Raizen, "Nanoscale Imaging of Neutral Atoms with a Pulsed Magnetic Lens," *ACS Nano*, vol. 7, no. 5, pp. 4378–4383, May 28, 2013, ISSN: 1936-0851, 1936-086X. DOI: 10.1021/nn400896y.

[85] J. R. Gardner, E. M. Anciaux, and M. G. Raizen, "Communication: Neutral atom imaging using a pulsed electromagnetic lens," *J. Chem. Phys.*, vol. 146, no. 8, p. 081 102, Feb. 28, 2017, ISSN: 0021-9606, 1089-7690. DOI: 10.1063/1.4976986.

[86] E. Anciaux, G. Stratis, and M. G. Raizen, "Brightening of a supersonic beam of neutral atoms," *Phys. Scr.*, vol. 93, no. 12, p. 124 009, Dec. 1, 2018, ISSN: 0031-8949, 1402-4896. DOI: 10.1088/1402-4896/aae716.

[87] U. Even, "Pulsed Supersonic Beams from High Pressure Source: Simulation Results and Experimental Measurements," *Adv. Chem.*, vol. 2014, pp. 1–11, Aug. 3, 2014, ISSN: 2356-6612, 2314-7571. DOI: 10.1155/2014/636042.

[88] L. Vattuone, G. Bracco, M. Smerieri, Savio, Letizia, and Rocca, Mario, "Supersonic molecular beams studies of surfaces," in *Dynamics of Gas-Surface Interactions: Atomistic-Level Understanding of Scattering Processes at Surfaces*, Springer, 2013.

[89] M. D. Morse, "Supersonic beam sources," in *Atomic, Molecular, and Optical Physics: Atoms and Molecules*, ser. Experimental Methods in the Physical Sciences, vol. 29B, Academic Press, 1996, pp. 21–47.

[90] P. X. Feng and B. Weiner, "A collimated pulsed supersonic metastable helium atomic beam," *Phys. Scr.*, vol. 75, no. 4, pp. 565–571, Apr. 2007, ISSN: 0031-8949, 1402-4896. DOI: 10.1088/0031-8949/75/4/033.

[91] T. Halfmann, J. Koensgen, and K. Bergmann, "A source for a high-intensity pulsed beam of metastable helium atoms," *Meas. Sci. Technol.*, vol. 11, no. 10, pp. 1510–1514, Oct. 1, 2000, ISSN: 0957-0233, 1361-6501. DOI: 10.1088/0957-0233/11/10/312.

[92] F. Dunning and P. Nordlander, "Spin-dependent studies of the dynamics of He(23S) atom deexcitation at surfaces," *Nucl. Instrum. Methods Phys. Res. Sect. B Beam Interact. Mater. At.*, vol. 100, no. 2-3, pp. 245–252, Jun. 1995, ISSN: 0168583X. DOI: 10.1016/0168-583X(94)00839-6.